Design and Characterization of Crystalline Thin Film Architectures at the Air–Liquid Interface: Simplicity to Complexity

Ivan Kuzmenko, Hanna Rapaport, Kristian Kjaer, Jens Als-Nielsen, Isabelle Weissbuch, Meir Lahav,* and Leslie Leiserowitz*

Department of Materials and Interfaces, The Weizmann Institute of Science, 76100 Rehovot, Israel, Materials Research Department, Risø National Laboratory, DK 4000, Roskilde, Denmark, and Niels Bohr Institute, H. C. Ørsted Laboratory, DK 2100, Copenhagen, Denmark

Received July 12, 2000

Contents

I. Introduction

Ordered molecular clusters with a length scale down to few nanometers are currently attracting

* To whom correspondence should be addressed. Email: meir.lahar@weizmann.ac.il, leslie.leiserowitz@weizmann.ac.il.

10.1021/cr990038y CCC: $36.00
Published on Web 05/12/2001

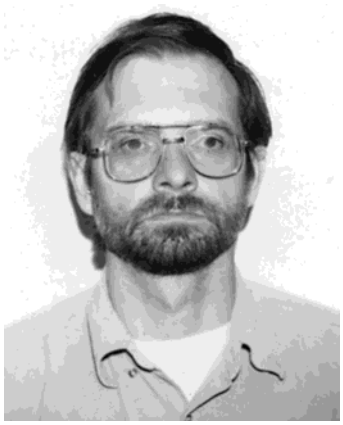



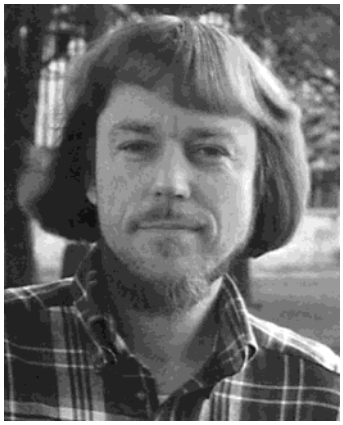
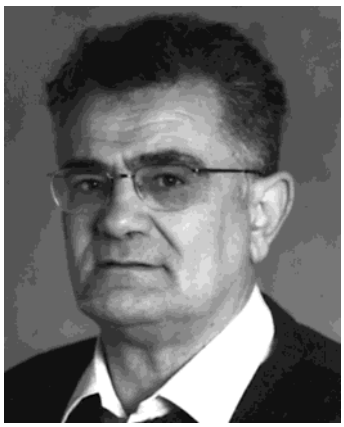

wide attention in the physical and biological sciences. The design and preparation of functional materials such as thin-layered microstructures, reagent films for biosensors, and devices for optoelectronics requires knowledge and control of nanoarchitectures from the very early stages of self-organization. This requirement is linked to the control of nucleation, growth, morphology, and dissolution of crystals.

For many years crystal nucleation has been studied primarily by kinetic and thermodynamic methods[1] that supplied experimental proof for the existence of clusters in supersaturated solutions but little information on their structure and their possible role as intermediates in the crystallization process. The recent development of various methods for the elucidation of molecular ordering at interfaces has provided a means to probe the early stages of molecular assembly. One approach involves the use of crystalline monolayers of amphiphilic molecules on aqueous solution to induce nucleation of solute molecules into three-dimensional (3-D) crystals at the air−solution interface. The monolayer, through its hydrophilic headgroups, is a template for the molecular solute arrangement within a particular plane of the 3-D crystal.

Another avenue for probing the early stages of molecular assembly involves the spontaneous formation, at the air−water interface, of crystalline films ranging from one to several layers thick, composed of water-insoluble molecules, such as amphiphiles, bolaform amphiphiles, and chainlike hydrocarbons. This tendency also provides a means for engineering various packing arrangements, for example, multicomponent thin film crystallites of supramolecular architecture prepared in situ via water-insoluble and solute molecules interacting at the solution surface.

This review shall be presented in terms of three different types of ordered films at the air−solution

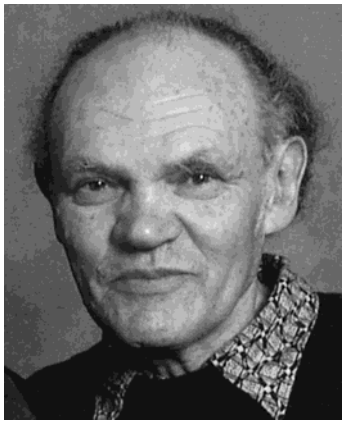

The review represents the fruits of a collaboration between scientists schooled in different disciplines: crystallography, chemistry and physics and whose home bases are far apart. The common playground where they regularly met is the liquid surface X-ray diffractometer at the synchrotron light source Hasylab, Hamburg. In the mid eighties Jens Als-Nielsen and Kristian Kjaer had played a pioneering role in the use of synchrotron X-radiation for the study of crystalline films composed of amphiphilic molecules at the water surface. At the same time Meir Lahav and Leslie Leiserowitz had concluded on the basis of simple crystallization experiments that certain amino acids amphiphiles self assemble into monolayer crystallites on the water surface. Thus a collaborative effort was initiated in 1986 between the groups from Risø and the Weizmann Institute to examine by grazing incidence X-ray diffraction (GIXD) at a bending magnet beamline the monolayer crystalline structures of simple long-chain amino acids. This cooperative effort resulted in a continual, tandem interplay between thin film design and X-ray structural elucidation in topics ranging from induced ice nucleation, photochemical reactions at interfaces, separation of enantiomers, multicomponent molecular self assembly and cholesterol nucleation. A boost to the research came in the early 1990's with the use of intense X-rays from an undulator device. By these means Isabelle Weissbuch moved up the ladder of structural elucidation from simple amphiphiles to complex supramolecular architectures. Hanna Rapaport and Ivan Kuzmenko, presently post doctoral fellows at Dept of Chemical Engineering, Caltech and Lawrence BerKeley Laboratory, respectively, did their PH. D. studies on complex multilayer structures, contending with the problems of design and elucidation of the packing arrangements to near atomic resolution.

Scheme 1

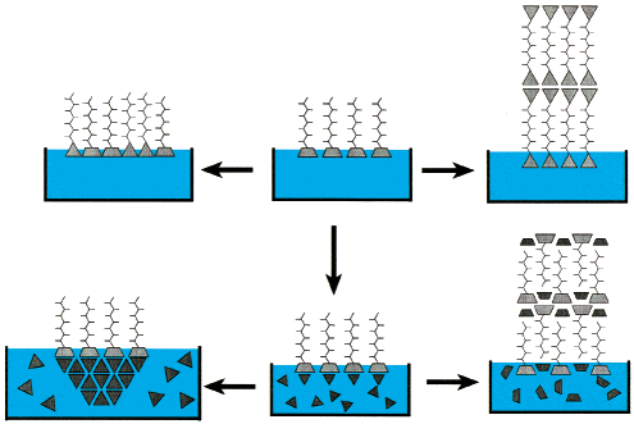

interface (Scheme 1): first, monolayer arrangements of amphiphilic molecules at the air−liquid interface and interaction between the monolayer and the solution subphase (Scheme 1, central and left columns). We next describe crystallite multilayers composed of water-insoluble molecules only, and finally, multilayers generated by reaction between the water-insoluble species with solutes from the subphase to form complex architectures will be discussed (Scheme 1, right column).

The enormous strides made over the past decade for the elucidation of molecular ordering at interfaces has been made possible by the development of a variety of experimental tools. These include surface-specific X-ray diffraction, X-ray and neutron reflectivity, scanning-tunneling and scanning-force microscopy, cryo-electron microscopy, nonlinear optics, and surface reflectance infrared spectroscopy. In this review much use is made of grazing incidence X-ray diffraction (GIXD) using synchrotron radiation. It is with the advent of intense and highly collimated X-ray beams of variable wavelength from synchrotron sources that GIXD has become such a valuable tool to obtain direct structural information of crystalline films at interfaces at the subnanometer scale. The principles of GIXD and X-ray reflectivity for the characterization of two-dimensional (2-D) crystalline films of amphiphilic molecules at the air−liquid interface have been detailed in recent reviews.[2−9] A description thereof is given in the Appendix, to facilitate understanding of the results presented here.

II. Scope of the Review

The description of amphiphilic monolayers shall encompass an outline of phase behavior upon compression of the film on the liquid surface from the 'gaseous' to the 'solid' state. We shall examine crystalline self-assembly of long-chain achiral and chiral amphiphiles and their various monolayer packing arrangements, control of crystalline domain size, topochemical behavior of photoreactive amphiphiles, and the impact of crystalline order in monolayer films on catalysis. Next, we discuss interactions between the polar headgroups of the amphiphiles and the solution subphase, followed by induced nucleation of three-dimensional crystals at the monolayer−solution interface. The generation of multilayer crystals at the surface of a pure liquid shall be discussed in terms of the nature of the subphase and the various types of water-insoluble molecules such as amphiphiles, bolaform amphiphiles, and pure hydrocarbons. We describe the formation of multilayer crystallites obtained by compression of the monolayer film beyond the collapse point leading to interdigitated bilayers, or spontaneously generated by reaction of the water-insoluble species with solutes from the subphase to form complex architectures such as interdigitated molecular bilayers, metal salts of dicarboxylic acids, supramolecular grids, and complexed ionophores and superlattices composed of organically functionalized nanocrystal monolayers.

We attempted to make a comprehensive presentation of chemical design and structural characterization of thin film crystalline systems on liquid surfaces, although the major proportion of crystalline systems presented here in more detail are from our group. Reviews encompassing other viewpoints and aspects of Langmuir monolayers of long-chain amphiphiles, in particular their physical properties, such as phase transitions and morphological patterns, have been published over the past decade.[10−13] Some aspects of these reviews shall be considered below.

III. Structural Characteristics of Langmuir Monolayers

A. Langmuir Monolayer Phases

Monomolecular films are formed when water-insoluble amphiphilic molecules are spread at the air−water interface. These 2-D systems can exist in different phases depending on the lateral pressure and temperature of the film. At low surface densities, monolayers exist in a gaseous state *G*, which upon compression undergo a phase transition first to a "liquid expanded" *LE* and then to a 'liquid condensed' *LC* phase. At high surface pressure, a "solid" *S* condensed phase is obtained.

Identification of different phases is possible by various means. Liquid, gas, and their coexisting regions can be characterized by visual observations using fluorescence microscopy. For example, the transition of phases *G* to *LE* and *LE* to *LC* was detected by fluorescence microscopy for pentadecanoic acid.[14] Langmuir monolayers of amphiphilic compounds such as fatty acids, alcohols, and their esters are rich in liquid crystalline phases.[15]

Grazing incidence X-ray diffraction provided the first clear-cut evidence for monolayer crystalline structure of amphiphiles.[16−18] Several groups of compounds including long-chain alcohols, carboxylic acids and amides, α-amino acids, phospholipids, and their derivatives were the main systems characterized by GIXD.[8,13] This method also demonstrated that many amphiphilic types spontaneously form in the uncompressed region of the isotherm, monolayer, or multilayer crystals, up to tens of nanometer in lateral coherence length as shall be described below.

B. Monolayer Packing Motifs of Hydrocarbon Chain Amphiphiles

A precise determination of 2-D crystal structure of the amphiphilic film on the liquid surface can be achieved by an analysis of its GIXD data, sometimes to even near atomic resolution, particularly when coupled with a knowledge of 3-D crystal structures of the same or analogous molecules, atom−atom potential energy calculations, and spectroscopic methods such as sum frequency generation. The large number of GIXD monolayer studies of the simple amphiphiles, $C_nH_{2n+1}X$, where X is a headgroup such as COOH or OH, have yielded a variety of phases ranging from mesophases that possess partial orientational and translational order to highly crystalline structures, recently reviewed in detail in ref 13.

All these monolayer structures have one basic feature in common: their hydrocarbon chain axes are parallel to one another. The packing of hydrocarbon chains can be further classified according to the subcell a_p, b_p, c, in which a_p and b_p describe a two-dimensional lattice perpendicular to the chain axis and $c = 2.4$ Å corresponds to the periodicity along the chain.[19] A distribution of the cell dimensions a_p and b_p (Figure 1a) of monolayers for various phases lie, with some scatter, on a continuous arc. The central region, distinguished by a hexagonal-type lattice, is occupied by low-density mesophases; the

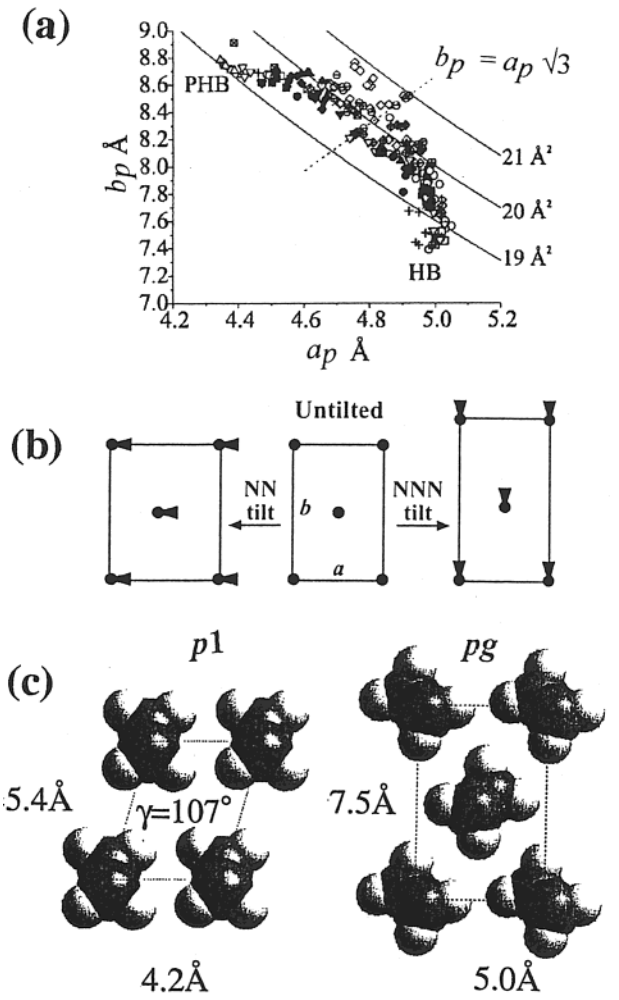

Figure 1. (a) Distribution of projected unit cell axes (a_p, b_p) extracted from GIXD data of various Langmuir monolayers. Parallel solid lines correspond to values of constant cross-sectional area $= a_p b_p/2$ occupied by a single hydrocarbon chain. The dashed line corresponds to the hexagonal projected unit cell with $b_p = a_p\sqrt{3}$. Labels HB and PHB denote the commonly observed herringbone and rarely encountered pseudo herringbone motifs, respectively. (b) Herringbone motif HB shown on the right and translation packing of chains on the left. (c) Direction of tilt toward nearest neighbors (NN) and next-nearest neighbor (NNN) of hydrocarbon chains that pack in the HB motif.

two ends of the arc correspond to relatively dense chain packing with rectangular unit cell dimensions 5.0×7.5 Å^2 and 4.4×8.7 Å^2. The two molecular chains in each unit cell in both motifs are related by glide (*g*) symmetry in the plane group *pg*, the former motif (Figure 1c, right) being the most commonly observed. It embodies a herringbone arrangement of the chains and is found in the monolayer crystals of the fatty acids, e.g., $C_{29}H_{39}CO_2H$,[20] and the alcohols[21] $C_nH_{2n+1}OH$, $n = 16-31$. In view of the glide symmetry, the hydrocarbon chains may tilt along either the short *a*-axis or the long *b*-axis, corresponding to tilting toward nearest neighbors (NN) or toward next-nearest neighbors (NNN), respectively, as shown schematically in Figure 1b. Molecules have also been observed to pack in another characteristic symmetry pattern, plane groups *p*1. The unit cell is oblique, and the only symmetry element is translation as depicted in Figure 1c, left. The molecules that crystallize in

*p*1 symmetry on water include α-amino acids[22] and arachidamide.[23]

In general, the monolayer packing arrangements of amphiphilic molecules on the aqueous surface are similar to their 3-D crystalline counterpart, the differences lie mostly in chain tilt. This latter observation suggests that in 3-D crystals and in amphiphilic monolayers, interlayer forces and interactions between hydrophilic headgroups and the aqueous subphase, respectively, play a role in determining intralayer packing.

C. Molecular Interactions and Crystallinity

The amount of crystalline material in self-aggregated clusters of amphiphilic molecules has been found to depend on several factors, including temperature, conformational flexibility, hydrophobic chain length and type, the nature of the hydrophilic headgroup, and the nature of the solvent subphase with which the headgroups are in contact. The role played by chain flexibility has been inferred by the higher crystallinity of Langmuir monolayers of molecules containing fluorocarbon chains C_nF_{2n+1} compared with the hydrocarbon counterpart C_nH_{2n+1},[24] in view of the inherent "stiffness" of the fluorocarbon chain.[25,26] However, intermolecular forces also play a role, since potential energy calculations have indicated a more favorable interaction between the fluorocarbon chains than between hydrocarbon chains.[24] In general, for amphiphilic molecules which form 2-D crystalline self-aggregates when deposited on the liquid surface, the amount of monolayer crystalline material formed and the extent of crystal coherence are both enhanced the longer the chain. This observation may be simply correlated with the contribution to the lattice energy by each additional CH_2 group in the chain. By a similar criterion, the stronger the interaction between the headgroups, other things being held equal, the more crystalline the material.

The effect ions may have on the extent of monolayer crystallization was observed by comparing the films of arachidic acid over pure water and cadmium arachidate formed over a $CdCl_2$ solution, the amount of crystalline material formed being higher for the latter.[27,28] Clearly the Cd ion···carboxylate interactions are stronger than those between the neutral carboxyl groups. Another example of enhanced crystalline self-aggregation induced by ions involves the short chain myristic acid $C_{13}H_{27}CO_2H$. It did not yield any GIXD signal over a pure water subphase but showed a long-range crystallinity in the form of cadmium myristate.[29]

The lateral extent of perfect crystalline order in different directions, termed also the positional coherence lengths L, was found to be distinctly anisotropic in monolayer crystals for amphiphilic molecules with a large chain tilt. The coherence length extends much further in the direction perpendicular to the molecular tilt direction than parallel to it. Lattice energy calculations, involving the attachment energy of a row of the amphiphilic molecules to different monolayer (h,k) facets, yielded weaker attachment along the tilt direction, compatible with a shorter coherence length.[30] This approach, linking the 2-D crystal coherence length with the relative attachment energy of the amphiphile to different monolayer facets, is akin to that adopted in order to calculate the growth morphology of 3-D crystals; the rate of growth for a particular layer in a certain (h,k,l) direction is proportional to the attachment energy of that layer to the crystal face.[31]

D. Buckling of Langmuir Films

Under compression, rigid molecular films may buckle in the third dimension, leading to a corrugated structure. Such corrugation has been detected by X-ray scattering in monolayer films of fatty acids on divalent cation subphases at high pH and low temperature as reported by Daillant and co-workers.[32,33] An X-ray scattering pattern for arachidic acid is depicted in Figure 2a. The buckling wavelength $\Lambda \approx 20nm$ (Figure 2a, inset) changes only slightly under compression, but the amplitude strongly increases. This buckling could be induced by the asymmetry in packing constraints for headgroups and aliphatic chains.[33]

Complementary, yet independent, information on monolayer buckling can be inferred from the skewed shapes of Bragg rods observed in the GIXD patterns of films on water such as some long chain α-amino acids (see section IV.A) and the alkanes $C_n\ H_{2n+2}$, $n = 34, 50$ (see section VII.D) shown in Figure 2b for $n = 50$. These Bragg rods were interpreted in terms of bent crystalline films assuming a concave-like shape, which is in accordance with, but not proof of, a regular surface corrugation.

E. Topochemical Reactions in Langmuir Films

A correlation between the stereochemistry of products formed in solid-state reactions and the packing arrangements of the reactant molecules in the 3-D crystals has been demonstrated for a large variety of systems, and such reactions are referred to as topochemically controlled. This type of control has also been invoked in photoreactions in assemblies possessing a lower degree of order such as micelles, vesicles, microemulsions, Langmuir monolayers, and Langmuir−Blodgett multilayers.[34−38]

According to the rules of topochemically controlled reactions in the solid state,[39] neighboring *trans*-cinnamic acid molecules, $C_6H_4-CH=CH-CO_2H$, separated by translation of about 4 Å will, upon UV irradiation, photoreact across their C=C double bonds to form a mirror dimer (Scheme 2a). Thus, we anticipated that crystalline *trans*-cinnamic acid molecular monolayers on water of the type $R-C_6H_4-CH=CH-CO_2H$, where R contains a long hydrocarbon chain in the *para* position, would photodimerize provided the neighboring C=C bonds are separated by about 4 Å. A monolayer of the analogous *trans*-cinnamamide $R-C_6H_4-CH=CH-CONH_2$ should not dimerize on the following basis: An ordered array of cinnamamide molecules should be interlinked by N−H···O=C hydrogen bonds along a repeat axis of 5 Å, generating ribbons (Scheme 2b). These ribbons cannot be stacked along a translation axis shorter than 5 Å because the cross-sectional area of cin-

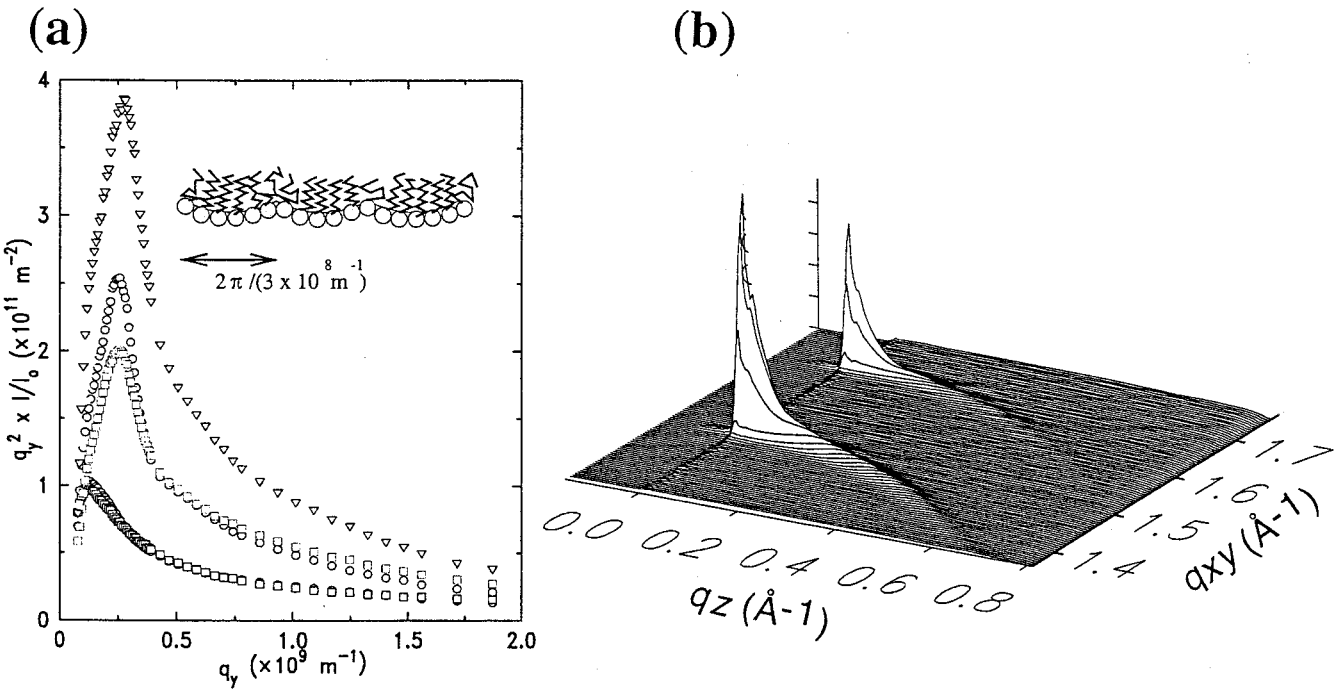

Figure 2. (a) X-ray intensity $I(q_y)$, where $q_y = q_{xy}$, scattered in the plane of incidence by an arachidic acid film deposited on a $CdCl_2$ solution at high pH and $T = 5$ °C, as a function of increasing pressure π from (bottom) 1.4 to (top) 20 mN/m. Inset: Buckled monolayer with wavelength $\Lambda \approx 20$ nm (Reprinted with permission from J. Daillant ref 33). (b) GIXD pattern $I(q_{xy},q_z)$ of an uncompressed monolayer $C_{50}H_{102}$ on water showing skewed Bragg rods.

Scheme 2

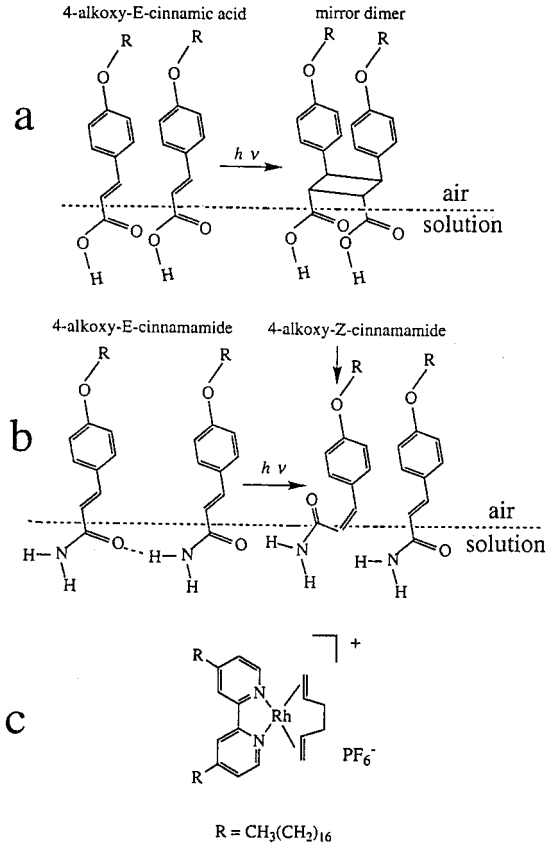

namamide is about 25 Å^2. Such molecules should undergo a *trans*−*cis* photoisomerization (Scheme 2b).

These predictions were tested with monolayers on water of the amphiphiles[40] $C_{18}H_{37}OC_6H_4CH{=}CHY$, $Y = CO_2H$, $CONH_2$. UV irradiation of the trans acid monolayer yields the mirror dimer, whereas the amide system undergoes *trans*−*cis* isomerization. Both monolayers form self-aggregated 2-D crystalline clusters according to their GIXD patterns. The GIXD pattern of the acid shows coexistence of two crystalline phases. The crystal structure of the major phase (Figure 3a) embodies a 4 Å separation between essentially parallel C=C double bonds of neighboring glide-related cinnamic acid moieties, in keeping with formation of the mirror photodimer. The monolayer packing arrangement of the amide (Figure 3b) contains molecules interlinked by N−H···O hydrogen bonds and whose C=C bonds are separated by about 5 Å, thus precluding photodimerization.

This approach has been made use of to demonstrate the ordering of water-soluble amphiphilic molecules at the air−aqueous solution interface and is described in section VI.I.

F. Catalytically Active Langmuir Films

Homogeneous catalysis by metal complexes plays a major role in chemical and biological processes. Such catalysts generally involve discrete metal complexes that function independently. The effect of crystalline order in Langmuir−Blodgett (LB) films on catalysis has been demonstrated by the behavior of LB films of a rhodium complex (Scheme 2c), [41] an analogue of a known hydrogenation catalyst. The LB films on glass support as well as the monolayer on aqueous solution catalyzed the hydrogenation of acetone in a dilute aqueous solution, yielding 2-propanol as the only observed product. The 2-D crystallinity of the monolayer of the rhodium complex on water was demonstrated by GIXD, albeit only a single Bragg reflection of 4.6 Å spacing was observed.

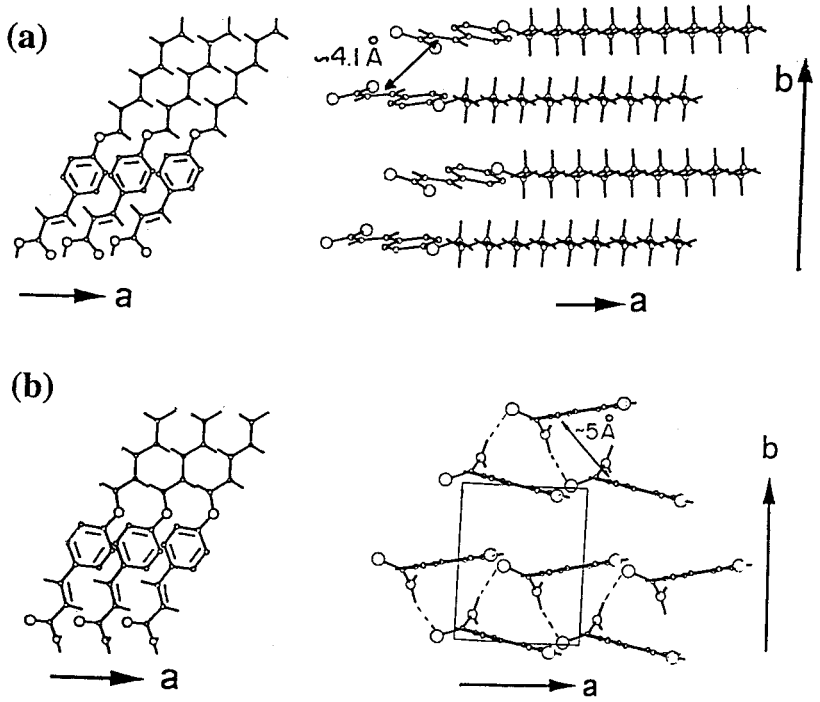

Figure 3. Packing arrangements of the uncompressed monolayers on water at 5 °C of $C_{18}H_{37}OC_6H_4CH{=}CHX$, viewed (left) parallel and (right) perpendicular to the water surface. (a) X = CO_2H (b) X = $CONH_2$. The upper chain section has been removed in some of the figures.

IV. Two-Component Monolayers

A crystalline monolayer on water composed of two different amphiphiles *A* and *B* may fall into one of the two categories: either *A* and *B* separate into different domains or do not. In the event of the latter, molecules *A* and *B* may be arranged in a random blend or if *A* and *B* complement each other form ordered *ABABAB*-type arrays. Various types of such binary systems have been studied on solid and liquid support. As we shall show below, it is possible to design binary amphiphilic systems which when composed of enantiomeric pairs of molecules separate into crystalline islands of opposite handedness. When *A* and *B* complement each other, as in acid−base systems, they may form ordered complexes. It is possible to engineer *A* and *B*, which may be different or very similar in structure, into separate territories of variable size.

A. Separation of Racemic Mixtures into 2-D Crystals

1. Introduction

The spontaneous separation of left- and right-handed molecules (i.e., enantiomers) from a racemic mixture has intrigued scientists since it was discovered by Pasteur a century and half ago. This phenomenon might have played a significant role in an abiotic process proposed to explain the transformation from a racemic chemistry to a chiral biology. In this regard, the separation of enantiomers in two dimensions may have relevance to the transfer of chiral information within or across an interface. This possibility prompted an investigation of the structural requirements for separation of left- and right-handed hydrophobic α-amino acids into 2-D crystalline arrays from a racemic mixture at the air−water interface.[22]

Unlike in 3-D crystals, the detection of spontaneous separation in two dimensions is not straightforward. The macroscopic methods of surface pressure−area isotherms, Brewster angle, and epifluorescence optical microscopy may not be sufficiently reliable for the purpose. Chiral segregation in 2-D crystals has been detected via techniques that probe the structure at the nanometer scale, such as scanning force[42] and scanning tunneling[43] microscopies and grazing incidence X-ray diffraction.[22,44]

Chiral discrimination of molecules in solution and in Langmuir films has been examined theoretically by Andelman, de Gennes, and Orland.[45,46] Their overall conclusion that heterochiral pair interactions should be generally favored should be relevant to dilute fluid phases but hardly to crystalline systems where multiple molecular interactions and crystal symmetry play a dominating role. We shall see that the occurrence of spontaneous resolution in 2-D crystals may depend on subtle differences in molecular structure.

Racemic mixtures of molecules tend to form 3-D crystals which embody centers of inversion or glide symmetry that relate chiral molecules of opposite handedness. As already discussed in section III.B, only translation or a glide but whose plane is perpendicular to the water surface are the symmetry elements common for 2-D crystals composed of amphiphilic chainlike molecules on water (see Figure 1b). Under such conditions, a racemic mixture can either resolve spontaneously into crystalline 2-D islands of opposite handedness in which the molecules are related only by translation symmetry or form a racemate in which the molecules are related

Scheme 3

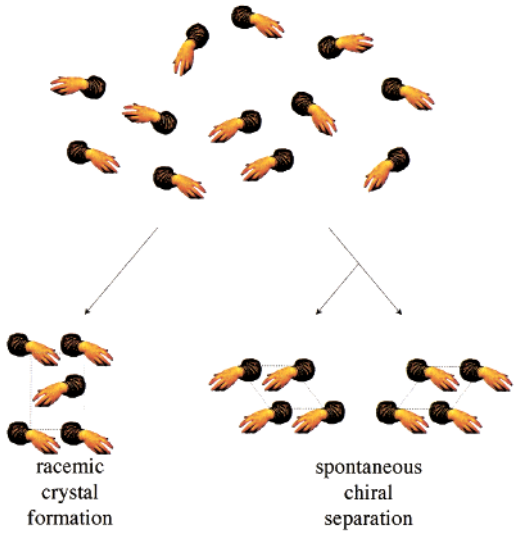

by glide symmetry, as depicted in Scheme 3 for a set of hands. If the glide can be prevented, spontaneous segregation of enantiomeric territories at the solution surface can be induced. However, since an amphiphile generally incorporates a long aliphatic chain $C_nH_{2n+1}-$, which tends to pack in the herringbone motif generated by glide symmetry, the molecule may require a functional group within the chain that, together with the hydrophilic group, will promote translation packing only.

2. α-Amino Acids

Reasoning along these lines was applied for obtaining enantiomeric segregation into 2-D islands of racemic mixtures of long-chain α-amino acids $^+H_3NCHXCOO^-$, where X is a long-chain side group,[22] by making use of the two common types of hydrogen-bonding layer motifs of the $^+H_3NCHXCOO^-$ moieties (Figure 4a). The motif in which the moieties are interlinked only by translation (Figure 4a, right) embodies axes of length appropriate for intermolecular N−H···O═C hydrogen bonding between secondary amide groups CONH introduced within the aliphatic X chains. Such chains cannot form favorable intermolecular N−H···O═C bonds in Figure 4a (left), since the herringbone arrangement of the chains, generated by glide symmetry, would preclude N−H···O linearity. Thus, the amide group within the hydrocarbon chain should induce the translation motif.

When X was chosen to be $C_nH_{2n+1}-$, n = 12, 16, the racemic mixture crystallized into heterochiral domains according to the GIXD pattern (Figure 4b, left) in a rectangular cell containing molecules related by glide in a herringbone arrangement of the chains (Figure 4a, left). The enantiomeric form yielded a GIXD pattern (Figure 4b, right) corresponding to molecules related by translation in an oblique cell (Figure 4a, right).

Enantiomeric separation was achieved by introducing into the chain an amide group, four CH_2 groups from the asymmetric atom C(HX), to form $C_nH_{2n+1}CONH(CH_2)_4$, n = 15, 17, 21. The enantiomeric form for n = 17 yielded a GIXD pattern (Figure

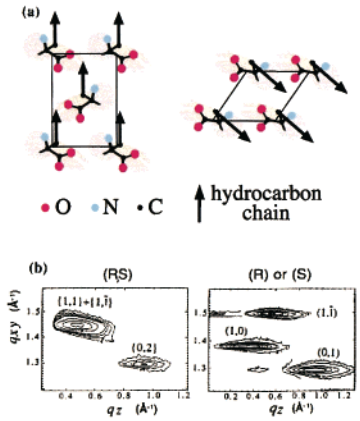

Figure 4. (a) Schematic views of the crystalline monolayer arrangements of α-amino acid amphiphiles $XCH(NH_3^+)CO_2^-$ (X = chain, depicted as arrow), showing: (left) molecules of opposite handedness (R and S) related by glide symmetry, and (right) molecules of a single handedness (R or S) related by translation. (b) The GIXD patterns, presented as 2-D intensity contour plots $I(q_{xy},q_z)$, of the monolayers of racemic, (R,S), and enantiomeric, (R) or (S), amino acid amphiphile $C_{16}H_{33}CH(NH_3^+)CO_2^-$ on water.

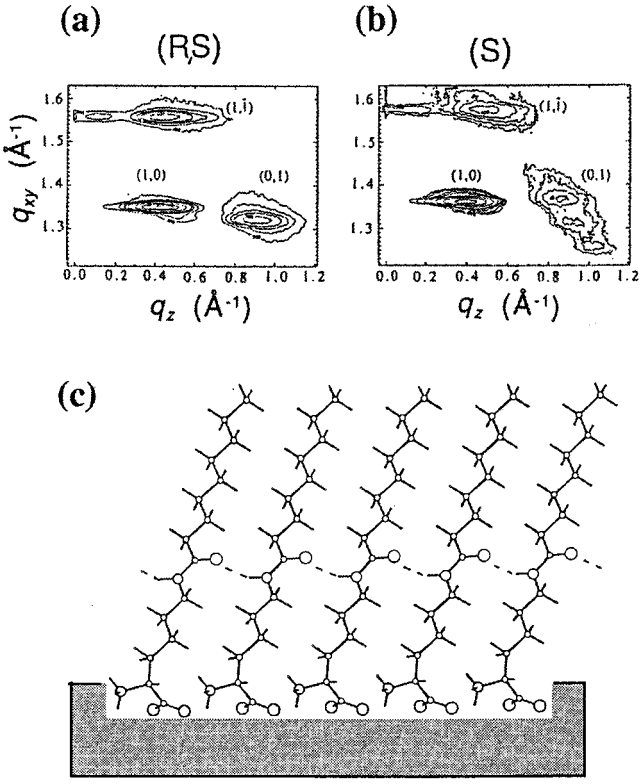

Figure 5. The monolayer crystals of racemic, (R,S), and enantiomeric, (R) or (S), α-amino acid amphiphile $C_nH_{2n+1}CONHC_4H_8CH(NH_3^+)CO_2^-$ n = 15, 17, 21 on water. (a,b) The GIXD patterns for the amino acid n = 17 in the form of two-dimensional intensity contour plots $I(q_{xy},q_z)$. (c) The packing arrangement of the racemic mixture n = 17 viewed parallel to the water surface. Upper chain section is not shown.

5b) indicative of an oblique unit cell with translation symmetry only. The GIXD patterns of the racemic mixture for the three monolayers n = 15, 17, 21 (as shown in Figure 5a for n = 17) are very similar to those of their corresponding enantiomeric form. Thus, the racemic mixture spontaneously separated into

homochiral domains of opposite handedness induced by N−H···O hydrogen bonding of the amide groups along a 5 Å axis, complemented by the N−H···O network of the $^{+}H_3NCHCOO^{-}$ moieties (Figure 5c).

The subtle interplay between the relative contributions of the hydrocarbon chain and the hydrogen-bonding amide and glycine groups in determining whether a racemic mixture will separate into monolayer islands of opposite handedness is brought to the fore by the example of the amphiphile X = $C_{29}H_{59}$-$CONH(CH_2)_4$−. Both the enantiomers and the racemic mixture of this system exhibit similar GIXD patterns, indicating molecular packing in a rectangular cell in the regular herringbone motif (Figure 1b right), generated by (pseudo) glide symmetry. Thus, in the racemic mixture the molecules of opposite handedness do not separate into different islands.

3. Monolayers of Diastereomeric Acid–Base Mixtures

Spontaneous separation of enantiomers of more complex monolayer systems has been achieved making use of acid−base interactions in 1:1 mixtures of long-chain substituted *R*- or *S*-mandelic acid [$C_{15}H_{31}$−C_6H_5−CH(OH)COOH] and *R*′- or *S*′-phenylethylamine [$C_{14}H_{29}$−C_6H_4−$CH(CH_3)NH_2$], which form crystalline monolayers on water,[47] depicted schematically in the central column of Scheme 4. The GIXD patterns of the *R*,*R*′- and *R*,*S*′-films (Figure 6) are distinctly different, in particular the intensity profiles of their Bragg rods (Figure 6b). An equimolar mixture

Scheme 4

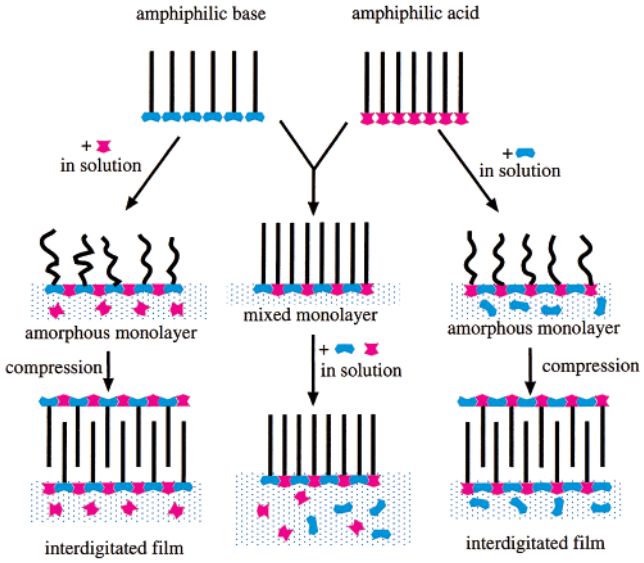

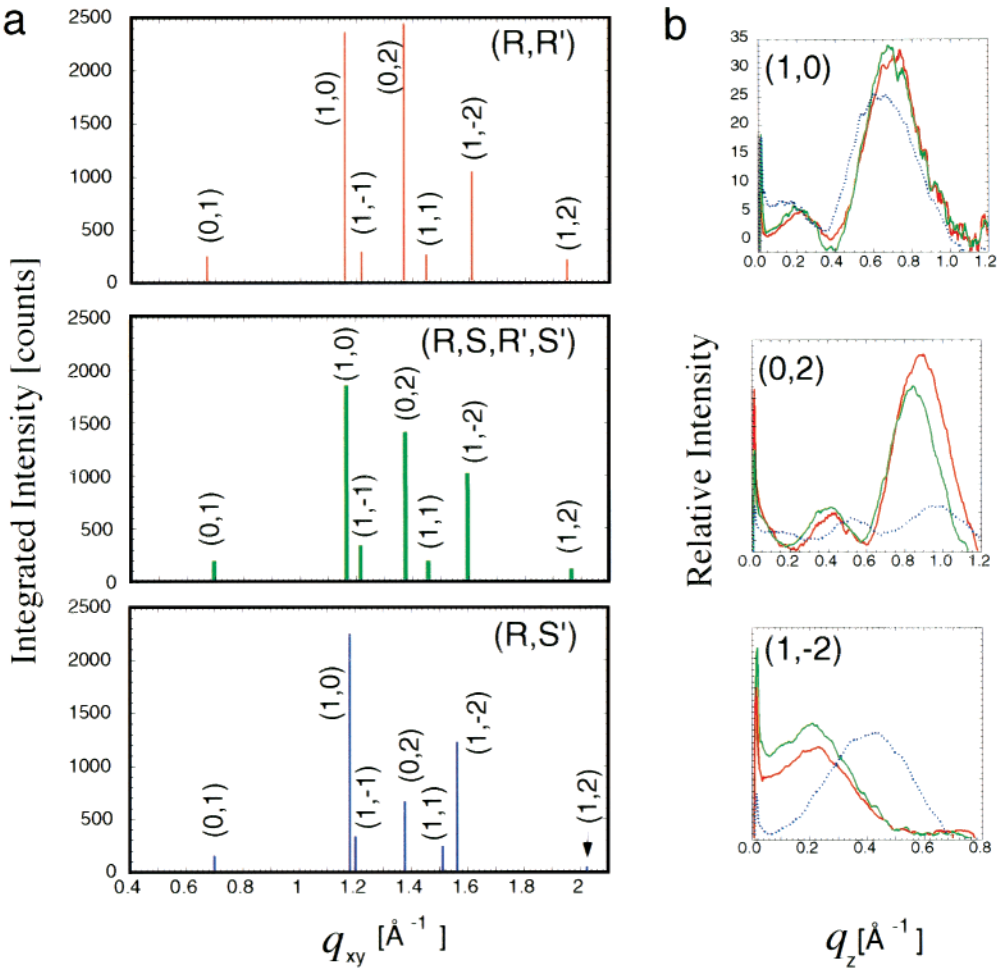

Figure 6. The GIXD patterns of the crystalline monolayers on water of the three mixtures, (R,R′), (R,S′), and (R,S,R′,S′) of $C_{15}H_{31}$−C_6H_5−CH(COH)COO^{-} and $C_{14}H_{29}$−C_6H_5−$CH(CH_3)NH_3^{+}$, in which their intensities are depicted in red, blue and green, respectively. (a) GIXD patterns of the three mixtures showing Bragg peaks $I(q_{xy})$ with their (h,k) indices. (b) Comparison of the Bragg rod profiles $I(q_z)$ of the (1,0), (0,2), and (1,−2) reflections of the three mixtures.

Scheme 5

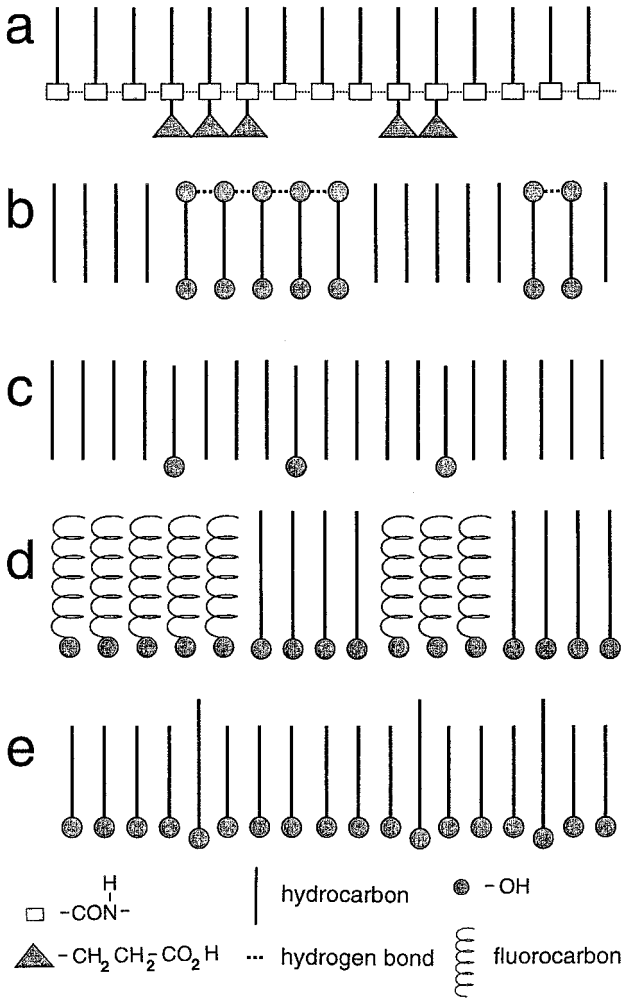

of the four components (*R,S,R′,S′*) gave rise to a diffraction pattern almost identical to that of the *R,R′*-mixture (see the Bragg rods in Figure 6b), signifying a separation of *R,R′*- and *S,S′*-territories. Studies involving nonracemic mixtures demonstrated, however, that mixing of the enantiomers can take place. Thus, the formation of an oblique 2-D unit cell containing one molecule only as in the systems studied by GIXD[22,44] does not rule out the presence of some enantiomeric disorder in the monolayer crystals.

B. Monolayer Film Domains of Variable Size

Engineering monolayer domains of variable size was motivated by attempts to get a measure of the limiting size of 3-D crystal nuclei whose formation is induced by epitaxial growth from amphiphilic monolayers (vide infra). The idea involved the preparation of *A*-type domains of variable size within a monolayer sea of *B* molecules, where only the *A*-domains induce the crystal precipitation whereas the *B*-domains are inactive. This aim was achieved in ways shown in Scheme 5a−e. In Scheme 5a, amphiphiles *A* and *B* each contain the common moiety $C_{19}H_{39}CONH$. This hydrogen-bonding amide group and the hydrocarbon chain provide the driving force for a continuous network as confirmed by GIXD measurements. The headgroup of *A*, $-(CH_2)_2CO_2H$ was found to both favor segregation and induce crystallization of a metal−carboxylic acid salt as shall be described in section VI.E.

A similar approach for gleaning information on the size of ice nuclei as induced by monolayers of aliphatic alcohols (see section VI. A.2) involved mixtures of diols $HO(CH_2)_nOH$ and alkanes $H_3C(CH_2)_nCH_3$ (Scheme 5b). In these mixed systems the concept was that intralayer OH···O bonds between diol OH groups exposed to air would promote aggregated islands of diols within the sea of alkane molecules. A combination of infrared measurements sensitive to intermolecular environment, ice nucleation experiments, and GIXD data confirmed this model.[48] Replacement of the diol by an alcohol induced a random solid solution (Scheme 5c), as expected. Segregated domains of the mono alcohols $C_nH_{2n+1}OH$ were obtained by using the fluorocarbon alcohol $C_mF_{2m+1}C_2H_4OH$ as the *B*-type molecule (Scheme 5d). It was not possible to reduce the *A*-type hydrocarbon domain size below about 100 Å. The alcohol $C_nH_{2n+1}OH$ domains can be effectively reduced in size by addition of low concentrations of the longer chain $C_mH_{2m+1}OH$, $m = n + 4$, to the host system (Scheme 5e), which then intercalates within the $C_nH_{2n+1}OH$ domains at random sites with the end CH_2CH_3 and CH_2OH groups emerging from the layer and so form point defects.[49]

V. Interactions between Amphiphilic Monolayers and Solution Subphase

The focus below on the interaction between the hydrophilic headgroups of ordered monolayers and the liquid subphase, such as water, solutes, and ions, has a bearing on many processes. For example, the interfacial region between a charged surface and an electrolyte is central to electrodeposition, ion transport through biological membranes, preparation of Langmuir−Blodgett films, and biomineralization. The studies presented are also a prelude to a discussion on induced nucleation of 3-D crystals by monolayers as templates. With undersaturated solutions of such ions or solutes, it is possible to glean, from their binding to the monolayer, information on the way a nucleating crystal's first layer might be formed. Amphiphilic monolayers on solution surfaces are also an ideal vehicle to study the effect of solvent on 2-D and, by extension, 3-D crystal growth and dissolution.

We have limited the discussion in this section to those systems that have been characterized by GIXD. Supramolecular hydrogen-bonding architectures at the monolayer−solution interface investigated by Ringsdorf, Kunitake, and others shall be described in section VIII.A

A. Binding of Solvent and Solute to Monolayers

Specific interactions between hydrophilic headgroups of an ordered monolayer and the pure water subphase may be deduced by comparative results on long-chain alcohols and alkanes. For example, the monolayer packing arrangements on water of the alcohols[21] $C_nH_{2n+1}OH$, $n = 31-15$, are compatible

Scheme 6

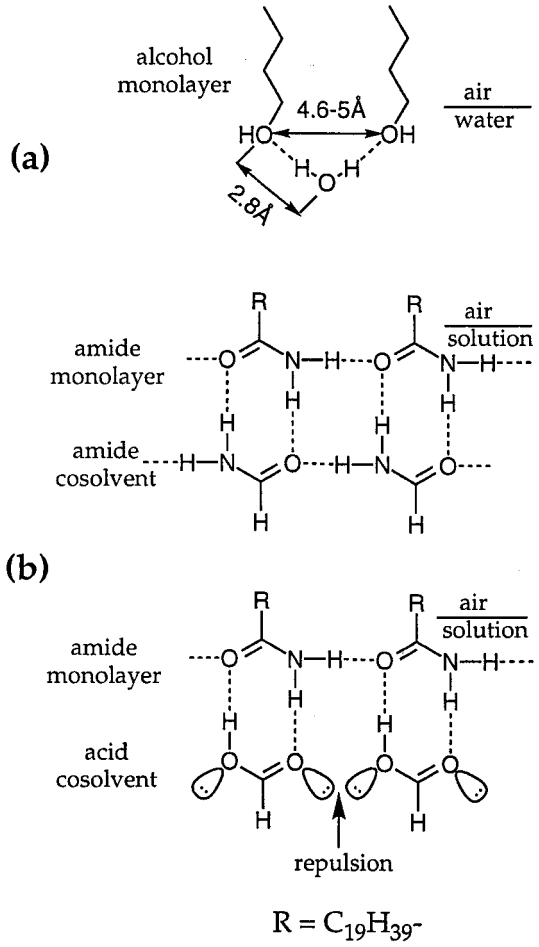

with ordered binding between the alcohol OH groups and a layer of water (Scheme 6a). The distances between neighboring alcohol OH groups range from about 4.6 to 5.0 Å, which allow water molecules to form hydrogen-bond bridges between neighboring OH groups. This model is supported by a comparison between the monolayer arrangements of the alcohols and several long-chain alkanes.[50] Both types of molecules form the herringbone motif; the alkane chains are untilted, whereas the alcohol chains are tilted from the normal to the water surface by angles ranging from 10° to 20°. The chains of alcohol−alkane mixtures of the same length are untilted. More direct evidence that the monolayers of long-chain alcohols interact with the water molecules comes from nonlinear optical measurements, according to which an ordered layer of water is bound to the monolayer,[51] as well as the observation that the alcohol monolayers promote ice nucleation,[30,52,53] discussed in section VI.A.

The interaction of a monolayer of hexacosanoic acid ($C_{25}H_{51}COOH$) with aqueous solution (containing up to 1 M HCl or 1 M NaOH) was studied by Shen and co-workers,[53] making use of sum-frequency vibrational spectroscopy. At a pH up to about 7, the carboxyl group is neutral. The O−H bond of the carboxyl group above pH 3.5 orients to adopt an antiplanar O=C−O−H conformation, perhaps to form a hydrogen bond with a carboxyl group of a neighboring molecule.

Introducing cosolvents to water such as formamide or formic acid can have a pronounced effect on monolayer crystallinity and packing of aliphatic amides and carboxylic acids in view of the hydrogen bonding between the amphiphile and cosolvent.[54] Concentrated solution of formamide as subphase can induce a change in packing of some aliphatic amides. Replacing formamide by formic acid was found to inhibit the monolayer crystalline formation of arachidamide $C_{19}H_{29}CONH_2$. The essential difference in binding of formic acid and formamide to the amphiphile involves the replacement of an N−H···O bond between monolayer-bound formamide molecules by O(hydroxyl)···O(carbonyl) repulsion between lone-pair oxygen electrons of the formic acid molecules (Scheme 6b). Pure formamide as the liquid subphase instead of water has no observable effect on the monolayer packing of long-chain alcohols. On the other hand, it induces the chains of the fatty acid $C_nH_{2n+1}COOH$, $n = 29$, to be aligned normal to the liquid surface unlike the highly tilted orientation on a water subphase[55] and the amide $n = 19$ to form multilayers which will be discussed in section VII.A.

Solutes can not only inhibit or retard formation of monolayer crystallites but also dissolve them as found when β-alanine, $^+H_3NC_2H_4CO_2^-$, as solute caused the disappearance of monolayer crystals of a perfluorinated α-amino acid surfactant after 2 h[56] (Figure 7a). This process was rationalized in terms of a strong interaction between β-alanine with the amino acid headgroups of neighboring amphiphilic molecules, leading to intercalation and thus destruction of the crystallites (Figure 7b,c).

Amphiphilic monolayer formation on a liquid mercury surface has been studied by GIXD and X-ray reflectivity.[57,58] Both methods applied to a clean liquid mercury surface revealed a liquidlike in-plane arrangement of the Hg surface atoms, atomic layering parallel to the surface plane which decays into the bulk after a few atomic diameters, and sub-Angstrom roughness. A monolayer of stearic acid on liquid Hg displayed two weak GIXD peaks.[59] Alkanethiol $C_nH_{2n+1}SH$, ($n = 16$, 18, 22, 30) monolayers on liquid mercury were found to be densely packed but, paradoxically, with no long-range order, according to surface X-ray scattering data.[60] This result was explained in terms of a strong interaction of the thiol group with the underlying disordered mercury layer dominating over the order-promotion interactions of the alkyl chains. One should also note that the area per Hg atom in the surface liquid layer is about one-half that of the alkanethiol chain of about 19 Å^2. Thus, only one-half the number of surface Hg atoms can be covalently bound to the disordered alkanethiol chains of the monolayer.

B. Detection of Ordered Ion Binding to Monolayers

X-ray reflectivity measurements have demonstrated that metal ions, when present in solution, lie close to the charged headgroups of the monolayer at the interface. Such an arrangement, however, does not necessarily imply that the metal ion distribution

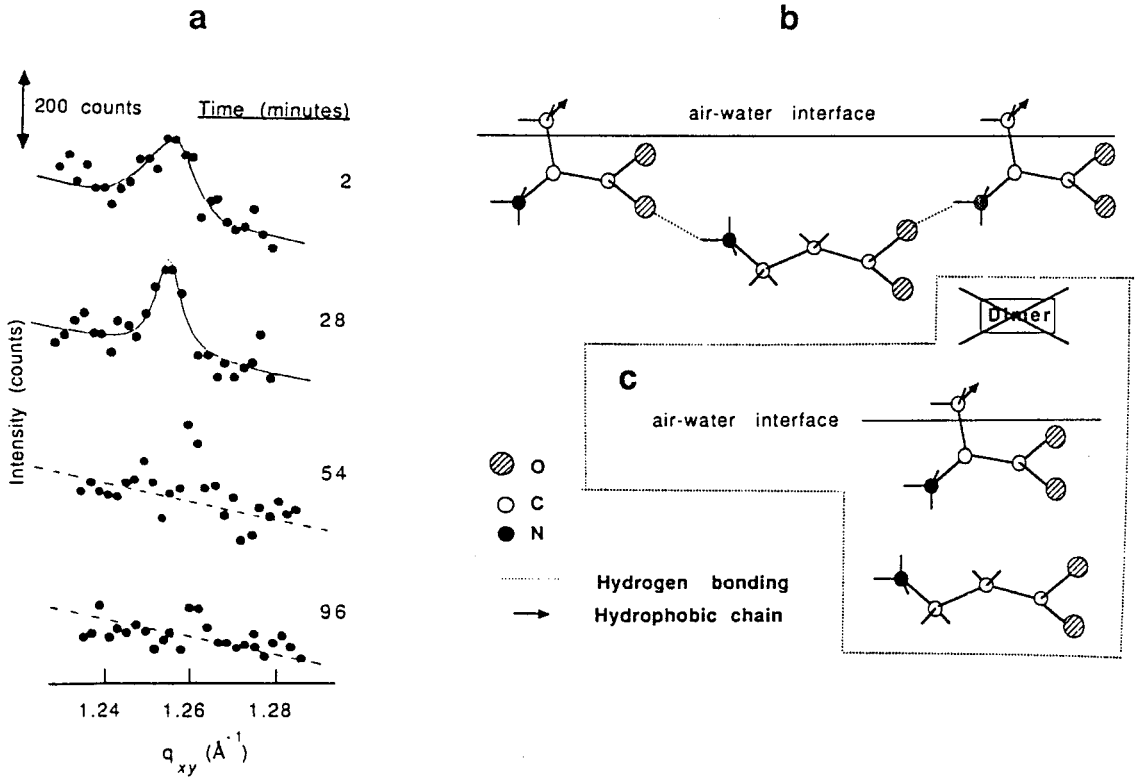

Figure 7. Monolayer of $C_{10}F_{21}C_2H_4OCOCH_2CH(NH_3^+)CO_2^-$ over a β-alanine solution. (a) Bragg peak measurements as a function of time after spreading the amphiphile. (b) Schematic drawing of "bridging complexes" between the amphiphiles and the β-alanine solute molecules in which the latter intercalates between neighboring amphiphilic headgroups.

in contact with the charged ordered surface is crystalline. A direct demonstration of an ordered counterionic layer first came from a GIXD study of uncompressed cadmium arachidate monolayers over an alkali aqueous subphase, using ammonia as base.[27,28] The GIXD pattern (Figure 8a, left) showed 10 Bragg peaks, 7 of which arise from the cadmium layer only, belonging to a 2 × 3 supercell of the arachidate subcell. X-ray reflectivity measurements yielded a molar ratio of cadmium to arachidate of 1:1, implying that the counterionic layer consists of $CdOH^+$ ions. Refined Cd positions in the supercell (Figure 8a, right) gave a very good fit to the observed GIXD data (see inset, Figure 8a). Another example of supercell formation, as a result of binding of Cu^{2+} ions to glycine headgroups and thus indicative of an ordered arrangement of the Cu^{2+} ions, was found in the monolayer structures of some enantiomerically pure α-amino acid amphiphiles on copper acetate solution. [61]

The absence of a supercell in monolayer structures composed of long-chain carboxylic acids and amino acids bound to metal ions at the air−solution interface does not imply that the metal ions are disordered. Bragg rod data analyses appear to reveal the presence of ordered binding of K^+ to the amino acid[56] and Ca^{2+} ion to arachidic acid.[29] More direct evidence has come from a GIXD study of arachidic acid on a $Pb(NO_3)_2$ solution that has yielded the presence of monolayer-bound Pb ions arranged in a 2-D lattice commensurate with the arachidate lattice. The relationship between the arachidate and Pb lattices is presented in Figure 8b.[62]

C. In-Plane Attachment of Water-Soluble Complexes to Langmuir Films

A model involving intercalation of β-alanine solute molecules within α-amino acid monolayer crystallites has been presented above. Here we describe evidence in favor of peripheral attachment of water-soluble complexes to crystalline monolayer films using chirality as a probe.[61] The monolayer of the amphiphile S-$C_{15}H_{31}CONH-C_4H_8CH(NH_3^+)COO^-$, having been formed on a copper acetate solution, exhibits a more expanded pressure−area isotherm when pure alanine, serine, or valine of S' rather than of R' configuration is injected into the subphase. We explain this phenomenon in terms of a more satisfactory attachment of the water-soluble $S'-Cu-S'$ complex units to the periphery of monolayer crystals of complex units $S-Cu-S'$, as opposed to $R'-Cu-R'$ bound to the monolayer $S-Cu-S'$, as depicted in Scheme 7.

VI. Induced Nucleation of 3-D Crystals by Langmuir Monolayers

Heterogeneous crystal nucleation is a frequently observed process that takes place at an interface, thus lowering the activation barrier for nucleation. The interaction between the nucleus and the interface can range from nonspecific adsorption to epitaxial growth. Here we focus on the use of synthetic monolayer templates composed of amphiphilic molecules whose polar headgroups in contact with the aqueous solution subphase are expedient crystal nucleating agents through a structural complementarity between the polar headgroups and a layer of

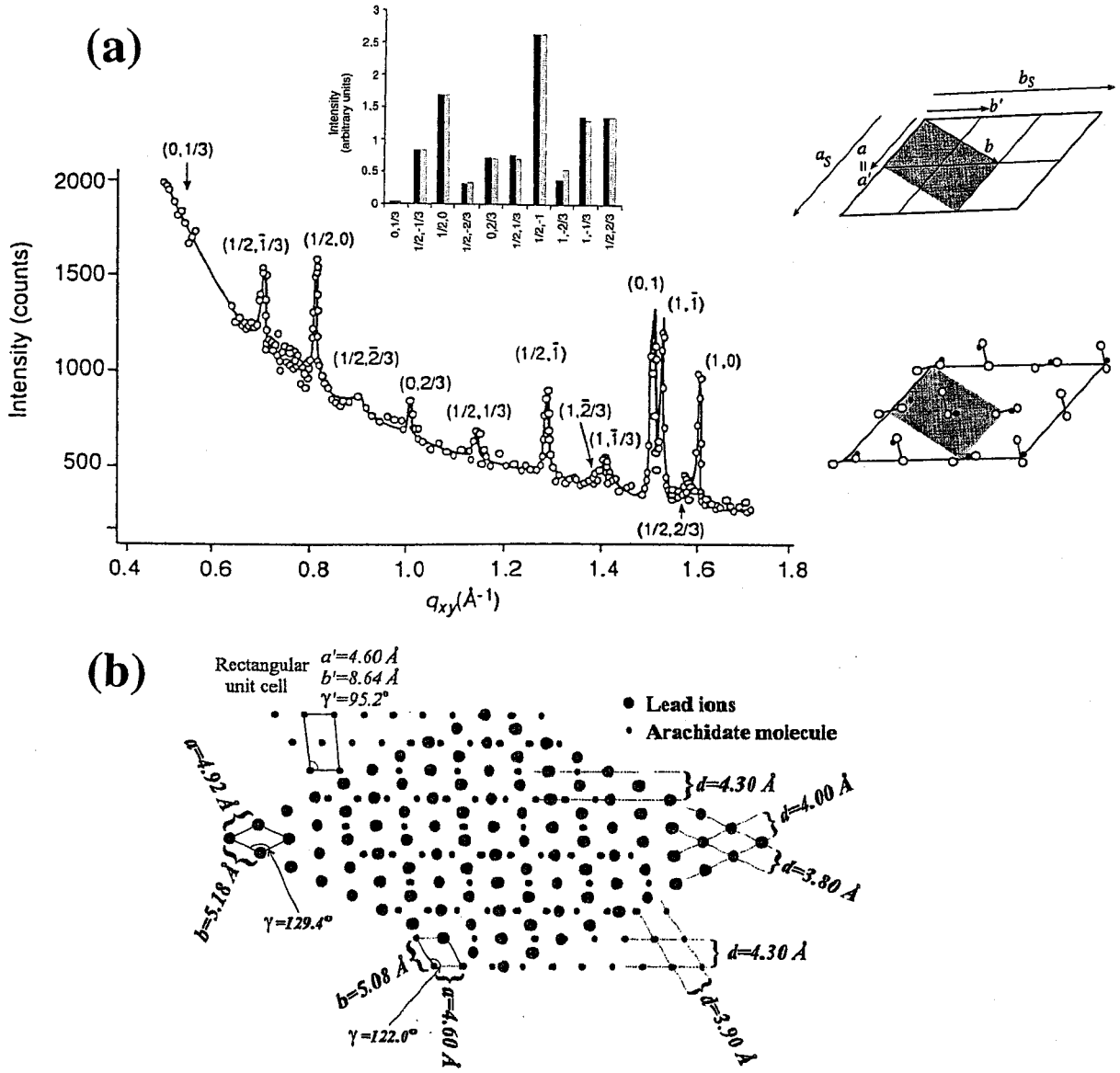

Figure 8. (a) Arachidic acid, $C_{19}H_{39}COOH$, monolayer over a $CdCl_2$ subphase (pH 8.8) at 9 °C. The observed GIXD peaks $I(q_{xy})$ and the (h,k) reflection assignment is shown on the left. The three reflections with integer indices (1,0), (0,1), (1−1) correspond to scattering from the arachidic moieties in an $a'b'$ subcell shown on the right; the reflections with fractional indices correspond to scattering from the bound Cd layer in a supercell $a_s = 2a'$, $b_s = 3b'$. The arrangement of carboxylate groups (dumbells) in the arachidate repeat cell (shaded area) $\boldsymbol{a} = \boldsymbol{a}'$, $\boldsymbol{b} = \boldsymbol{a}' + 2\boldsymbol{b}'$ and of Cd ions (as black dots) in the 2×3 supercell is shown on the right. The Cd ion arrangement yields calculated intensities (grey) that compare well with the observed GIXD intensities (black) as shown in the inset on the left. (b) Arachidic acid on a $Pb(NO_3)_2$ solution. The two lattices arising from arachidic acid (small dots) and from the Pb ions (large dots). The two unit cells are commensurate.

the to-be-nucleated crystal (see Scheme 1, left). With this method it is possible to obtain some insight into the nucleation process as well as a measure of control on the size and orientation of the precipitated crystals. Studies along these lines have yielded information on the limiting size of crystal nuclei, the interplay between the orientation of the nucleating polar headgroups, and the nucleation process, biological mineralization, and oriented formation of semiconductor nanocrystals.

A. Induced Nucleation of Ice via Alcohol Monolayers

Pure water can be supercooled to temperatures below −20 °C. Therefore, the inhibition or induction of freezing of water into ice, in particular through the role of auxiliaries, has far-reaching ramifications for the living and nonliving world. Promotion of ice nucleation has been exploited in the induced precipitation of rain by silver iodide seeded in clouds. Ice nucleation, on the other hand, can result in wide-scale damage to nonconiferous plants in temperate climates by frost bacteria, which promotes ice nucleation, preventing supercooling of water below −2 °C.

Various considerations suggested that water-insoluble long-chain aliphatic alcohols $C_nH_{2n+1}OH$ would promote ice nucleation. For example, there is a close lattice match between the arrangement of oxygen atoms in the *ab* layer of hexagonal ice (Figure 9a) and of the oxygen atoms in the alcohol molecules packed in the herringbone arrangement of unit cell dimensions 5×7.5 Å^2 (Figure 9b). Indeed, alcohol

Scheme 7

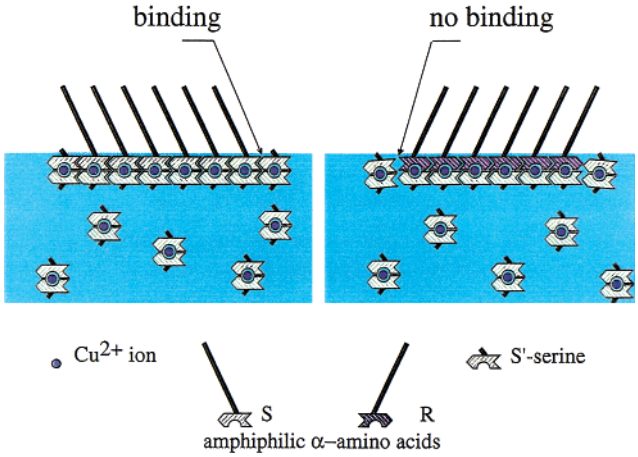

films of the series $C_nH_{2n+1}OH$, $n = 13-31$, were found to catalyze ice nucleation[52,53] (Figure 10). The induced freezing into ice for n odd reaches an asymptotic temperature just below 0 °C for an upper value of $n = 31$; the freezing temperature for n even reaches a plateau of −8 °C for n in the range 22−30. The catalytic action of the alcohol monolayers was also demonstrated by the time taken to freeze supercooled water drops kept at fixed temperatures and covered by a monolayer of $C_{30}H_{61}OH$.[63]

The epitaxial nature of the induced ice nucleation from an essentially single crystal of the $C_{31}H_{63}OH$ monolayer was demonstrated by an electron diffraction pattern[64] (Figure 11a). GIXD studies of self-assembled monolayers of the alcohols $C_nH_{2n+1}OH$, $n = 13-31$, on water at 5 °C revealed detailed information that could be correlated with the ice freezing behavior.[21,30] For example, the epitaxial relation between ice and the alcohol monolayer of

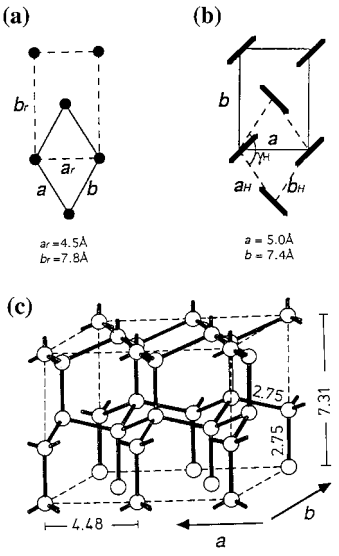

Figure 9. (a) Schematic representation of a,b layer of hexagonal ice in terms of the hexagonal cell (a,b) and of a c-centered rectangular cell (a_r,b_r). (b) Schematic representation of the herringbone packing of hydrocarbon chains $C_n H_{2n+2}$ in a rectangular cell (a,b), viewed along the chain axis. The distorted hexagonal representation of the cell (a_h,b_h) is also depicted. (c) Three-dimensional structure of hexagonal ice showing oxygen atoms interlinked by hydrogen bonds (bold lines).

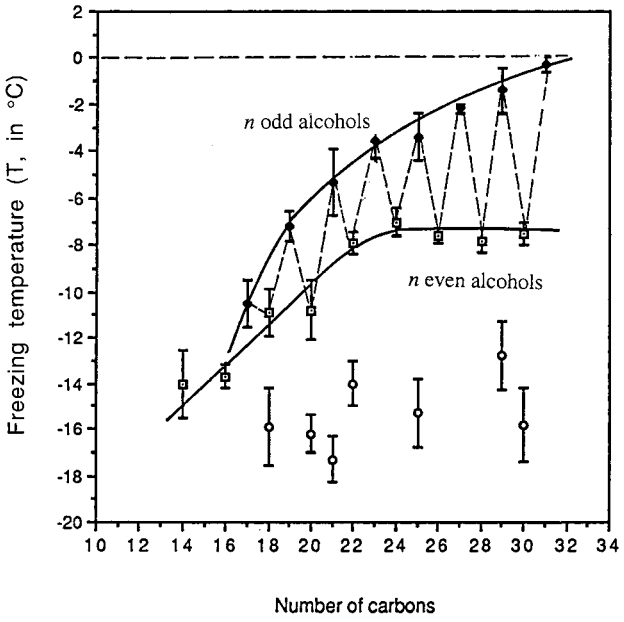

Figure 10. Freezing temperatures (T) of supercooled water drops covered by monolayers of amphiphilic alcohols $C_nH_{2n+1}OH$ (rhombs and squares) and carboxylic acids $C_nH_{2n+1}COOH$ (open circles). Curves are drawn separately for alcohols with n odd (filled rhombs) and n even (open squares).

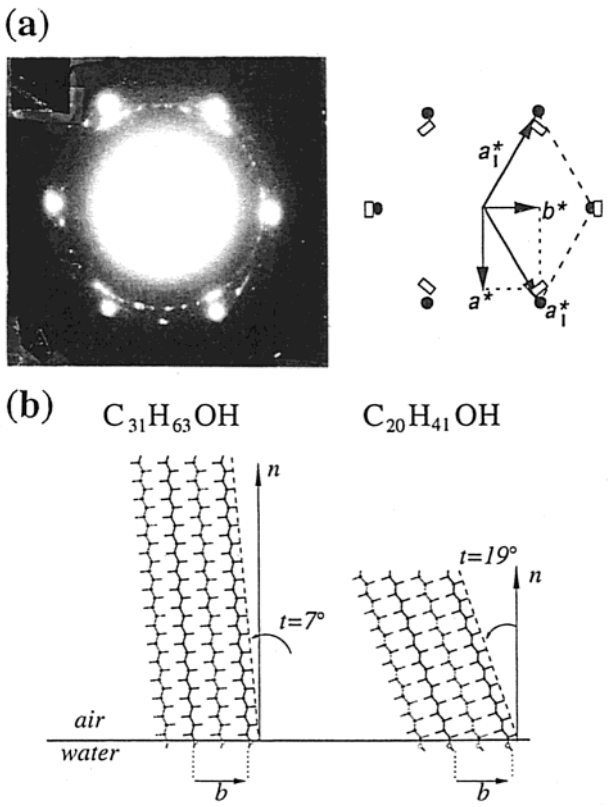

Figure 11. (a) Electron diffraction pattern from an essentially single crystallite of the $C_{31}H_{63}OH$ monolayer on a single crystal of hexagonal ice and the relation between the reciprocal lattice of ice and of the monolayer, showing the six {1,0,0} reflections of ice (circles) and the four {1,1} and two {0,2} reflections of the monolayer (rectangles). (b) Monolayer crystalline arrangements of alcohols $C_nH_{2n+1}OH$, $n = 31$, 20 viewed perpendicular to the glide plane. Molecules related by glide symmetry are in full and dotted lines, respectively.

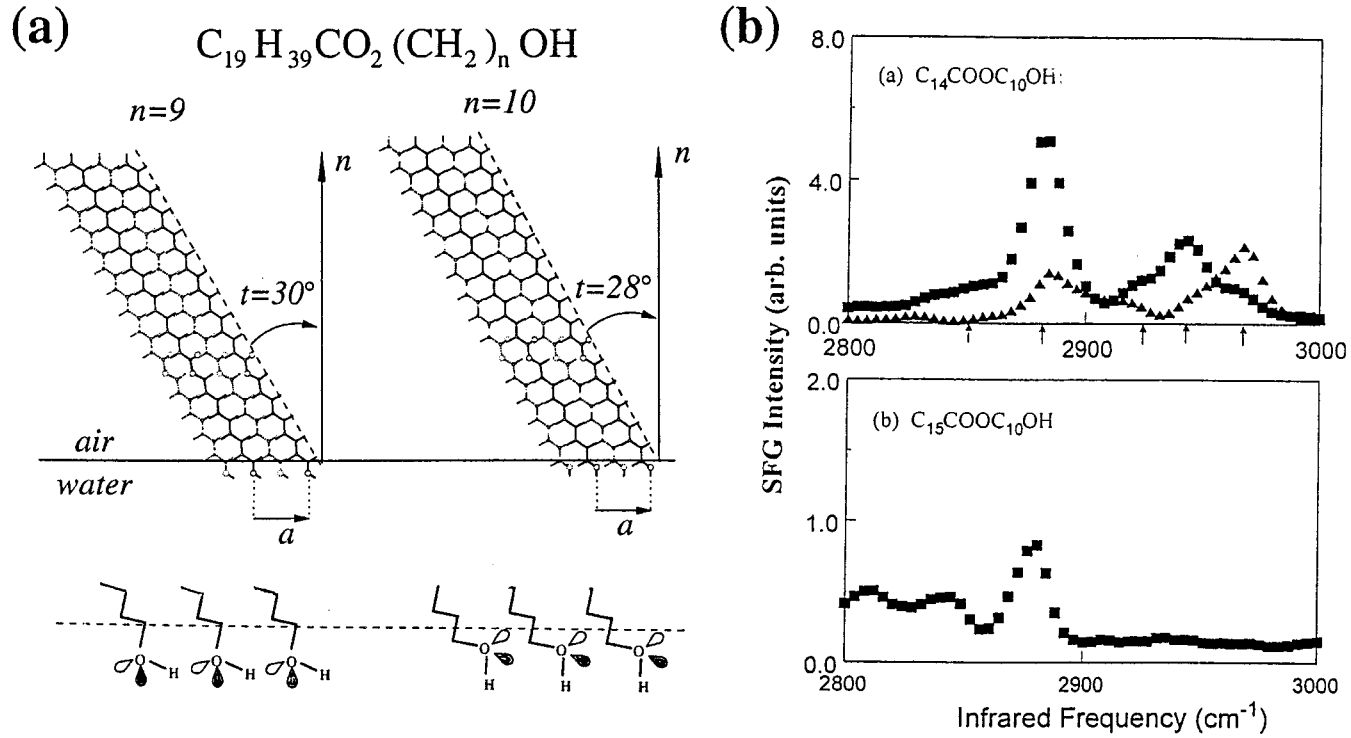

Figure 12. (a) Monolayer crystalline arrangements of the hydroxyl alkyl esters $C_{19}H_{39}CO_2(CH_2)_nOH$ $n = 9$, 10 showing their different C−OH groups orientations. (b) Infrared-visible sum-frequency spectra of monolayers of $C_mH_{2m+1}CO_2(CH_2)_{10}$-OH $m = 14$, 15 on water. The difference in the spectra of the two monolayers arises from the difference in tilt of their $C-CH_3$ bonds.

$C_{31}H_{63}OH$, which is an excellent ice nucleator, is obvious from the similarity between the arrangement of oxygen atoms in the (001) layer of ice and in the alcohol monolayer (vide infra, Figure 13e), the packing arrangement of which is shown in Figure 11b, left. The alcohols crystallize in a rectangular cell, with the chains adopting the herringbone motif as in Figure 1c, right. There is a gradual change in crystal structure with chain shortening that may be correlated with poorer ice nucleation behavior. The molecules become more tilted (see Figure 11b), and there is an increase in lattice area mismatch between ice and the alcohol monolayer, a significant increase in chain motion, and a reduction in the relative amount of alcohol crystalline material formed and in their extent of lateral order.[22] We compare this behavior with monolayers of short-chain alcohols $C_nH_{2n+1}OH$, $n = 8-13$, in equilibrium with macroscopic liquid drops of the alcohol on water, studied by Berge and co-workers[7,65,66] that exhibit remarkable coherence lengths of mm size.

The odd−even effect in the ice-nucleating behavior of $C_nH_{2n+1}OH$ and the GIXD data implies that the absolute azimuthal orientation of the hydrocarbon chains differing in length by one CH_2 group are the same, leading to a difference in orientation of their CH_2OH groups. The absolute orientation of the molecular chains, and thus of the $CH_2O(H)$ groups, was established in the series $C_mH_{2m+1}CO_2C_nH_{2n}OH$, $m = 14$, 15, 19, $n = 9$, 10, by GIXD (see Figure 12a for $m = 19$, $n = 9$, 10) complemented by lattice energy calculations[30] and independently by infrared−visible sum frequency generation (Figure 12b).[67] This optical method fixed the tilt angle of the terminal $C-CH_3$ bond and thus the absolute azimuthal orientation of the molecular chain. In the monolayer packing arrangements of $C_{19}H_{39}CO_2(CH_2)_nOH$, $n = 9$, 10 (Figure 12a), the O−H bond and the lone-pair electron lobes are equally exposed to water for $n = 9$ whereas for $n = 10$, which is the better ice nucleator of the two, the O−H bond can point vertically into the water subphase. This model was confirmed from an assignment of the absolute azimuthal orientation of the bromo alcohols $BrC_nH_{2n}OH$, $n = 21$, 22 on water, determined directly from an analysis of the GIXD data.[67]

A lattice match is not the only determining factor for induced crystal nucleation For example, compressed monolayers of the alcohol $C_{18}H_{37}OH$ induces nucleation of gypsum ($CaSO_4 \cdot 2H_2O$) from its {010} face.[68] The crystal structure is composed of layers of Ca^{2+} and SO_4^{2-} ions interspersed with a double layer of water molecules, parallel to the {010} face. There is no lattice match between the alcohol monolayer and the layer structure of gypsum, suggesting that overall hydrogen bonding between the alcohol hydroxyl and the sulfate groups induced the oriented nucleation.

1. Critical Size of the Ice Nucleus

An estimate of the critical size of ice nuclei as induced by an alcohol monolayer, just below 0 °C, was gleaned from a GIXD study monitoring growth of (001) plates of ice by a $C_{31}H_{63}OH$ monolayer[69] (Figure 13a−d). Many of these ice crystals had a lateral coherence length as low as 25 Å, as determined from the width of the (100) reflection of ice (Figure 13d). This value of 25 Å compares well with the domain diameter of about 30−35 Å, over which there is a match to within 0.5 Å between the oxygen positions

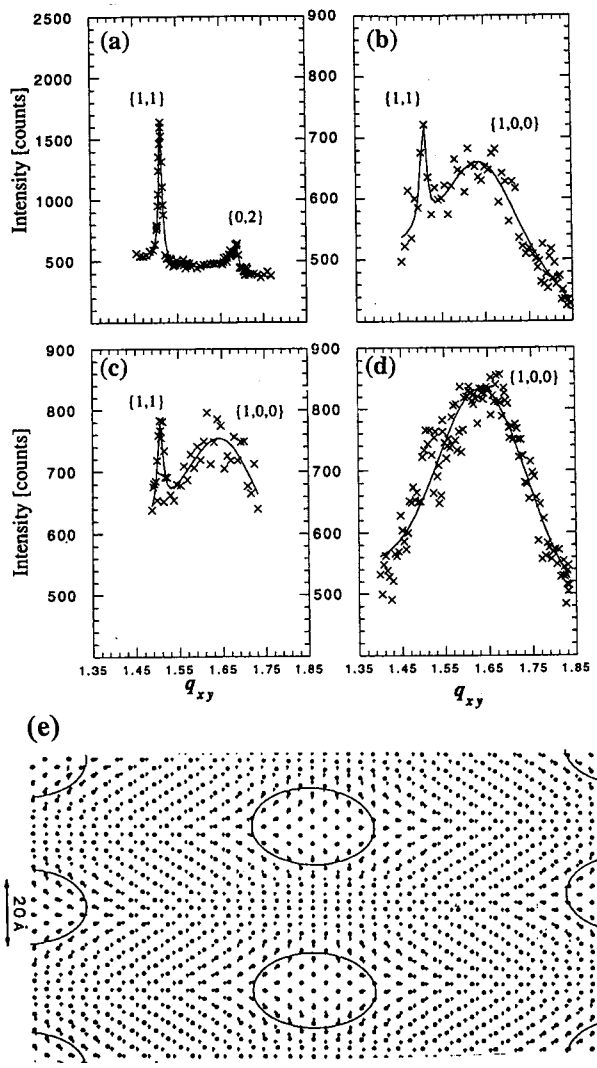

Figure 13. GIXD measurements made on a monolayer of $C_{31}H_{63}OH$ over pure water cooled to freezing. (a) The Bragg peaks {1,1} and {0,2} of the monolayer on water at 4 °C. (b) First stage of ice nucleation just below 0 °C under the monolayer. The {1,1} Bragg peak of the monolayer and the (100) Bragg peak of ice are visible. (c) Same as part (b) but after a time interval of 15 min. (d) After a further 15 min only the (100) Bragg peak of ice is visible. The disappearance of the Bragg peaks of the crystalline monolayer was not due to its destruction, but rather because the ice crystals bound to the monolayer were no longer parallel. The q_{xy} values are in $Å^{-1}$units. (e) A diagram of the oxygen positions within the *ab* layer of hexagonal ice (triangles in a rectangular unit cell of 4.5 × 7.8 $Å^2$) superimposed on the oxygen positions in the monolayer of $C_{31}H_{63}OH$ (squares in a rectangular cell of 5.0 × 7.5 $Å^2$). Within each ellipse the oxygen atoms of ice and the monolayer match to within 0.5 Å.

of the *a*,*b* lattice of ice and that of the $C_{31}H_{63}OH$ monolayer on water (Figure 13e). A value of about 30 Å was also obtained as the calculated size of 'defect-free' domains in a monolayer of $C_{29}H_{61}OH$ in a study simulating the observed ice nucleating efficiency of $C_{29}H_{61}OH$ when contaminated with tailored additives (see Scheme 5e).[49] Thus, an assumed maximum diameter of the ice critical nucleus of 30 Å would constitute a hemisphere containing about 250 molecules of water. This analysis also suggests that for a homogeneous ice nucleation just below 0 °C, the number of water molecules in a critical

Scheme 8

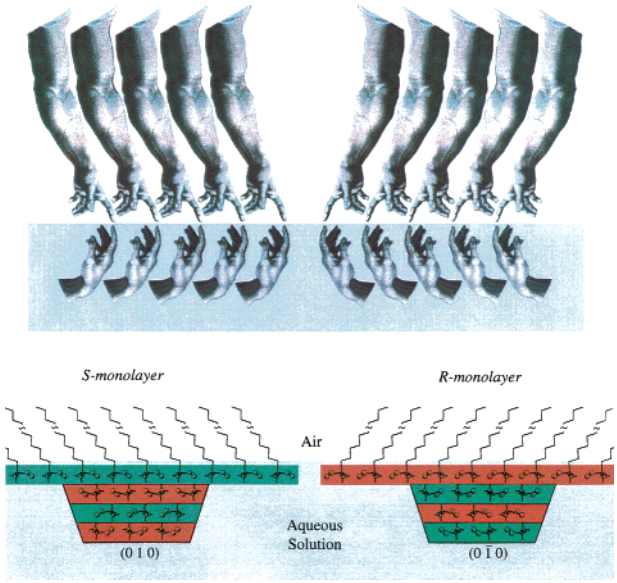

nucleus is unlikely to be less than 500. According to electron diffraction studies of clusters of water molecules formed on expansion through a nozzle, the crystalline ice core formed in a water cluster had a diameter of about 45 Å containing about 1200 water molecules.[70] These results suggest that the alcohol monolayer reduces the effective diameter of the critical ice nucleus.

2. Ordered Alcohol Monolayers at the Oil–Water Interface

The induced ice-nucleation behavior was exploited to probe the oil−water interface: the freezing temperatures of water drops placed in hexane solutions of the alcohols $C_nH_{2n+1}OH$, $n > 22$, were sufficiently high to indicate that the alcohols aggregate into crystalline clusters at the oil−water interface.[53] A direct observation of monolayer amphiphilic crystallinity at the oil−water interface by GIXD of $C_{10}F_{23}(CH_2)_2OH$ at the water−hexane solution interface was made by Schlossman et al.[71] Below the transition temperature the monolayer is in a high-density ordered phase, whereas above the transition point the monolayer desorbs into the hexane solution. Another observation of monolayer crystallinity at the oil−water interface was carried out by Brezesinski et al.: They showed that monolayers of phospholipids at the air−water interface in contact with hexadecane and dodecane are crystalline, with a reduction of the tilt angle of the aliphatic chains compared to films at the pure air−water interface.[72]

B. Amino Acid Monolayer Template for Glycine Crystallization

The opposite faces of a centrosymmetric crystal that are chiral, and thus of opposite handedness, may be used as an advantage to demonstrate epitaxial nucleation by an ordered monolayer composed of amphiphilic molecules of a single handedness. Scheme 8, top, depicts a layer of left hands in contact at an interface with an underlying layer of right hands; by symmetry, the layer of right hands make equivalent

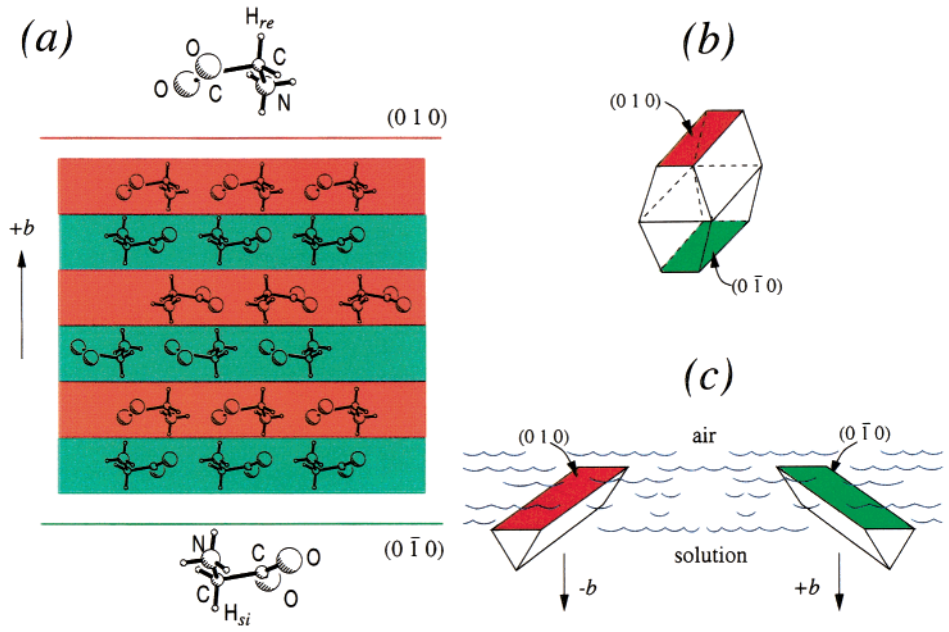

Figure 14. (a) Packing arrangement of the α-form of glycine. The red and green colors define the chiral layers, and crystal faces, of opposite handedness. (b) Bipyramidal crystal morphology of the pure form of α-glycine from aqueous solution. (c) Schematic view of crystals of α-glycine of pyramidal shape obtained when grown under monolayers of (left)*R*, and (right)*S*, α-amino acid amphiphiles, respectively.

contact with the layer of underlying left hands. These arrangements are analogous to a floating layer of water-insoluble 'left-handed' molecules, which induces nucleation of a top crystal layer of right-handed molecules at the air−solution interface and, by symmetry, the Langmuir layer of right hands which induces formation of the enantiotopic crystal face composed of left hands. This principle was applied to the induced nucleation of the opposite enantiotopic {010} faces of the α-form of glycine, $^{+}H_3NCH_2CO_2^{-}$. The crystal structure (Figure 14a) contains hydrogen-bonded *a*,*c* layers in which the molecules are related by translation only. These layers are interlinked on one side by hydrogen bonds to form a centrosymmetric bilayer and on the other side by C−H···O contacts. Glycine crystallizes from aqueous solution in the form of truncated bipyramids in which the opposite {010} faces are weakly expressed (Figure 14b). Monolayers of long-chain enantiomeric α-amino acids, $^{+}H_3NCH$-$XCOO^{-}$, $X = C_nH_{2n+1}CONH(CH_2)_4$, were predicted to form, on the water surface, 2-D crystals with their glycine moieties arranged in a manner akin to that of an *a*,*c* layer structure of α-glycine itself. These monolayers, on saturated glycine solutions, induced formation of floating pyramidal-shaped α-glycine crystals oriented with their basal (0−10) or (010) face to air depending upon the chirality of the amphiphile, shown schematically in Figure 14c,d, in Scheme 8, bottom. [73,74] These results were in accordance with a determination by GIXD of the monolayer crystal structures of the α-amino acids[22] for $n = 15, 17$ (see section IV.A.2), which proved the precise epitaxial nature of the induced nucleation.

C. Nucleation of *p*-Hydroxybenzoic Acid via *p*-Alkoxybenzoic Acid

This study provides evidence not only that a precise structural match between the Langmuir monolayer nucleator and nucleant is not required for oriented crystallization, but that in order to improve the match the monolayer may undergo a molecular rearrangement. One could say that the to-be-grown crystal takes the role of a template. Crystals of 4-hydroxybenzoic acid monohydrate, $HOC_6H_4CO_2H\cdot H_2O$, obtained from aqueous solution are composed of hydrogen-bonded layers parallel to a (401) plane (Figure 15a), which is not expressed as a crystal face. A monolayer of $C_{18}H_{37}OC_6H_4CO_2H$ was found to induce nucleation of the acid monohydrate[75] floating from its (401) face (Figure 15b). The structural match between the monolayer with bound solute, as determined by GIXD (Figure 15c), and the (401) plane of 4-hydroxybenzoic acid·H_2O is however incomplete, necessitating a partial rearrangement of the solute-bound monolayer to induce nucleation of the acid monohydrate.[76]

D. Nucleation of 3-D Crystals via Guanidium–Alkane Sulfonates

Another informative example involving a partial epitaxial match is provided by the oriented crystallization of diphenyl sulfone ($C_6H_5-SO_2-C_6H_5$) under a monolayer of 1-octadecane sulfonate spread over an aqueous solution containing a mixture of guanidine hydrochloride and bezenesulfonic acid.[77] The molecular area of the monolayer as deduced from surface pressure−area isotherms agrees with the formation of two-dimensional pseudohexagonal hydrogen-bonded mixtures of guanidinium $-C(NH_2)_3^{+}$ and $-SO_3^{-}$ ionic mixtures as shown in Figure 16a. The mixed monolayer induced nucleation of diphenyl sulfone, the decomposition product of benzenesulfonic acid. A model involving a coincident match in the lattice *d*-spacing of the nucleator and nucleant has been invoked.

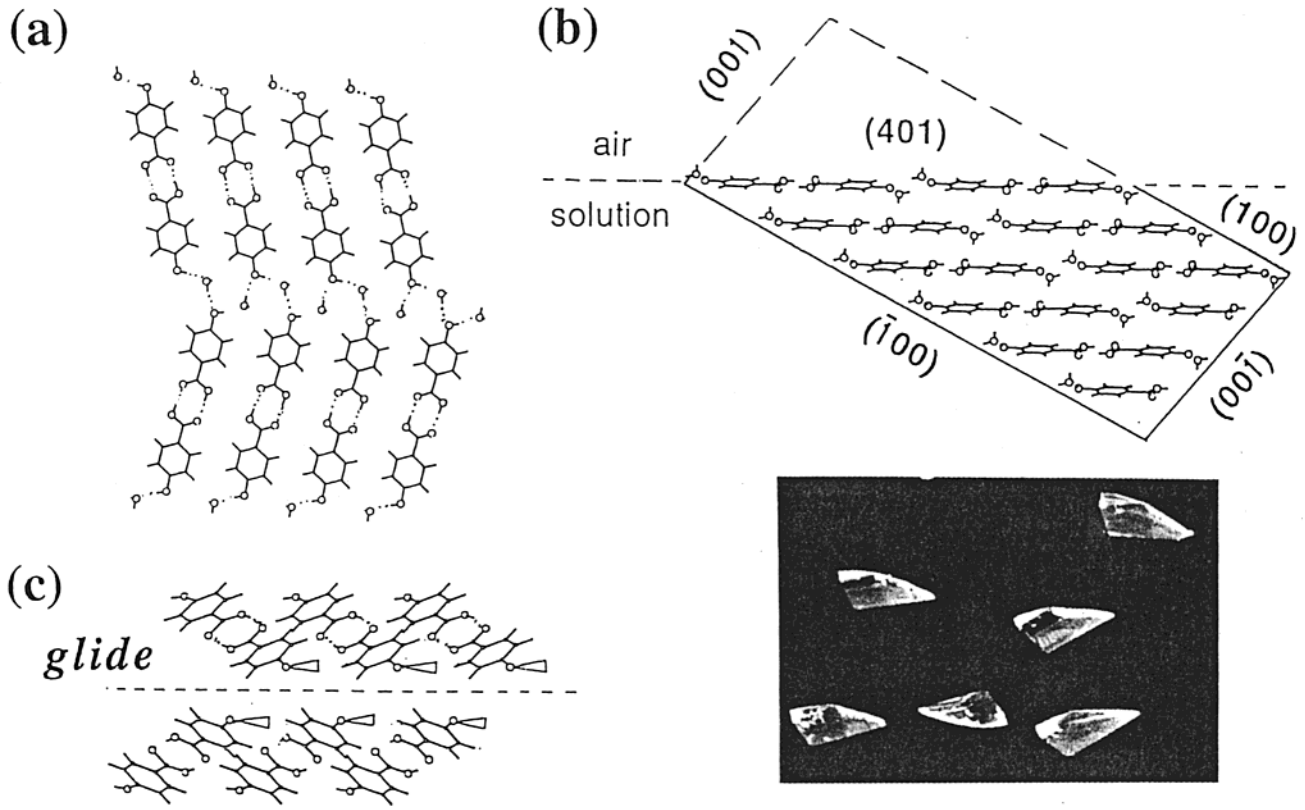

Figure 15. (a) Layer arrangement of a 4-hydroxybenzoic acid monohydrate crystal, in the (401) plane. (b) Schematic view of the orientation of a hydroxybenzoic acid crystal at the air−water interface, floating from the (401) face, when crystallized from a solution covered by a monolayer of 4-(octadecyloxy)benzoic acid or when the solution contains 4-methoxybenzoic acid as additive, as well as photographs of such crystals. (c) A pair of rows of hydrogen-bonded dimers formed between the amphiphilic molecules and the hydroxybenzoic acid solute viewed perpendicular to solution surface. According to the proposed mechanism to explain the oriented 3-D nucleation the molecules in (c) rearrange to simulate the (401) layer structure of hydroxybenzoic acid shown in (a). The wedges represent the amphiphilic chains.

E. Mixed Monolayers for Induced 3-D Crystallization

We have already described in section IV.B the principle of using mixed monolayers for estimating the limiting size of 3-D crystal nuclei epitaxially formed under a monolayer. The mixed monolayers contain segregated domains of type *A* and *B* with a common moiety structured to promote the formation of a homogeneous array of molecular moieties, common to *A* and *B*. Molecule *A*, however, contains an additional group appropriate for the induced 3-D crystallization, which would also favor their segregation into domains (Scheme 5a). As *B* we used $C_{19}H_{39}CONH_2$ and as *A* $C_{19}H_{39}CONH-(CH_2)_2-CO_2H$ for induced crystallization of bilayer compounds composed of metal salts of carboxylic acids.[78]

The crystal structure of silver propionate, $CH_3CH_2CO_2Ag$, consisting of layers in which the Ag ions are embedded within cyclic dimers of COO groups, was chosen as an appropriate system. Mixed monolayers with a molar ratio *A*:*B* down to a limiting value of 1:10 induced oriented formation at the air−solution interface of platelike silver propionate crystals. The segregated nature of the *A*+*B* domains was independently demonstrated by X-ray reflectivity, making use of cadmium ions bound to neighboring CO_2^- headgroups. The homogeneous, ordered, nature of the $C_{19}H_{39}CONH$ moiety of the mixed monolayer was proven by GIXD for a variety of *A*:*B* mixtures. A randomly distributed monolayer mixture of stearic acid *A*′ and stearyl alcohol *B*′ in a ratio as high as 1:1 did not induce silver propionate precipitation. These results show that the *A*-type domains must be of finite size to induce nucleation of the silver salt. This domain size should provide an inkling on the critical size of the 'nuclei' en route to precipitation.

F. Monolayer-Induced Nucleation of NaCl

The induced nucleation of zwitterionic glycine via an α-amino acid monolayer triggered a search for an ionic crystal whose layer structure would complement the arrangement of NH_3^+ and CO_2^- moieties of the α-amino acid monolayer (Figure 5c). The structure of NaCl at its (110) face (Figure 17a), with alternating rows of Na and Cl ions separated by 2.8 Å, appeared to fit this requirement; indeed, NaCl was nucleated from this face via amino acid monolayers.[79] The crystals of NaCl are composed of alternating {111} layers of Na^+ and Cl^- ions (Figure 17b), which suggested that a monolayer of charged long-chain carboxylic acids would induce nucleation of sodium chloride from an (111) face by electrostatic complementarity only. This prediction was experimentally demonstrated.[79] The crystals of NaCl developed (100) plates when stearylamine was used as a nucleating matrix (Figure 17c), which may be rationalized in

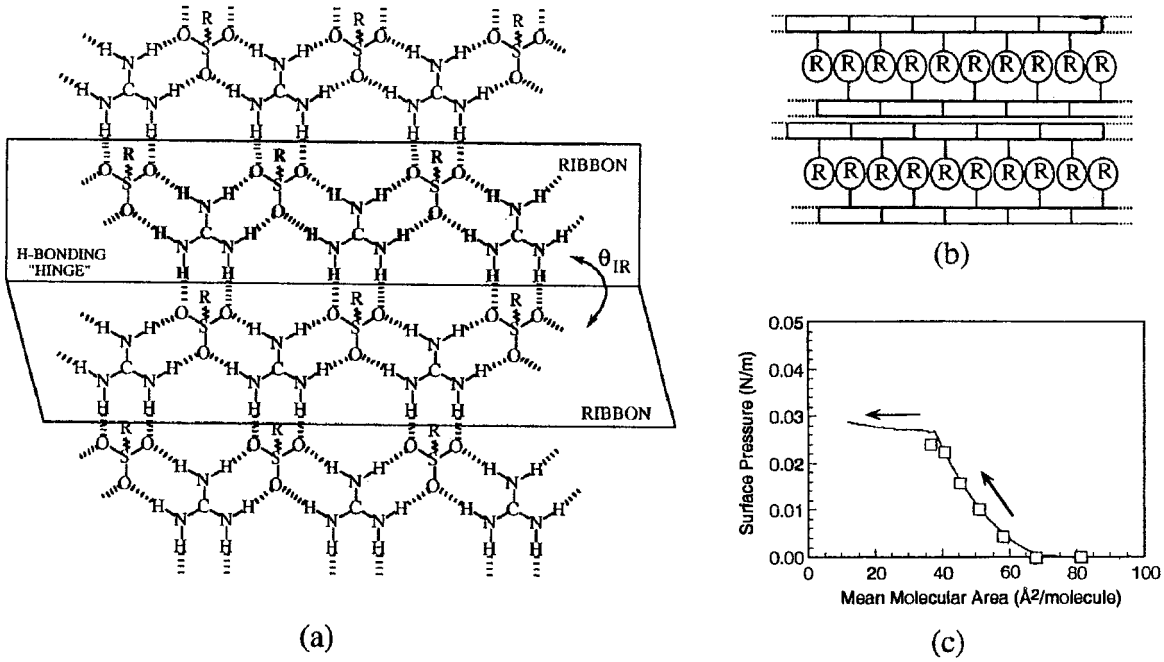

Figure 16. (a) Schematic representation of the 2-D hydrogen-bonding network present in guanidinium alkane- and arenesulfonate salts. The network can be described as 1-D ribbons, highlighted in bold, held together by hydrogen bonding between residual sulfonate oxygen lone pairs and guanidinium protons. 3-D single-crystal X-ray diffraction studies have revealed that the steric requirements of the R groups in many salts induce puckering of the sheetlike network about a "hydrogen-bonding hinge" formed by these residual hydrogen bonds. Such puckering is unnecessary in monolayers on solution. (b) Bilayer motif observed in guanidinium sulfonate salts of 3-D crystals for sterically undemanding R groups. (c) Langmuir isotherm of sodium 1-octadecanesulfonate over 0.009 M guanidinium sulfate at room temperature. The compression isotherm is indicated by the solid line (Reprinted with permission from M. Ward ref 77).

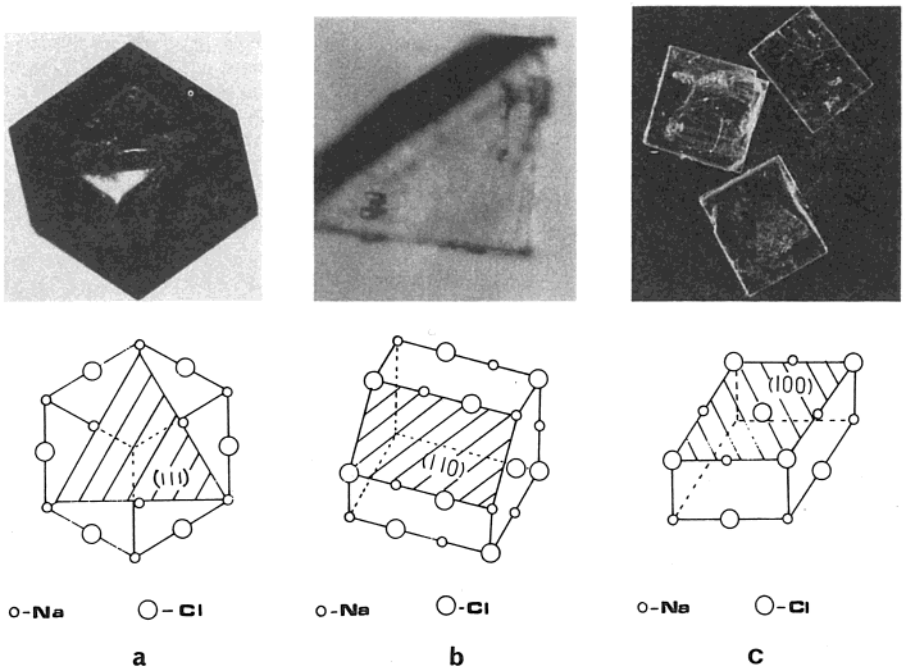

Figure 17. (a–c) Photographs of NaCl crystals nucleated via amphiphilic monolayers of α-amino acids, long-chain acids and amines respectively, and schematic views of the atom arrangement of the corresponding crystal faces.

terms of intercalating Cl^- ions between the stearylamine NH_3^+ groups.

G. Induced Nucleation of $CaCO_3$ Relating to Biomineralization

Inorganic crystals of defined phase, shape, and orientation are produced by biological systems The specific orientation of biogenic crystals with respect to an underlying organic matrix has been observed; for example, aragonite crystals in mollusc shells are aligned with respect to the β-pleated protein. Addadi, Weiner, and co-workers demonstrated (001) oriented calcite nucleation from β-pleated sheet proteins.[80]

Mann, Heywood, and co-workers made use of organized organic surfaces of amphiphilic monolayers in model studies on biomineralization.[81–84] They

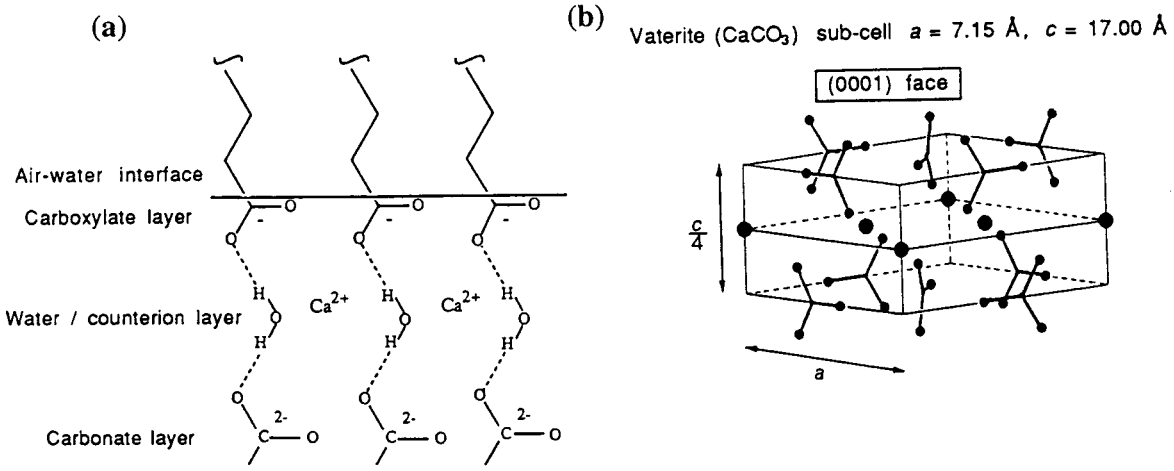

Figure 18. (left): Schematic representation of a calcium stearate monolayer. A stoichiometry of one calcium ion per two COO^- carboxylate moieties is required for charge neutrality. Interleaved water molecules in the cationic layer form hydrogen bonds with the carboxylate layer and with a carbonate layer oriented as in the (0001) layer structure of the vaterite form of $CaCO_3$ shown on the right.

examined the oriented crystallization of $CaCO_3$ under a variety of monolayers. All three polymorphs of $CaCO_3$ were obtained at the monolayer−solution interface depending upon experimental conditions. Calcite, thermodynamically the most stable form, and vaterite, the least stable, are arranged in hexagonal cells. All three crystal structures are composed of alternating *ab* layers of Ca^{2+} and CO_3^{2-} ions. In calcite and aragonite, the CO_3^{2-} plane is parallel to the *ab* plane; in vaterite, it is perpendicular to this plane. A mechanism has been suggested that water molecules, interleaved between stearic acid monolayer-bound Ca^{2+} ions, may promote nucleation of calcite and vaterite (Figure 18) via hydrogen bonding to the carbonate CO_3^{2-} ions.[5] This orienting role of water is supported by induced precipitation of vaterite via octadecylamine monolayers whose charged amino groups can form hydrogen bonds with the carbonate ions.[82,83] In all these systems there is also the possibility of a partial lattice match. The monolayers of *n*-eicosyl sulfate and *n*-eicosyl phosphate induce nucleation of calcite from the (001) face; in the presence of Mg^{2+} ions in solution, aragonite is formed from the (001) face.[85] The trigonal symmetry of the sulfate and phosphate groups coupled with an approximate structural match to the (001) arrangement of Ca^{2+} ions in the (001) planes of calcite and aragonite has been invoked to account for the induced nucleation.

Polymeric Langmuir−Schaefer films of $C_{12}H_{25}-C{=}C-C{=}C-C_8H_{16}-COOH$ were found to nucleate calcite at the (012) face.[86,87] The crystals were coaligned with respect to the polymer's conjugated backbone, explained in terms of a stereochemical match between tilted carboxylates of the film and the carbonates of the crystal. There is the alternative explanation, already invoked above, that water molecules intercalated between the Ca^{2+} ions of the top layer help induce the oriented nucleation of calcium carbonate crystals.

H. Formation of Semiconductor Nanoparticles

Compressed monolayers of arachidic acid have been employed to direct the oriented growth of semiconductor crystals of PbS,[88,89] PbSe,[90] and CdS.[91] For example, induced crystallization of PbS was achieved by spreading the surfactant on a subphase of $Pb(NO_3)_2$ followed by injection of H_2S into the subphase. Equilateral triangular nanocrystals varying in size from 30 to 60 nm and oriented vis-à-vis to each other were nucleated from a {111} face (Figure 19). PbS has a cubic NaCl-type structure. The structure is composed of alternating layers of Pb and S atoms parallel to the {111} plane in a hexagonal sublattice with a repeat area of 15.3 $Å^2$, which is decidedly less than the unit cell area per molecule of lead arachidate of ≈18 $Å^2$. Nevertheless, the oriented alignment of neighboring triangular crystals of PbS indicates induced nucleation via a partial match between the hexagonal subcell of PbS in its {111} plane and a subcell of the monolayer of Pb arachidate.

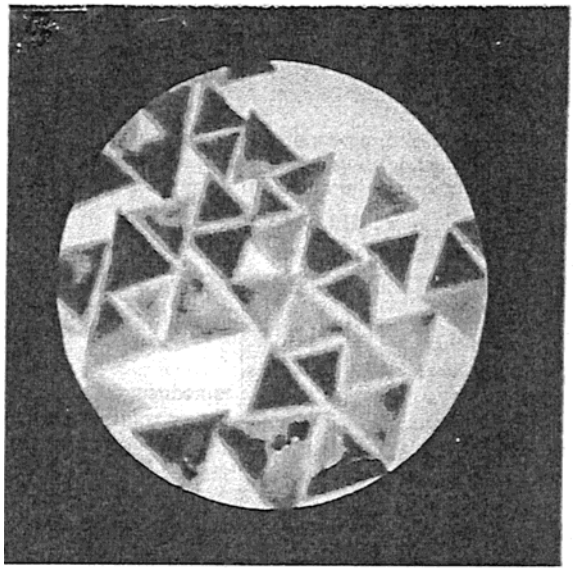

Figure 19. Transmission electron micrograph of PbS crystals formed by infusion of H_2S into an aqueous subphase of $Pb(NO_3)_2$ under an arachidic acid monolayer. The diameter of the aperture is about 0.4μm. Reprinted with permission from J. Fendler, ref. 88. Copyright 1992 American Chemical Society.

I. Evidence for Ordering of Water-Soluble Amphiphiles at Interfaces

The degree of coverage on the water surface of water-soluble amphiphiles and their orientation vis-à-vis the water surface can be evaluated by methods such as surface tension measurements, second harmonic generation spectroscopy, and X-ray and neutron reflectivity. These methods, however, provide no direct evidence of 2-D molecular ordering. Oriented nucleation of crystals at the air−solution interface via a monolayer of water-soluble amphiphiles can provide indirect evidence of 2-D ordering of the amphiphiles, in particular if a long-chain water-insoluble counterpart behaves similarly. Evidence in favor of 2-D ordering of the *S* and *R* enantiomers of the naturally occurring hydrophobic α-amino acids at the air−aqueous solution interface has been gleaned by induced crystallization.[92] The addition of such amino acids of a single handedness to glycine solution yielded floating pyramidal-shaped α-glycine crystals oriented with their basal (010) or (0−10) face to air depending upon the chirality, *R* or *S*, of the additive. This result mirrors those obtained with water-insoluble long-chain α-amino acids (see Scheme 8 and Figure 14c) whose crystalline monolayer structures were determined by GIXD (see section IV.A). Thus, we may deduce that naturally occurring hydrophobic α-amino acids form ordered 2-D domains at the solution surface, but which were not observed by GIXD, perhaps because of too small a domain size and insufficient amount of crystalline material.[22]

The second example centers on the induced crystallization of *p*-hydroxybenzoic acid monohydrate. We described the crystallization of this molecule induced via ordered monolayers of *p*-alkoxybenzoic acid (section VI.C). The added presence of *p*-methoxybenzoic acid, $H_3COC_6H_4COOH$, in an aqueous solution of *p*-hydroxybenzoic acid also induces crystal formation of the latter floating from its (401) face (Figure 15b), which suggests that the additive accumulates at the solution surface, facilitating layer-type aggregation with hydroxybenzoic acid.[75]

Evidence, albeit indirect, of 2-D ordering of water-soluble hydrophobic molecules has also been obtained by topochemically controlled photoreactions. We have already described that crystalline monolayers on water of the acid p-$C_{18}H_{37}OC_6H_4CH{=}CHX$, X = COOH, photodimerize in accordance with a 4 Å separation between the C=C bonds (Figure 3a) but that crystalline monolayers of the amide, X = $CONH_2$, undergo a *trans*−*cis* isomerization because the intermolecular C=C distance of 5 Å is too long for photodimerization (Figure 3b). Thus a surface-active, yet water-soluble, *trans*-cinnamic acid, $RC_6H_6CH{=}CHCOOH$, where R is a hydrophobic group, stacked parallel along a 4 Å 'axis' on the solution surface, should yield mirror dimers on UV irradiation, but the corresponding amide should only isomerize. This hypothesis was tested with 4-methoxy-*trans*-cinnamic acid and the corresponding cinnamamide (R = $-OCH_3$). The photoproducts formed in bulk aqueous solution and at the solution surface were experimentally differentiated. Only the latter yielded the mirror dimer for the acid; the amide underwent *trans*−*cis* isomerization.[93]

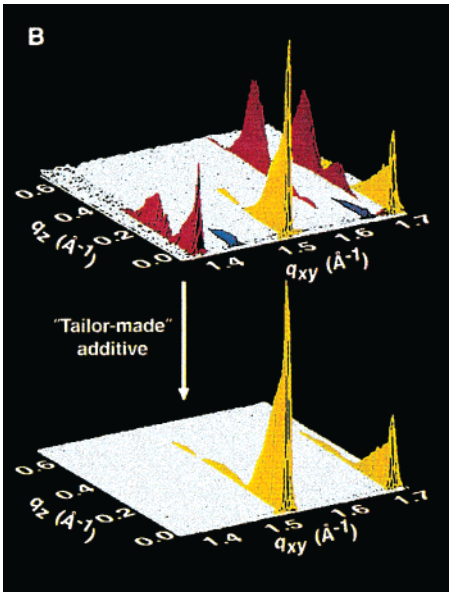

Figure 20. Two-dimensional intensity plots $I(q_{xy},q_z)$ of the GIXD pattern of arachidamide on 70% formamide-water subphase. (Top) GIXD patterns (red, yellow) of the crystalline dimorphs of pure arachidamide; (Bottom) GIXD pattern of only one dimorph of arachidamide appears when the spreading solution contains 5% *N*-methylarachidamide.

VII. Multilayer Crystallites on Liquid Surfaces

Amphiphilic molecules almost invariably form monolayers on the water surface. We shall describe results showing that certain amphiphiles spontaneously form multilayers on liquid formamide. This result was interpreted in terms of partial dissolution of the amphiphile in the subphase. Molecules containing hydrogen-bonding groups at both ends of the chain, i.e., bolaform amphiphiles, as well as pure long-chain alkanes were found to form, on the water surface, multilayer crystallites whose packing arrangements may be determined to almost atomic resolution. The multilayer systems of the various types of molecules exhibited polymorphic behavior whose interlayer growth as well as polymorphism could be controlled with the use of tailor-made inhibitors. These results have bearing on the control of polymorphic behavior of 3-D crystals with the use of tailor-made auxiliary molecules.[94]

A. Multilayer Formation of Amphiphilic Molecules

Recent GIXD studies have demonstrated that certain amphiphiles, when spread on liquid surfaces, spontaneously form not monolayers but rather multilayer crystallites. For example, arachidamide, $C_{19}H_{39}CONH_2$, when spread on water aggregates into a crystalline monolayer. On the other hand, when spread on liquid formamide, the molecules form first a crystalline monolayer, later developing into dimorphic trilayers,[55,95] exhibiting different chain tilts from the normal to the liquid surface. A formamide−water subphase yielded a mixture composed of the tilted trilayer phase plus the untilted phase in monolayer form, according to the GIXD data (Figure 20, top).

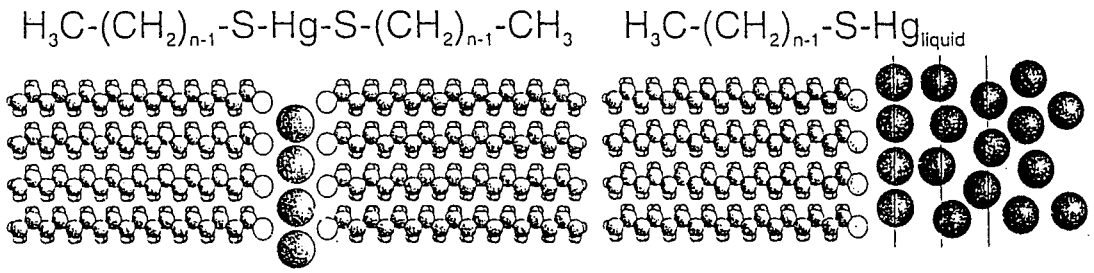

Figure 21. Model structure of the trilayer $C_{18}H_{37}-Hg-C_{18}H_{37}\cdots C_{18}H_{37}-S-Hg$ on liquid mercury.

Addition of 5−10% of additive $C_{19}H_{39}CONHCH_3$, where the role of the $N-CH_3$ group is to interfere with regular formation of interlayer growth from the subphase, inhibited the trilayer formation, yielding monolayer only of the untilted arrangement, according to the GIXD pattern (Figure 20, bottom). These results were interpreted in terms of multilayer growth at the side of the film in contact with the liquid formamide for systems where the amphiphile is partially soluble in the solvent,[8,95] which is in agreement with trilayer formation on water of enantiomerically pure $C_{11}H_{23}CONH(CH_2)_4CH(NH_3^+)COO^-$, whose longer-chain analogues form monolayers[22] (see Figure 5).

In all these structures only trilayers are formed, presumably because in this way the uppermost molecule exposes methyl groups; a film with an even number of layers would expose hydrophilic groups.

B. Alkanethiol Multilayers on Liquid Mercury

As already discussed (section V.B), alkanethiol $C_nH_{2n+1}SH$ (n = 16, 18, 22, 30) films on liquid mercury were found by Magnussen et al.[60] to be densely packed but with no long-range order. At high thiol coverages, alkanethiol trilayers were formed, comprised of a bilayer, containing an intercalated Hg layer, on top of the alkanethiol monolayer (Figure 21) according to X-ray reflectivity.[96] GIXD measurements showed the film to be crystalline, but whether only the top bilayer is ordered has yet to be established.[96] The unit cell of the crystalline bilayer, of dimensions a,b,γ, = 4.3 Å, 4.7 Å, 109°, contains only one Hg atom bound to two alkanethiol molecules from opposite sides (Figure 21). The density of this Hg layer is about one-half that of the liquid surface Hg layer. The unit cell is similar in dimension to the representative subcell (4.3 Å, 4.7 Å, 111°) of 3-D crystals of a class of hydrocarbons whose chain axes are perpendicular to the *ab* plane.[97] With this information, the azimuthal orientation of the alkanethiol chain vis-à-vis the *ab* cell axes can be fixed and also the relative positions of the alkanethiol and the Hg atom, given the geometry of the S−Hg bond.

C. Multilayer Formation of Bolaform Amphiphiles on Water

The diol $HO-(CH_2)_{22}-OH$ on water, studied in relation to ice-nucleating activity, exhibits a limiting area per molecule of less than 10 Å^2 along its surface pressure−area isotherm, triggered the following recognition: A bolaform amphiphile, such as $X-(CH_2)_n-X$, where X is a group that can make interlayer hydrogen bonds, such as OH or COOH, may display a tendency for crystalline multilayer formation on the aqueous surface. This prediction was demonstrated with the GIXD measurements of $HO(CH_2)_{22}OH$ on water, which yielded a bilayer packing arrangement.[98] The morphology was imaged by cryo-transmission electron microscopy on vitreous ice. The multilayer growth of $HO(CH_2)_{22}OH$ could be inhibited upon addition of 10% of long-chain monoalcohols as monitored by atomic force microscopy.[99] The diacid $HO_2C-(CH_2)_{22}-CO_2H$ on pure water forms dimorphic multilayers,[100] with somewhat different chain tilt angles from the normal to the water surface for the dominant and minor dimorphs.

D. *n*-Alkane and Oligothiophene Multilayers on Water

The formation of crystalline multilayers at zero surface pressure on water for the α,ω-alkane diols suggested that the alkanes C_nH_{2n+2}, $20 < n < 30$, with a similar surface pressure−area isotherm behavior, also self-aggregate into multilayers on water. This prediction proved to be correct according to GIXD data.[50] For $n > 31$, monolayers were formed, and as the chain length decreased from $C_{29}H_{61}$ to $C_{23}H_{48}$, the number of layers increased from 2 to about 20. The molecular chains in these crystals are aligned normal to the layer plane adopting the herringbone packing but for the hydrocarbon chains of $C_{24}H_{50}$, which are highly tilted and related by translation only. For some of the long-chain alkanes, such as n = 34 and 50, the Bragg rods assume a skewed shape (see Figure 2b) interpreted in terms of bent crystalline films, perhaps assuming a concave-like shape.

Multilayer growth of the alkanes $C_{23}H_{48}$ and $C_{24}H_{50}$ was inhibited on addition of 5−10% of the respective alcohols $C_{27}H_{55}OH$ and $C_{28}H_{57}OH$. Not only was film thickness reduced from 20 layers to a bilayer, but a change was induced in the packing arrangement of $C_{24}H_{50}$ from triclinic $P\bar{1}$ to orthorhombic $Pbc2_1$ according to their GIXD patterns (Figure 22). This result was explained by energy computations: The crystal lattice energy of the $P1$ form of $C_{24}H_{50}$ is more stable by 0.5 kcal/mol. However, the situation is reversed for their layer energies, with a difference of 0.8 kcal/mol in favor of the orthorhombic form, whose preferred precipitation may be understood if the additive induces layer by layer growth from inception; otherwise crystallization of the triclinic form should be preferred.

Aromatic hydrocarbons such as oligothiophenes $H-(C_4H_2S)_n-H$, n = 4−6) were also found to self-

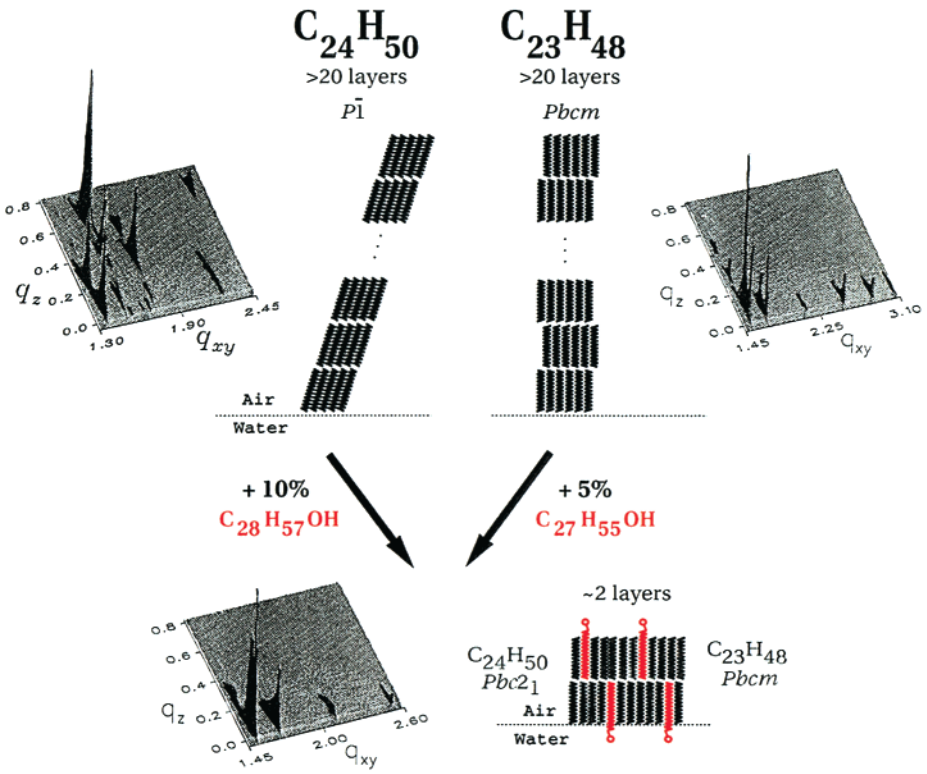

Figure 22. (Top): Schematic representation of the multilayer crystalline packing arrangements on water of the alkanes $C_{24}H_{50}$ of triclinic symmetry *P*-1 and $C_{23}H_{48}$ of orthorhombic symmetry *Pbcm*, together with the two-dimensional intensity distributions $I(q_{xy},q_z)$ of their GIXD patterns. (Bottom): Bilayers of orthorhombic symmetry were formed on addition of small amounts of alcohol additives, according to the GIXD patterns for $C_{24}H_{50}$ + additive and for $C_{23}H_{48}$ + additive which were essentially the same.

organize on the water surface,[101] yielding multilayers from the shorter homologues $n = 4$, 5 and monolayer from $n = 6$.

The lack of hydrophilic headgroups suggests that the alkanes and oligothiophenes grow layer by layer above the water surface, perhaps from liquid drops.

E. Surface Layer Freezing in Chain Molecules on Bulk Melt

In general, the solid surfaces of 3-D crystals melt at a temperature lower than that of the bulk[102,103] since the molecules are less confined at the surface and therefore have a higher entropy than that of the bulk. The opposite effect, called surface freezing, when an ordered surface layer coexists with its own bulk melt has been recently discovered in crystals containing aliphatic chains.[104−108] These results are in a sense akin to smectic layering at the free surface of a nematic or isotropic bulk.[109−111]

The long-chain alkanes C_nH_{2n+2}, $n \geq 16$, form ordered monolayers at a temperature T_s a few degrees above the bulk freezing temperature T_b and may be classified into three groups according to their *n* values as exemplified in Figure 23, which shows the GIXD patterns and schematic packing arrangements for $n = 20$, 36, and 44. For $n \leq 30$, the molecules appear in a hexagonal unit cell with an area $A = 19.7$ Å^2, in which the chains are aligned normal to the layer plane (Figure 23a,d). For $30 < n < 44$ (Figure 23b,e), the molecules also appear in a hexagonal cell whose area *A* increases with *n* as a result of a larger chain tilt along the direction of

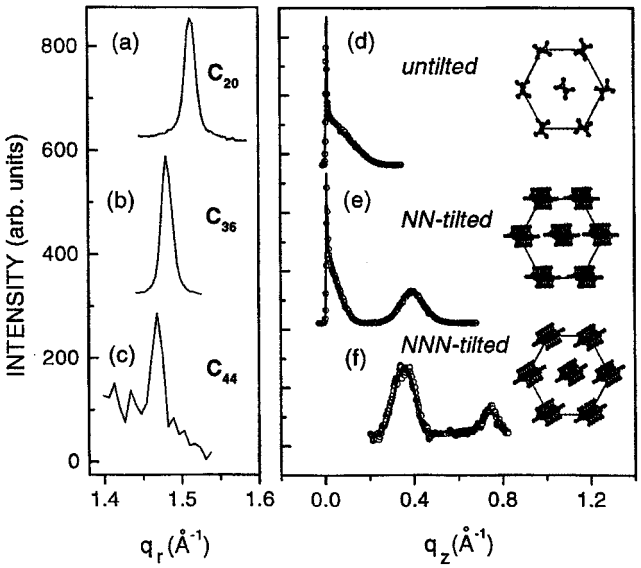

Figure 23. Surface layer freezing of three alkanes C_nH_{2n+2}, $n = 20$, 36, 44. (a−c) Bragg peaks $I(q_{xy})$., where $q_r = q_{xy}$. (d−f) Bragg rods$I(q_z)$ and corresponding tilt directions of the chains. The terms NN and NNN indicate that the chains are tilted in the direction of nearest-neighbor and next-nearest-neighbor respectively (Reprinted with permission from M. Deutsch ref 108).

nearest neighbors, with the constraint that the molecular cross-sectional area A_x remains at 19.7 Å^2. For $n \geq 44$ (Figure 23c,f), the cell is hexagonal in which the chains are tilted in a direction between nearest neighbors, where the molecular area A_x is reduced to 18.7 Å^2.

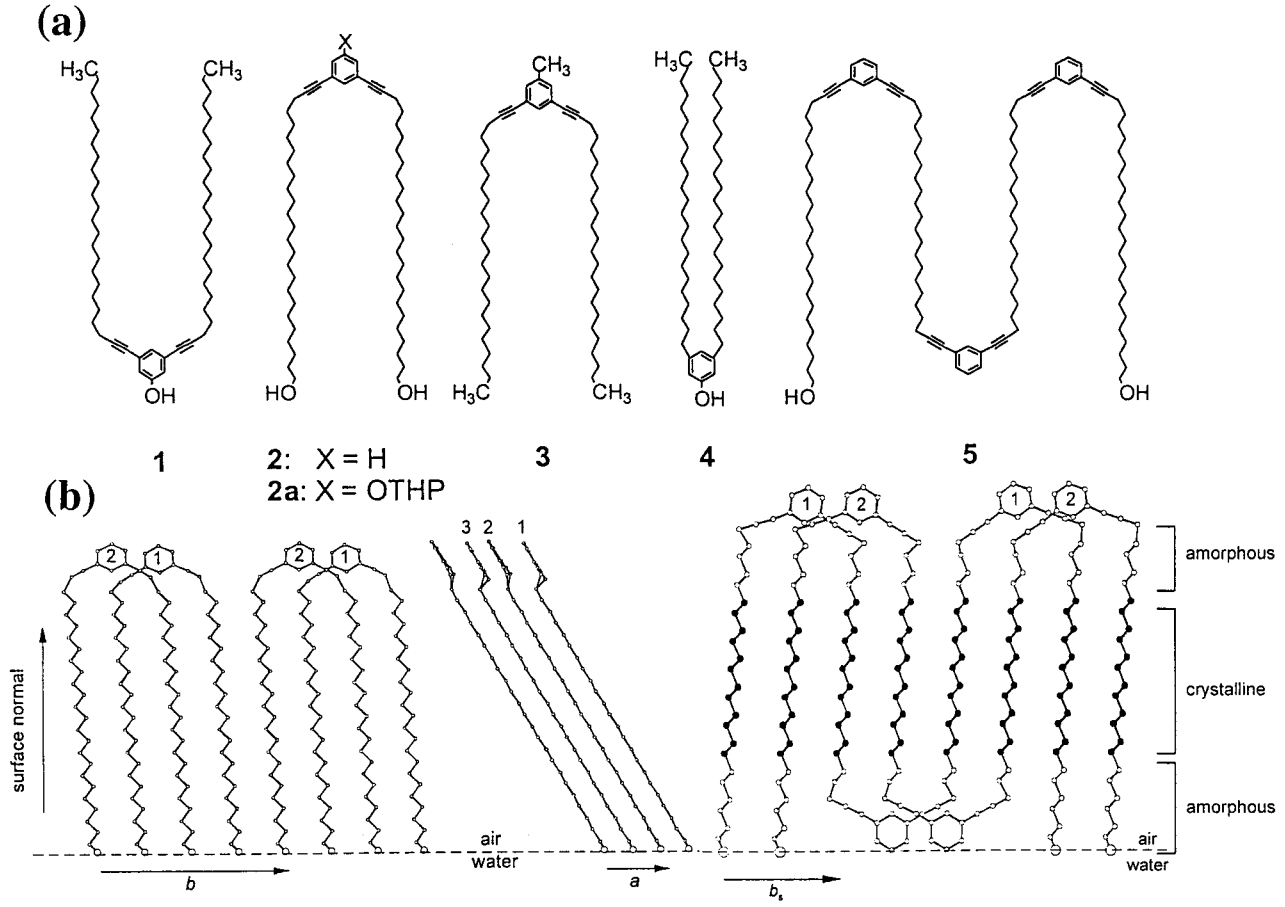

Figure 24. (a) U-, inverted U-, and M-shaped chain like molecules **1**−**5**, whose crystalline monolayer structures formed at the air−water interface had been characterized by GIXD. (b) The packing arrangements of **2** (left, center) and of **5** (right) each displaying folding of chains evenly spaced along the *b* axis.

The surface freezing layers of the alkanes $16 \leq n < 44$ form a rotator phase[107] which is characterized by the existence of long-range order in molecular position but not in rotation angle about the molecular axis. For $n \geq 44$, the surface layer was described as a true monolayer crystal which is in keeping with the molecular cross-sectional area of 18.7 Å^2. For $n > 30$, the alkane chains are tilted and therefore the packing symmetry is not hexagonal since the distances between any chain and its six nearest neighbors are not all the same. We note that the unit cell dimensions are all hexagonal irrespective of the value of *n*. Whether this behavior is imposed upon by the underlying liquid phase is a moot point.

The surface freezing behavior of the long-chain alcohols $C_nH_{2n+2}OH$, $16 \leq n \leq 28$, were also examined.[107,112] Surface freezing was found to occur only for *n* even. X-ray reflectivity measurements indicated that a surface bilayer is formed.

F. Ordered Polymer Films at the Air–Water Interface

The observed monolayer crystalline formation of the alkane $C_{50}H_{102}$ prompted the engineering of a crystalline monolayer composed of undulating oligomer chains at the air−water interface. GIXD experiments have demonstrated the feasibility of such an approach with the monolayer crystalline formation of U-, inverted U-, and M-shaped chainlike molecules (Figure 24a) that appeared in the arrangements shown in Figure 24b.[113,114]

In a different set of experiments a short-chain oligomer and the polymer of Nylon-6,6 on water were found to form hydrogen-bonded arrangements akin to that of the macroscopic 3-D crystal of polymeric Nylon-6,6 but where the oligomer assembles into a monolayer with the chain axis somewhat tilted from the surface normal and the polymer forms a multilayer whose chain axes lie parallel to the water surface.[115]

VIII. Supramolecular Architectures Prepared in Situ at the Air–Solution Interface

The self-assembly at the air−water interface of simple chainlike molecules into thin crystalline films has been extended to the generation of crystalline films composed of supramolecular architectures prepared in situ at the air−solution interface. One approach involves the use of two complementary molecules, one water-insoluble with a long chain and the other water-soluble, extracted from the solution subphase. Different architectures may be prepared in this way, for example, monolayers by complementary hydrogen bonding or interdigitated films engineered via acid−base interactions between long-chain water-insoluble and water-soluble organic molecules. Another procedure involves complexation at the air−solution interface between water-insoluble organic

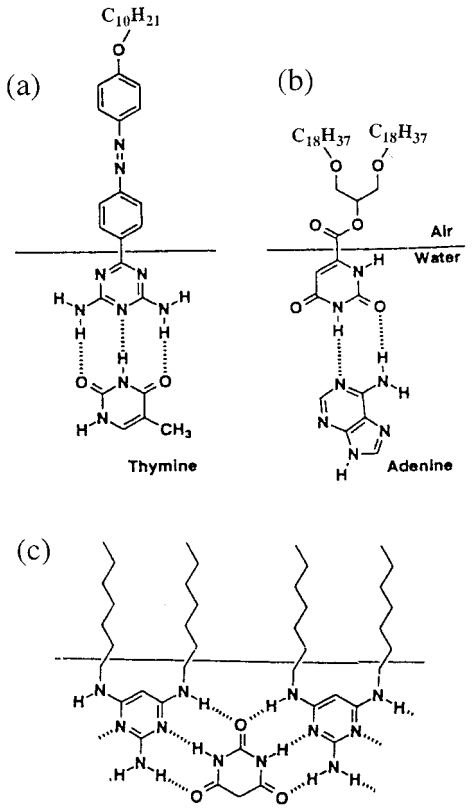

Figure 25. Hydrogen-bond pairing at the air−water interface of: (a,b) nucleic acids thymine[118] and adenine[119] to receptor monolayers, and (c) barbituric acid to a melamine type monolayer. [123,124]

molecules and metal ions from the solution. This approach has yielded multilayers composed of simple structures such as organic long-chain dicarboxylic acids and metal ions or supramolecular multicomponent systems. Finally, organically functionalized metal nanocrystals have been found to self-assemble into monolayer superlattices on the water surface. Here we describe the design and characterization of these systems.

A. Hydrogen-Bonded Host–Guest Monolayer Systems

Hydrogen bonding plays a decisive role in the assembly of nucleic acid polymers via complementary base pairing. Such molecular interactions were mimicked at the air−water interface by Kitano and Ringsdorf,[116] who studied $\pi-A$ isotherm behavior of an adenine-functionalized amphiphile on aqueous nucleosides from which they proposed an adenine−thymine-type pair at the interface. A systematic study of complementary hydrogen bonding in the formation of monolayers at the air−aqueous solution interface, making use of nucleic acid base pairs and other biological hydrogen-bonding moieties, was initiated by Kunitake and co-workers.[117] They provided more direct evidence in favor of the proposed models of guest binding by transfer of the films to solid surface and characterization by photoelectron spectroscopy (XPS) and FT-IR spectroscopy, two examples are which are given in Figure 25a,b.[118,119]

Complementary hydrogen bonding, as between melamine and cyanuric acid used in the construction of supramolecular motifs in organic media and in 3-D crystals,[120,121] has also been employed in the construction of monolayers at the air−aqueous solution interface. This approach is exemplified in the binding of triaminopyrimidine to barbituric acid amphiphiles[122] and the formation of an interfacial network of barbituric acid and melamine-type amphiphiles[123,124] shown in Figure 25c. The crystallinity of all these monolayers has not yet been examined by diffraction methods.

B. Interdigitated Crystalline Films via Monolayer Compression

Bilayers composed of interdigitated molecules *A* and *B* with acid−base complementarity can be formed at the air−solution interface, where *A* has a long hydrocarbon chain and *B* does not, as depicted in Scheme 4 (bottom of left and right columns).

Use was made of mandelic acid, $C_6H_5CHOHCO_2H$ (MA), and phenylethylamine, $C_6H_5CHCH_3NH_2$ (PEA), as chiral functional groups for interdigitation, where either the acid (MA) or the amine (PEA) is modified by attaching the chain $C_{15}H_{31}-$ in the *para* position. A film of $C_{15}H_{31}-C_6H_4CHOHCO_2H$ of *R* configuration, labeled *R*-($C_{15}H_{31}$−MA), over a solution of *S′*-(PEA) did not diffract at any point along the compression isotherm. In contrast, replacing the solution by *R′*-(PEA) yielded a GIXD pattern after high compression. The film structure (Figure 26a) is an interdigitated crystalline trilayer whose alkyl chains exposed to air are disordered.[125] Indeed, the system will only pack well in a crystalline bilayer containing interdigitated chains. The effect of chirality may be explained in terms of the 3-D crystal structures of MA and PEA;[126,127] only the chiral groups MA with the same handedness, e.g., *R*-(MA) and *R*-(PEA), are compatible with formation of the interdigitated bilayer but not the groups PEA and MA of opposite handedness. In an analogous manner, crystalline interdigitated films composed of up to seven layers have been formed from the binary acid−base system composed of a long-chain benzoic acid and a water-soluble amidinium molecule (Figure 26b).[128]

An interdigitated molecular system has in all likelihood been obtained upon deposition of 1-sodium octadecane sulfonate amphiphile over an aqueous subphase containing guanidinium sulfonate, studied by Ward and co-workers.[129,130] This acid−base system yielded a surface pressure−area isotherm (Figure 16c) compatible with intercalation of the guanidinium $C(NH_2)_3^+$ cations between the octadecanesulfonate $(C_{18}H_{37}SO_3)^-$ anions into a 2-D hydrogen-bonded network (Figure 16a).[77] The shape of the isotherm after monolayer collapse (Figure 16c) is in keeping with interdigitation, as observed in the 3-D crystal structures of guanidinium arenesulfonate (Figure 16b).

It appears that the basic requirement for interdigitation is the spontaneous formation first of the mixed monolayer comprising the two complementary acid−base components in proper registry, despite the loss in effective chain packing as shown in Scheme 4 (top left and right columns). A general model for the

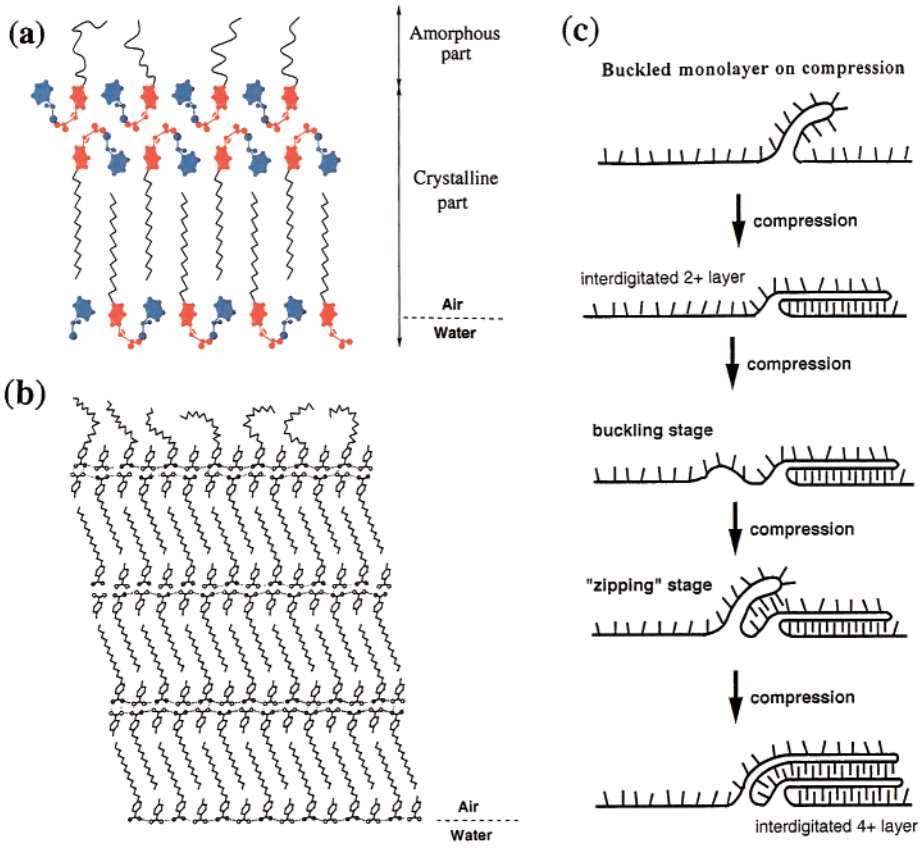

Figure 26. Interdigitated packing arrangements at the air−solution interface. (a) Trilayer of long-chain *R*-mandelic acid and *R′*-phenylethylamine. (b) Seven layers of long-chain benzoic acid and amidinium. (c) A general model of molecular reorganization leading to an interdigitated crystalline multilayer upon compression of an amorphous monolayer composed of the water-insoluble and water-soluble species as in Scheme 4 (top left and right).

process of molecular reorganization as function of film compression, for the formation of an interdigitated multilayer system is depicted in Figure 26c.[125,128] The figure incorporates a basic premise that the monolayer film becomes buckled upon compression with a tendency toward corrugation. Such a regular distortion of a monolayer has been reported by Daillant and co-workers in a GIXD study on a film of cadmium arachidate on solution (Figure 2a), yielding an average corrugation wavelength of 20 nm.[32]

C. Metal Complex Films

The formation of the interdigitated two-component systems discussed above led to the idea that water-insoluble and water-soluble components can interact at the air−solution interface to spontaneously form oriented crystalline architectures. The long-chain α,ω-dicarboxylic acids, when deposited on water, form crystallites in which the molecules are aligned with their long axes somewhat off the normal to the water surface (see section VII.C). A different organization of these molecules was determined by GIXD (Figure 27a,b) on aqueous subphases containing divalent Cd^{2+} and Pb^{2+} ions.[100] The diacids react with the ions to form the corresponding salt, which self-assemble with their hydrocarbon chains *parallel* to the water surface, forming crystalline films about 50 Å thick (Figure 27c). Such crystalline multilayers on transfer to glass followed by reaction with H_2S yield quantum dots with a diameter ranging from 2 to 4 nm for both the cadmium and lead salts.[131]

More complex crystalline film architectures could be self-assembled at the air−solution interface. Recently, spontaneously assembled, oriented crystalline films composed of *n*x*n* grids $n = 2$ and 3 of silver ions bound to ligand molecules were prepared in situ at the air−aqueous solution interface by interaction of the free ligand molecules spread on the aqueous solution with the silver ions, as established by their GIXD patterns (Figure 28a,c), complemented by X-ray reflectivity, scanning force microscopy, and X-ray photoelectron spectroscopy.[132,133] The packing arrangements of the 2 × 2 silver grid that forms a monolayer and of the 3 × 3 silver grid that self-assembles into a bilayer are presented in Figure 28b,d.

D. Superlattices of Organically Capped Metal Nanocrystal Monolayers

Rapid progress has been made over the past several years for the preparation of organically soluble semiconductor and metal nanocrystals showing a narrow size distribution.[134−136] Langmuir−Blodgett procedures have been applied for the preparation of ordered close-packed 2-D arrays of trioctylphosphine oxide-capped CdSe nanocrystals with narrow size distributions upon compression on water.[137] Organically passivated particles of silver and gold can also form ordered, close-packed, 2-D arrays

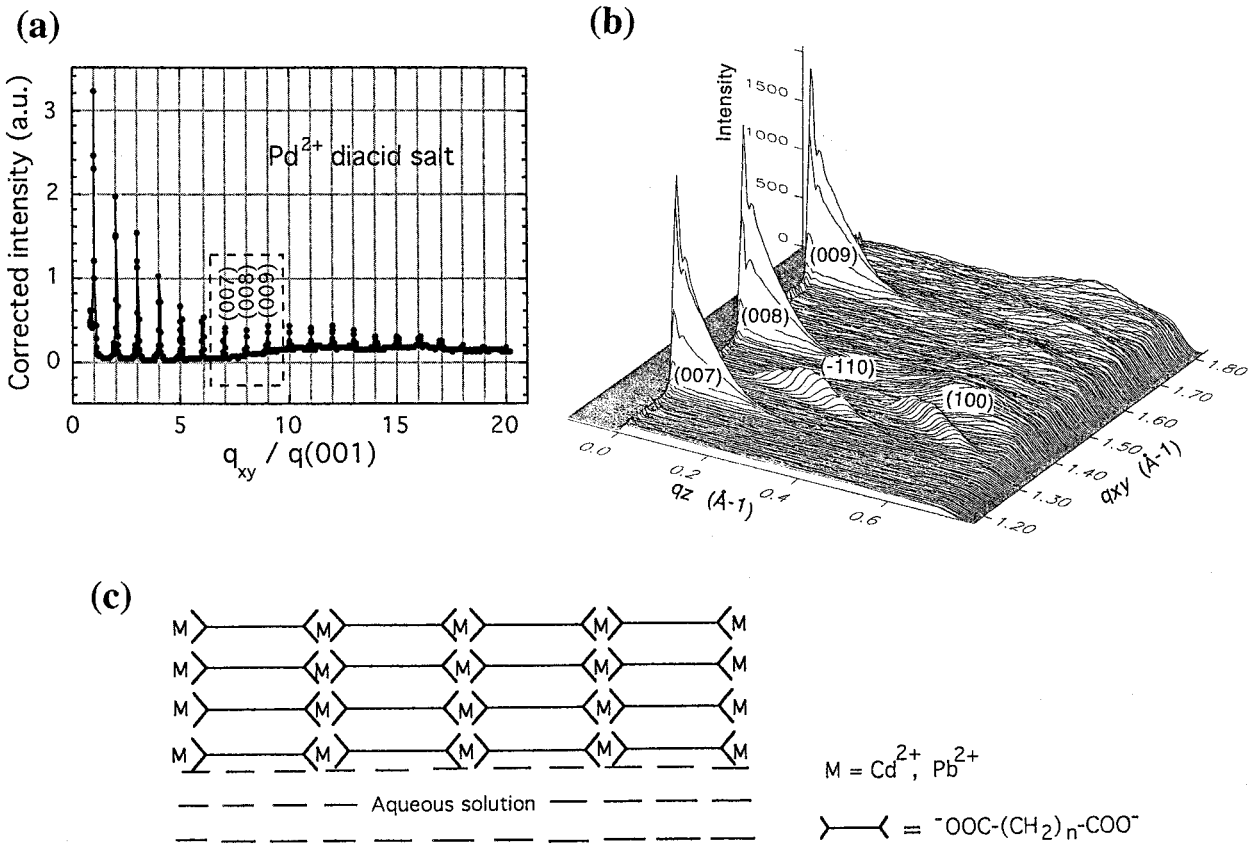

Figure 27. (a) GIXD pattern of HOOC−$(CH_2)_{22}$−COOH on a lead chloride aqueous solution. (b) The Bragg rods of three of the (00*l*) refections, and of the (−110) and (100) reflections. (c) Schematic view of the multilayer crystal of the lead diacid salt on solution.

upon compression on water, depending upon the chain length of the capping agent and the radius of the metal sphere, as shown, for example, in Figure 29.[138]

E. Superlattices of Short-Chain Peptide Monolayers on Water

Hydrogen-bond-mediated assembly of peptides provides a powerful tool for the generation of ordered supramolecular architectures.[139−161] Spectroscopic studies on Langmuir films of amphiphilic peptides with alternating hydrophilic and hydrophobic side groups have provided evidence of β-sheet formation.[142,143] Nonetheless, spectroscopic measurements do not provide information on long-range order. In particular, the flexibility of the peptide backbone and, paradoxically, the repetitive nature of the amino acid sequence may induce one-dimensional (1-D) long-range order only along the peptide hydrogen-bond direction (Figure 30a, inset). To induce the crystalline order in 2-D (Figure 30a), a family of peptides represented by the sequence X−Y−$(Z-Y)_n$−X were studied;[144] the N- and C-terminal residues of the peptides (X) bear charged ammonium and carboxylate groups, respectively, and Y and Z are alternating hydrophilic and hydrophobic amino acids. In a monolayer assembly of β-sheet peptides, the chain termini govern intermolecular interactions between juxtaposed β-sheet ribbons (along *b*) whereas hydrogen bonds along the chain dominate the intermolecular interactions in the direction normal to the peptide chain (along *a*).

In the peptide Pro-Glu-$(Phe-Glu)_4$−Pro, Pro = proline, Glu = glutamic acid, and Phe = phenylalanine, the rigidity of the Pro side chain has been anticipated to induce the juxtaposition of β-sheet ribbons. Glu in its protonated state was selected as the hydrophilic amino acid (Y), as it may form a hydrogen-bond network between carboxyl groups bridging adjacent strands. Phe has been chosen as the hydrophobic amino acid (Z) since it can span the spacing between neighboring strands via favorable phenyl ring contacts.[145,146]

The Pro-Glu-$(Phe-Glu)_4$−Pro films on pure water self-assembles into 2-D crystalline β-sheet monolayers, according to GIXD measurements. The GIXD pattern (Figure 30b) could be indexed in accordance with the structural model depicted in Figure 30a, yielding a spacing of 4.7 Å, characteristic of pleated peptide strands interlinked by N−H···O=C hydrogen bonds, and a 37.4 Å spacing, attributed to the repeat distance defined by juxtaposition of neighboring hydrogen-bonded ribbons. The crystalline coherence length *L*, a measure of the extent of lateral molecular order, is approximately 400 Å along both the 4.7 and 37.4 Å spacing directions.

Principal molecular packing features of the monolayer of Pro-Glu-$(Phe-Glu)_4$−Pro could be extracted by X-ray structure factor calculations of molecular models that were refined to provide a good fit to the observed GIXD pattern. The GIXD data has been matched by a model that involves superposition of two structures (see Figure 30c) exhibiting Phe groups oriented generally in opposite directions relative to

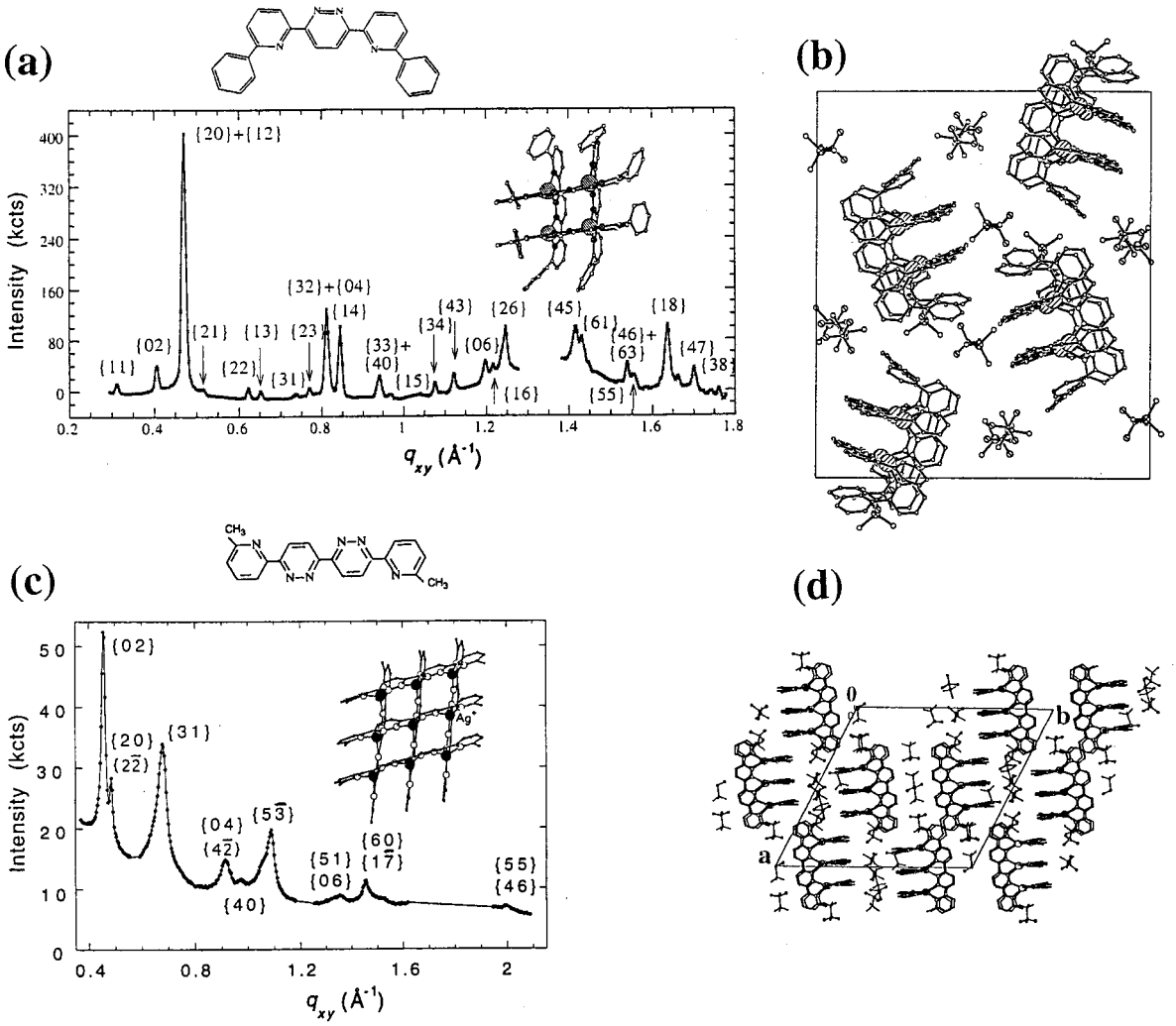

Figure 28. GIXD patterns and structures of in-situ self-assembled crystalline films composed of *n*x*n* silver grids bound to ligand molecules and derived crystalline structures. (a,b) The 2 × 2 silver grid that self-assembles into a crystalline monolayer. (c,d) The 3 × 3 silver grid that self-assembles into a crystalline monolayer.

the *b* axis. The large intramolecular spacing of 6.9 Å between adjacent amino acids of the same type (see Figure 30a) gives rise to relatively high librational motions of the side chains and thus to the possibility of various amino acid side-chain conformations.

IX. Ordered Assemblies of Membrane-Active Compounds on the Water Surface

Natural biomembranes are systems of a variety of compounds such as phospholipids, cholesterol, proteins, etc., held together by noncovalent interactions. Structural studies of model membrane films may provide knowledge on the tendency of the different components to form ordered domains.

A. Thin Crystalline Films of Cholesterol

Cholesterol is the most abundant sterol in animal tissues playing an important role in determining the rigidity of cell membranes. Faulty control of cholesterol levels may lead to its precipitation, also in crystalline form, in human bodies, prevailing as the pathological processes of atherosclerosis and gallstone formation in the bile.

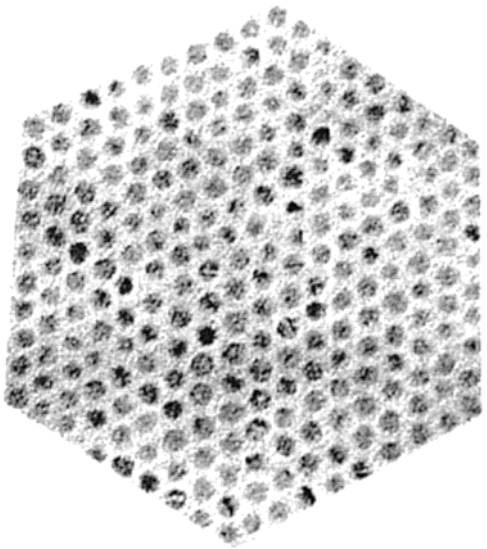

Figure 29. Transmission electron micrograph of a dodecanethiol-capped Ag particle of size 2.8 nm. The particles were extracted from the Langmuir trough at a pressure just below that required to collapse the 2-D film into a 3-D film (Reprinted with permission from J. M. Heath ref 138).

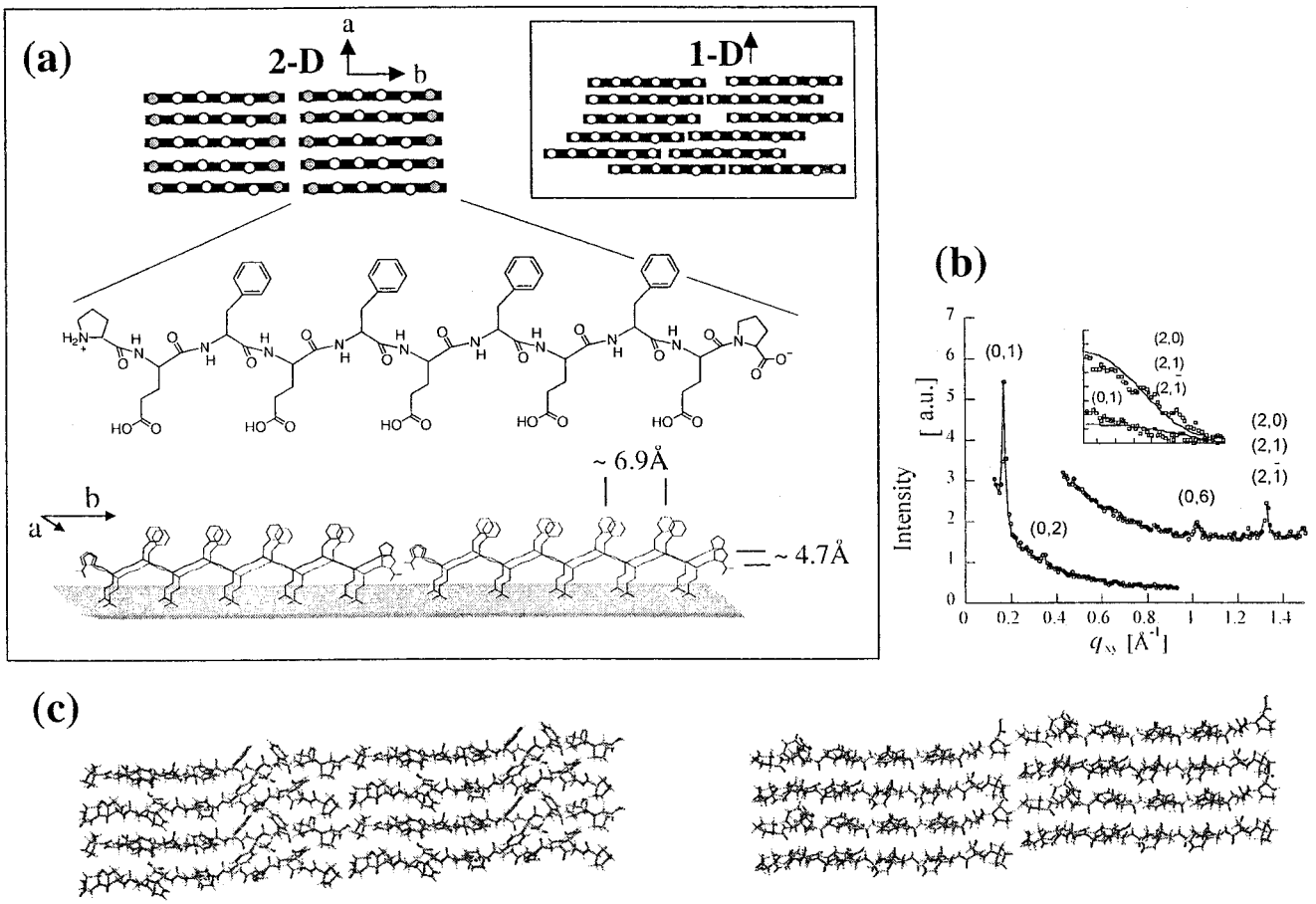

Figure 30. (a) Schematic representations of a β-sheet crystalline assembly of peptide chains at the air−water interface, in the form of one- and two-dimensional (1-D, 2-D) arrangements, and one containing the chemical structure of the peptide Pro-Glu-(Phe-Glu)$_4$−Pro. The repeat distances depicted along the *a* and *b* directions are those that have been observed before for crystalline β-sheet structures. (b) The observed GIXD pattern $I(q_{xy})$ of the crystalline monolayer Pro-Glu-(Phe-Glu)$_4$−Pro film on deionized water. Inset contains the observed and calculated Bragg rod profiles $I(q_z)$ that correspond to the packing arrangements shown. (c) View perpendicular to the plane of the β-sheet of the two model packing arrangements of Pro-Glu-(Phe-Glu)$_4$−Pro each forming hydrogen-bonded ribbons, and assumed to be randomly disordered in order to yield the calculated Bragg rods shown in (b).

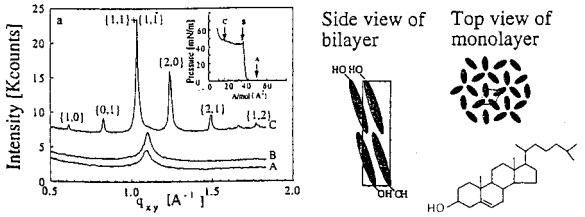

Figure 31. (Left): GIXD intensity patterns $I(q_{xy})$ of a film of cholesterol on water at different compressions. (Inset): The surface pressure−area isotherm at 5 °C with arrows indicating the points at which the GIXD measurements were made. (Right): Schematic packing arrangements of the bilayer (side view) and of the monolayer (top view).

A film of cholesterol at the air−water interface[147] in the uncompressed state exhibits one broad reflection (Figure 31, left, curve A) corresponding to a crystalline lateral coherence length of about 70 Å. The Bragg rod profile of that peak indicates a monolayer with the long axis of the molecules aligned normal to the plane of the water. A hexagonal unit cell $a = b = 6.6$ Å containing one molecule would be the most basic structure that can be assigned for this single reflection, but such a lattice implies high librational motion about the long molecular axis, which is precluded since the intermolecular contacts would be too close. However, a trigonal crystal composed of a unit cell $a' = b' = \sqrt{3}a$ containing three molecules of cholesterol related by a 3-fold symmetry (see Figure 31, right) meets the condition of acceptable intermolecular contacts, and calculated X-ray structure factors are in agreement with the experimental diffraction data.[148]

High compression (see inset to Figure 31, left) gives rise to several sharp Bragg reflections (curve C) corresponding to a rectangular unit cell $a = 10.1$ Å, $b = 7.6$ Å, containing two molecules in the layer plane. The widths of the Bragg rods point to a bilayer of 35 Å (Figure 31, center). This rectangular unit cell is fingerprint evidence of a particular layer packing found in several cholesterol-like molecules. Addition of certain phospholipids at 1:1 or 1:10 molar ratio of phospholipid to cholesterol depresses formation of cholesterol in the crystalline bilayer form.[147] Further structure analysis yielded the packing arrangement of the crystalline bilayer, and additional experimental GIXD data showed a transformation from the cholesterol bilayer to a crystalline trilayer phase that incorporated a layer of ordered water.[148] This structure proved to be similar to that of the macroscopic cholesterol monohydrate phase, a form found in

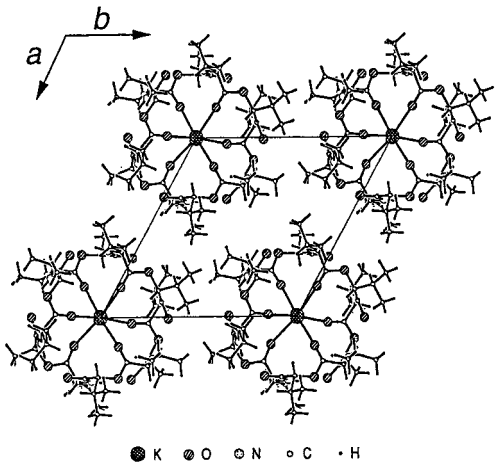

Figure 32. Monolayer crystalline structure of the valinomycin-potassium ion complex on KCl solution, the molecule adopting a bracelet-like shape.

pathological precipitants. It is also noteworthy that stigmasterol, which has a molecular structure akin to cholesterol but for a more bulky exocyclic moiety, forms, upon compression on the water surface, a crystalline trilayer with a layer of occluded water molecules between the top two cholesterol layers. This arrangement is similar to, but not the same as, stigmasterol hemihydrate, the crystalline bulk form.[148]

B. Crystalline Films of Ion-Bound Ionophores

Ionophores are capable of selectively carrying ions across natural and artificial membranes. The ion transport is associated with structural reorganization that takes place inside the membrane and at its interface. Valinomycin, a cyclic dodecadepsipeptide, is highly selective to binding of potassium and rubidium cations; Nonactin, a cyclic macrotetrolide, complexes efficiently with ammonium, potassium, and sodium cations. Physicochemical studies, aiming at revealing the mechanism of ion transport by ionophores, have been the major source of information regarding the conformations adopted by ionophores in different solvents and in the presence of ions.

Structural studies of model membranes containing ionophores as films at air−solution interfaces should contribute to the elucidation of the processes that take place at the hydrophilic−hydrophobic interface and inside the 2-D environment of the long chain lipids. Moreover, this type of study may also be of benefit for the design of ionoselective films for electrodes and sensors utilizing supramolecular architectures containing ionophores.

GIXD has been applied for study of the structural characteristics of 2-D crystallites of the ionophores valinomycin and nonactin when complexed with various cations at the air−solution interface.[149] Valinomycin on KCl solution and thus complexed with K^+ assumes a bracelet shape that packs in a 2-D hexagonal unit cell (Figure 32). Other crystalline phases were formed on potassium iodide and barium perchlorate solutions. The presence of hydrophobic monolayers such as phospholipids or stearic acids, which provide a membrane-like environment, induced ordered stacking of valinomycin−potassium chloride complexes into three to four layers. Nonactin packs in a pseudotetragonal unit cell on solutions of NH_4SCN and KSCN. Upon compression of the nonactin−NH_4SCN film, crystallites about seven layers thick were detected. The observed Bragg rod data could be fitted to a molecular model of the multilayer crystallite exhibiting a structure similar, but not identical, to the known 3-D crystal.

The high molecular symmetry characterizing these ionophores, reflected in their tendency to form 2-D ordered arrays and the relative ease by which multilayers of these complexed ionophores are assembled at interfaces, forming channel-like architectures, may have a bearing on ion transport through membranes, via stacking.

C. Cyclic Peptide Nanotubes

Cyclic peptides of an even number of alternating *R*- and *S*-amino acids have been shown by Ghadiri and co-workers to self-assemble by N−H···O hydrogen bonding into nanoscalar tubular structures.[139] As these architectures have a potential use as size-selective transporting components of molecular devices, biosensors, and drug-delivery systems, it is advantageous to study the principles that govern the organization of these tubular components at interfaces.

The assembly, orientation, and structural features of nanoscalar tubes composed of cyclic peptides formed at the air−water interface were detected by GIXD, complemented by atomic force microscopy (AFM) on transfer to mica support.[150] The eight residue cyclic peptide *cyclo*-[(L-Phe-D-N-MeAla-)$_4$ exhibits 2-D crystallinity in which the peptide ring lies parallel to the water interface in an arrangement similar to its 3-D crystal form. The peptide *cyclo*-[(L-Trp-d-Leu)$_3$-L-Ser-D-Leu] forms mostly aggregates composed of several nanotubes in planar lateral registry assuming a raft-like structure parallel to the air−water interface (Figure 33). The cyclic peptide [(L-Trp-D-Leu)$_4$] has the lowest tendency, if at all, to form a crystalline 2-D array of nanotubes.

This study highlights the factors involved in the formation of ordered arrays of cyclic peptide nanotubes at the air−water interface, a key factor for the generation of a continuous domain of nanotubes oriented normal to the interface resides in achieving a more equal balance between the strong hydrogen-bond energy of attachment of the cyclic peptide to an end of a growing tube as compared to the relatively weak lateral forces between tubes. Bulky and rigid amino acid residues, such as Trp on the tube periphery, do not promote attractive intertube interactions. Smaller and more flexible moieties, particularly Gln and Glu which can form intertube hydrogen bonds, would appear to be more favorable for the formation of extended arrays of tubes oriented normal to the surface.

Here it is worthy of mention that films on water of both mono- and polydisperse samples of α-helical poly (γ-benzyl L-glutamate) has been characterized by Pershan, Tirrell, and co-workers.[151] The film in the

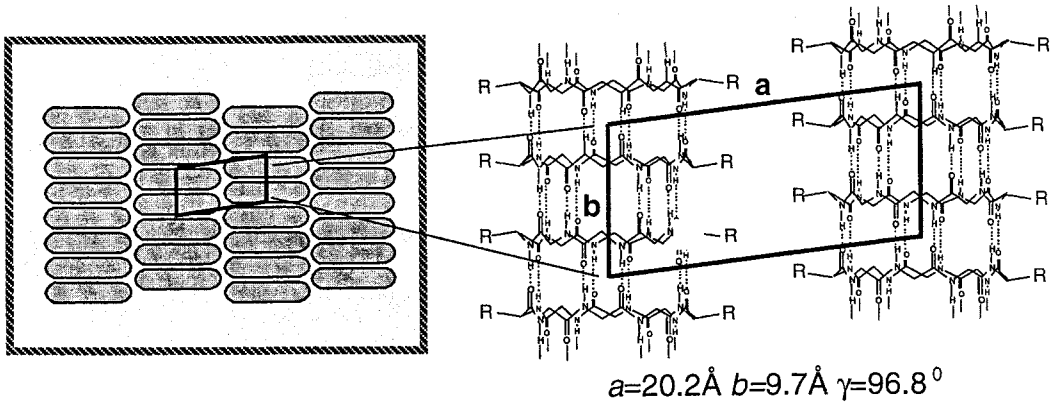

Figure 33. Raft-like structure of the nanotobe composed of the peptide molecules *cyclo* [(*L*-Trp-*D*-Leu)$_3$-*L*-Ser-*D*-Leu].

uncompressed state forms monolayer-like islands according to Brewster angle microscopy images. GIXD data shows an interhelix peak corresponding to parallel alignment of the rodlike α-helices. Compression results in an incomplete and incommensurate second layer with an average density less than the bottom layer according to X-ray reflectivity and GIXD data.

D. 2-D Crystallization of Proteins at the Air–Solution Interface

Several years ago Kornberg, Ribi, and coworkers[152−157] demonstrated by image processing of electron micrographs that 2-D crystals of water-soluble proteins are readily formed at the air−solution interface under monolayers of lipids, some of which contain headgroups which bind specifically to the protein. With this approach, a variety of protein structures have been studied; for example, streptavidin on biotinylated monolayer,[158] characterized to a resolution of about 20 Å, yielded a structure that corresponded well with the 3-D structure determined by X-ray diffraction. In all these electron microscopy studies, the lipid protein layer was transferred onto electron microscope grids and stained. In contrast, the structure at the air−water interface of streptavidin bound to biotinylated lipids has been studied in situ by X-ray and neutron reflectivity;[159,160] a GIXD pattern has also been measured showing broad Bragg peaks compatible with the electron microscopy structure.[161] Recently high-resolution GIXD data on three different proteins bound to lipid monolayers have been recorded yielding crystal coherence lengths several micrometers in size.[162]

GIXD has also been applied to help characterize 2-D crystals of membrane proteins that are not easily amenable to 3-D crystallization. Recently, GIXD patterns have been measured from purple membrane patches at the air−water interface up to a resolution of about 8 Å.[163] At this resolution the electron density map constructed with the phases known from electron microscopy shows the typical arrangement of bacteriorhodopsin α-helices.

X. Summary and Outlook

Over the past decade, enormous strides have been made in the design, characterization, and understanding of molecular assembly in ultrathin films at the air−liquid interface by virtue of surface sensitive methods for in situ investigation of molecular organization at interfaces. Early interest in monolayers of simple chainlike amphiphilic molecules has gradually expanded toward complex supramolecular thin film architectures and membrane proteins at the air−liquid interface. The structural elucidation of thin organic films was mostly due to the development of the GIXD method, complemented by various optical and spectroscopic techniques.

GIXD studies of Langmuir films of the simple amphiphiles such as fatty acids and alcohols has provided a deep insight into the state of their 2-D phases ranging from the 'gaseous' through the 'mesomorphous' to the 'crystalline' state. Other types of amphiphilic molecules of a more complex nature such as phospholipids, cholesterol, and derivatives thereof form mesomorphic or highly crystalline domains. In general, the extent of order depends on factors such as temperature, surface pressure, molecular chain length and flexibility, and the nature of the hydrophilic headgroup and the liquid subphase.

The ability of two- or multicomponent monolayer mixtures to phase separate or form composite phases can also be probed in situ. For example, it has proven possible by GIXD to establish whether racemic mixtures of amphiphiles spread on water form 2-D crystals in which the molecules of opposite handedness either combine to form heterochiral domains or spontaneously segregate into islands of opposite chirality.

The effect of solute molecules on the growth, dissolution, and structure of crystalline monolayers can be monitored. Ordered binding of solute molecules to the amphiphile may be applied for the design of monolayers, which would promote nucleation of 3-D crystals by means of a complementarity between the hydrophilic headgroups of the monolayer and the layer arrangement of the to-be-nucleated crystal. Monitoring the induced crystallization of ice under the long-chain alcohol monolayers by GIXD has provided information on the minimum critical size of the induced nuclei.

GIXD experiments have shown that crystalline multilayers may be readily formed by bolaamphiphiles, whose headgroups form interlayer hydrogen bonds, as well as by molecules as diverse as long-

chain *normal* alkanes, oligothiophenes, and nylon polymers.

The GIXD studies of the crystalline multilayer films at the air−liquid interface casts light on the general phenomenon of crystal polymorphism. Several systems were found to form polymorphic thin film crystallites on liquid surfaces. In addition, some multilayer structures on the liquid surface were similar to, but not the same as, their 3-D macroscopic counterpart. For example, cholesterol bilayer and stigmasterol trilayer were found to have crystal structures different than that of the corresponding bulk form, which may be of relevance to the possible state of cholesterol within biological membranes and mechanisms of crystallization therefrom.

The data on multilayer crystals suggest that nuclei of 3-D crystals growing in solution may be composed of aggregates of different structures, some of which are akin to, but not the same as, that of the stable macroscopic crystal. Such a hypothesis was assumed for the control of crystal polymorphism using tailor-made additives designed to inhibit nucleation of undesired polymorphs.[94,164] Moreover, interlayer growth of multilayer crystals may be inhibited and their polymorphic behavior, if present, controlled with tailor-made additives.

Supramolecular architectures may be formed at the air−solution interface and their structures elucidated. These include grids composed of water-insoluble ligand molecules and water-soluble metal ions, superlattices of organically capped metal nanocrystal monolayers, 2-D superlattices formed by peptide chains arranged in β-sheet monolayers, and raft-like aggregates composed of peptide nanotubes. Structure determination of such thin film architectures can be achieved in favorable cases to near atomic resolution by a combination of experimental and computational techniques. The more complex molecular systems require X-ray structure-factor least-squares refinement using the GIXD data but with constraints imposed on the structure.

In the future we may anticipate advances not only in the design, preparation, and structural elucidation of thin film architectures, but also such films of relevance to dynamic processes and reactions at interfaces.

XII. Acknowledgments

We are deeply indebted to our former collaborators who have contributed to several of the studies reviewed here. The work of our group was supported by the following funding agencies: the US Israel Binational Science Foundation, the German Israel Science Foundation, the Minerva Foundation, the Petroleum Research Fund, the G.M.J. Schmidt Minerva Center for Supramolecular Architectures, the Israel Academy of Sciences, and the Danish Foundation for Natural Sciences. We gratefully acknowledge HASYLAB at DESY, Hamburg, Germany, for synchrotron beamtime received over the years.

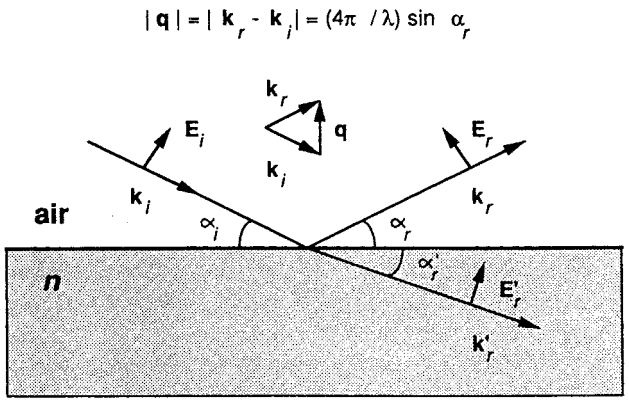

Figure 34. Refracted ($\boldsymbol{E}'_r$) and reflected ($\boldsymbol{E}_r$) waves resulting from an incident plane wave with amplitude E_i upon an interface between air and a material of refraction index n. Electric fields $\boldsymbol{E}$ are illustrated for one polarization only. The symbol $\boldsymbol{q}$ is the scattering vector, with $\boldsymbol{k}_i$ and $\boldsymbol{k}_r$ the incident and reflected wave vectors of magnitude $2\pi/\lambda$, where λ is the wavelength. Note that as $n \lesssim 1$, $\alpha'_r < \alpha_i = \alpha_r$. This provides for total reflection at angles $\alpha_r < \alpha_c$, where α_c is the critical angle for total external reflection.

XIII. Appendix

A. Surface-Sensitive X-ray methods

The intensity measured in a conventional X-ray scattering experiment is proportional to the number of scatterers, i.e., the irradiated sample volume. This, in turn, is proportional to the penetration depth of the radiation in a sample. For X-rays of about 1 Å wavelength, this penetration ranges from a few micrometers for highly absorbing materials to a few millimeters for low absorbing materials. Consequently, scattering from the top region about 100 Å deep shall be so weak compared to that from the bulk that it will be completely swamped. A method restricting the penetration depth to the surface region is, therefore, a prerequisite for all surface diffraction/scattering experiments. This can be achieved by using grazing angles of incidence and employing the phenomenon of total external reflection from the surface.

The refractive index n of matter for X-rays in the 1 Å wavelength range is given by eq 1,[165] where $\delta = 2\pi\rho r_o/k^2$. $k = 2\pi/\lambda$ is the X-ray wavelength where λ is the wavelength, ρ is the electron density, and $r_o = 2.82 \times 10^{-13}$ cm is the classical electron radius. Typically δ is on the order of 10^{-5}. The term β is equal to $-\mu/2\kappa$, where μ is the linear absorption coefficient. For X-rays of wavelength $\lambda \approx 1$ Å, absorption is small and $\beta \ll \delta$.

$$n = 1 - \delta - i\beta \qquad (1)$$

Consider now a plane wave with wavevector k_i incident at an angle α_i on a planar interface separating a homogeneous medium from the vacuum as shown in Figure 34. The wave will be partially reflected into the vacuum in the direction given by $\alpha_r = \alpha_i$ and partially refracted into the lower medium in the direction given by α'_r. Snell's law for this case yields eq 2.

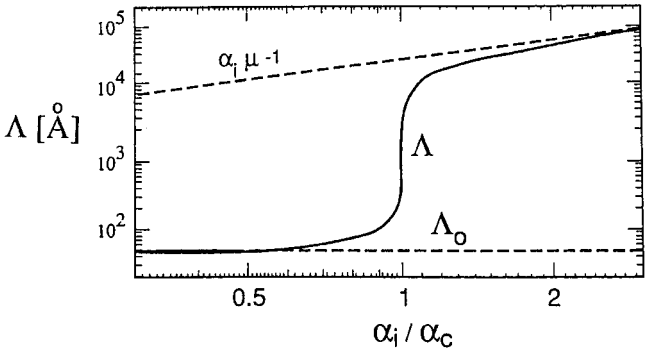

Figure 35. X-ray beam penetration depth Λ in water at $\lambda = 1.38$ Å versus incidence angle α_i/α_c, α_c being the critical angle for total external reflection. The limiting value Λ_o of the penetration depth for $\alpha_i/\alpha_c \ll 1$ is a characteristic materials constant, $\Lambda_o = (\pi r_o \rho)^{-1/2}/4$, independent of the X-ray wavelength λ. For $\alpha_i/\alpha_c \gg 1$ the penetration depth is $\alpha_i \mu^{-1}$ where the linear absorption coefficient μ does depend on λ.

$$n \cos \alpha'_r = \cos \alpha_i \qquad (2)$$

As $n < 1$, for angles of incidence α_i less than or equal to an angle α_c, which is defined as $\alpha_c = \cos^{-1}(n) = (2\delta)^{1/2}$, the well-known phenomenon of total reflection occurs:[166] the incident wave is totally reflected, while the refracted wave becomes evanescent travelling along the surface. The amplitude of the evanescent wave decays exponentially with depth. Figure 35 shows the penetration depth Λ of the X-rays in water versus angle of incidence α_i. For $\alpha_i < 0.5\alpha_c$, the penetration depth is about 50 Å independent of wavelength. The evanescent wave may, therefore, be diffracted by crystalline material in a surface layer of that thickness and provides information on its in-plane structure. Such diffraction is called grazing incidence X-ray diffraction (GIXD).[167,168]

1. Principles of Grazing Incidence X-ray Diffraction

In three-dimensional crystals (3-D), diffraction from a set of crystal planes with an interplanar spacing d occurs only when the Bragg law is satisfied. Namely, when, first, the scattering vector length q (given by $|\boldsymbol{k}_{out} - \boldsymbol{k}_{in}| = 4\pi \sin\theta/\lambda$, where the wave vector $\boldsymbol{k}$ is of length $2\pi/\lambda$ and the angle between $\boldsymbol{k}_{out}$ and $\boldsymbol{k}_{in} = 2\theta$) is equal to $2\pi d^*$, where d^* is the reciprocal of the interplanar spacing d, and, second, the normal to the planes bisect between the incident and outgoing beams (Figure 36, top). This condition may be mathematically expressed in terms of the reciprocal lattice vectors $\boldsymbol{d}^* = h\boldsymbol{a}^* + k\boldsymbol{b}^* + l\boldsymbol{c}^*$, where $\boldsymbol{a}^*,\boldsymbol{b}^*,\boldsymbol{c}^*$ are the reciprocal vectors of the unit-cell axes $\boldsymbol{a},\boldsymbol{b},\boldsymbol{c}$ and h,k,l are integers that represent the Miller indices of planes with a spacing $d_{hkl} = 1/d^*_{hkl}$. Diffraction, therefore, takes place in 3-D crystals from a set of planes with indices (h,k,l) only when the scattering vector $\boldsymbol{q}$ coincides with the vector $2\pi\boldsymbol{d}^*$ (Figure 36, top).

For a 2-D crystal there are no selection rules or restrictions on the scattering vector component $\boldsymbol{q}_z$ along the film normal. Thus, the Bragg scattering extends as continuous rods (BR) through the 2-D reciprocal lattice points (Figure 36, bottom).[169,170]

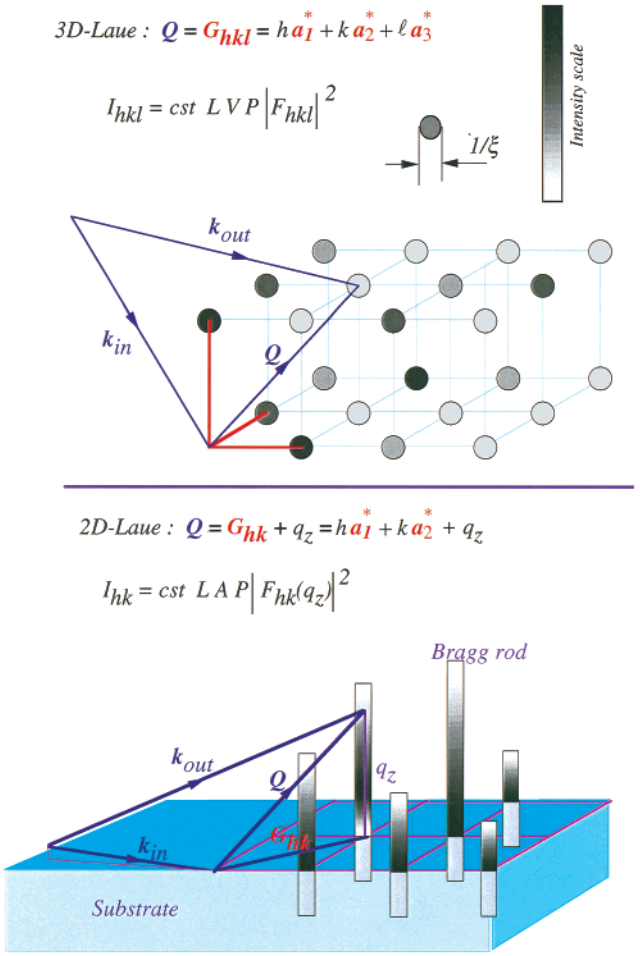

Figure 36. The conditions for diffraction from: (top) A 3-D crystal; (bottom) A 2-D crystal. Diffraction from a particular set of h,k,l planes of a 3-D crystal will be achieved if the scattering vector $\boldsymbol{q}$ is coincident with the reciprocal lattice vector $2\pi(h\boldsymbol{a}^*+k\boldsymbol{b}^*+l\boldsymbol{c}^*)$. For a 2-D crystal the diffraction for a particular value of q_z of an (h,k) Bragg rod requires that the horizontal component $\boldsymbol{q}_{xy}$ of the vector $\boldsymbol{q}$, is coincident with the reciprocal lattice vector $2\pi(h\boldsymbol{a}^*+k\boldsymbol{b}^*)$. The axes $2\pi(\boldsymbol{a}^*,\boldsymbol{b}^*,\boldsymbol{c}^*) = (\boldsymbol{a}_i^*, i = 1,3)$ in the figure.

Diffraction, therefore, takes place only when the horizontal component of $\boldsymbol{q}$, given by $\boldsymbol{q}_{xy}$, coincides with a vector $2\pi(h\boldsymbol{a}^* + k\boldsymbol{b}^*)$. The finite thickness of the 2-D crystal causes the BR to extend over finite $\boldsymbol{q}_z$ intervals. The intensity distribution along these intervals is determined by the vertical electron density distribution in the molecules and is expressed as the Fourier transform of the resulting electron density along the film normal.

In the GIXD geometry (Figure 37), the angle of incidence of the X-ray beam α_i is kept just below the critical angle, limiting the penetration of the beam to that of an evanescent wave with a depth in the range 50−100 Å. X-ray scattering due to the subphase is thus efficiently eliminated, which allows an accurate measurement of the weak signals originating from the crystalline film. The evanescent wave is diffracted by the two-dimensional order in the film, resulting in a beam that makes an angle α_f with the water surface (see Figure 37). If the order is crystalline, the evanescent wave may be Bragg scattered from a grain which is oriented so that its h,k lattice

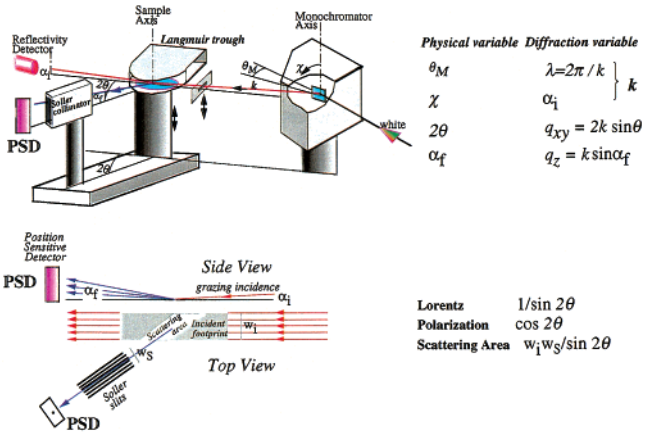

Figure 37. (Top) Experimental setup of the diffractometer at beamline BW1 (X-ray synchrotron source at Hasylab, Hamburg) for studying liquid surfaces. The white X-ray beam is monochromated and deflected down toward the sample by tilting the Be monochromator crystal in Laue geometry. The incident and specular reflected beam intensities are monitored by the NaI Beam Monitor and the NaI XR Detector, respectively. The diffracted beam is detected with a position-sensitive detector (PSD). (Bottom) Side and top views of the grazing incidence X-ray diffraction geometry. The PSD has its axis along the vertical. Only the cross-beam area contributes to the measured scattering. The Soller collimator defines the horizontal resolution of the detector.

"planes", with a $d_{h,k}$ spacing, make an angle $\theta_{h,k}$ with the evanescent beam fulfilling the Bragg condition $\lambda = 2d_{h,k}\sin\theta_{h,k}$. The grazing incidence beam illuminates a certain footprint of the surface. In general, the layerlike crystallites on the water surface are azimuthally randomly oriented and so may be described as a "two-dimensional powder".

As shown in Figure 37, the collection of the diffracted radiation by means of a position-sensitive detector (PSD) is made by scanning the detector over a range along the horizontal scattering vector q_{xy} ($\approx 4\pi \sin\theta_{xy}/\lambda$), where $2\theta_{xy}$ is the angle between the incident and diffracted beams projected onto the horizontal plane, and integrating over the whole q_z window of the PSD to yield the Bragg peaks. Simultaneously, the scattered intensity recorded in channels along the PSD, but integrated over the scattering vector q_{xy} in the horizontal plane across a Bragg peak, produce q_z-resolved scans called Bragg rods. For various purposes the scattered intensity may also be presented in 2-D contour plots as a function of q_{xy} and q_z.

Several different types of information may be extracted from the measured profiles. The angular 2θ positions of the Bragg peaks yield the repeat distances $d = 2\pi/q_{xy}$ for the 2-D lattice structure. The Bragg peaks may be indexed by the two Miller indices h,k to yield the a,b unit cell. The full-width at half-maximum (fwhm) of the Bragg peaks in q_{xy} units yields the crystalline coherence length L in the a,b plane associated with the h,k reflection. The intensity at a particular value of q_z in a Bragg rod is determined by the square of the molecular structure factor $|F_{h,k}(q_z)|^2$. The structure factor $F_{h,k}(q_z)$ is given by eq 3, where f_j is the scattering factor of atom j, $x_j\boldsymbol{a} + y_j\boldsymbol{b}$ is the vector specifying the position of atom j in the unit cell, and z_j is the atomic coordinate along the vertical direction.

$$F_{h,k}(q_z) = \Sigma f_j \exp i[2\pi(hx_j + ky_j) + q_z z_j] \qquad (3)$$

The measured intensity is given by eq 4

$$I_{h,k}(q_z) = \mathrm{I}V(q_z)|F_{h,k}(q_z)|^2 \qquad (4)$$

In general, the observed Bragg rod intensity is a sum over the (h,k) and $(-h,-k)$ reflections since they coincide at $2\theta_{hk}$ (or q_{hk}) positions because the crystalline film on the liquid surface is generally a "two-dimensional powder". The factor $V(q_z)$ describes the interference of X-rays diffracted upward with X-rays diffracted down and subsequently reflected up by the interface.[169] The factor $V(q_z)$ differs from 1 only in the vicinity of $q_z = 1/2q_c$, where it contributes a sharp peak to the intensity. Thus, in eq 3 the most important variation is due to the structure factor $|F_{h,k}(q_z)|^2$.

For molecules of arbitrary shape, the overall crystalline structure can be established from an analogous 3-D crystal structure if known, or by trial and error, and eventually by constrained least-squares refinement to near atomic resolution in favorable systems. For the simple linear surfactant molecules that contain aliphatic hydrocarbon chains, the square of the structure factor is a bell-shaped function which reaches its maximum when the scattering vector $\boldsymbol{q} = (\boldsymbol{q}_{hk}, \boldsymbol{q}_z)$ is orthogonal to the molecular axis. Thus, for chainlike molecules, precise information on the molecular chain orientation in a 2-D crystal may be obtained from the positions of the maxima of the Bragg rods, assuming the chains to be uniformly tilted[2] as demonstrated in Figure 38 for three different packing arrangements.

2. Specular X-ray Reflectivity

The variation in electron density of a film floating on the water surface in the direction normal to that of the surface can be obtained from specular X-ray reflectivity measurements. Specular reflection implies that the reflected ray measured is in the plane spanned by the incident wavevector k_i and the vector normal to the surface and that $\alpha_i = \alpha_r$ (Figure 34). The specular reflectivity of an ideal surface is given by the well-known Fresnel law of optics.[166] In the limit of small angle of incidence,[2,171−173] applicable here, and where absorption effects are neglected, it is given by eq 5, where $q_z = (4\pi/\lambda)\sin\alpha_i$ and $q_c = (4\pi/\lambda)\sin\alpha_c$ is the critical value of q_z for total external reflection. For $q_z < q_c$, eq 5 yields $R_F = 1$, i.e., total reflection. As q_z is increased beyond q_c, however, R_F decreases and, for $q_z \geq 4q_c$, approaches $R_F(q_z) \approx (q_c/2q_z)$.[4] As the range of interest may extend to $q_z/q_c \approx 30$ or more,[2,171−173] reflectivities down to 10^{-8} have to be measured. Hence, the importance of high-intensity synchrotron sources or high-power rotating anode X-ray generators for XR measurements. It is important to note that eq 5 is valid only for an ideally flat surface across which the electron density $\rho(z)$

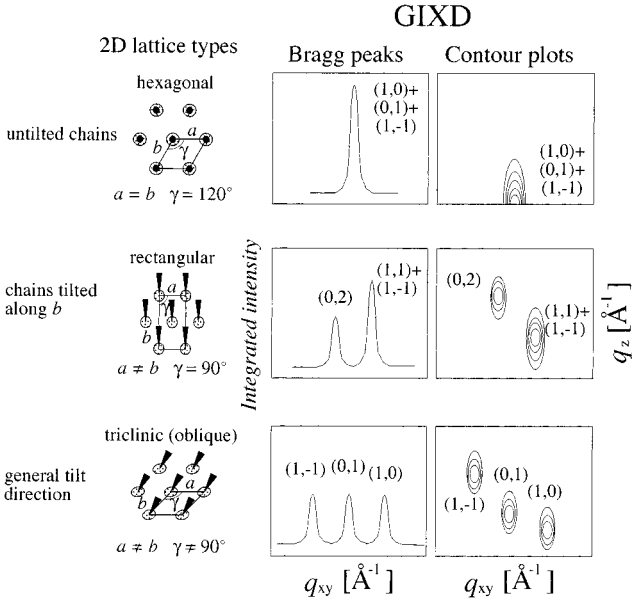

Figure 38. Three monolayer crystal packing arrangements of alkyl chains (left column) and their diffraction patterns (central and right columns) assuming the monolayer is in a 2-D "powder" form. We assume the chains are cylindrical rods. The middle column shows the Bragg peaks $I(q_{xy})$ each integrated over q_z, and the right column shows the Bragg rod pattern $I(q_{xy},q_z)$ in the form of a contour plot. When the molecular axis is perpendicular to the water surface the lattice is hexagonal (top row), and the three {1,0}, {0,1} and {1,−1} reflections coincide. The Bragg rod obtained from the single in-plane diffraction peak has its maximum at $q_z = 0$ Å^{-1}. When the molecular axis is tilted toward nearest neighbors along the *a* axis (middle row), the unit cell is centered rectangular, yielding two Bragg peaks. One comprises two coincident reflections and the other is a singlet. The Bragg rod of the two degenerate reflections (1,1) and (1,−1) is centered at $q_z \geq 0$ Å^{-1}, the position of the center depending upon the extent of the molecular tilt. The singlet corresponds to the (0,2) reflection whose Bragg rod is centered around $q_z = 0$ Å^{-1}. Finally, the molecular axis tilted in a nonsymmetry direction, yields an oblique 2-D lattice (bottom row). The peak positions of the three Bragg rods determine the chain tilt angle as well as the azimuthal position of the chain *vis*-à-vis the unit cell axes.

varies steplike between two constant values. If $\rho(z)$ is not a step function but varies continuously in the surface region, the reflectivity is modified,[2,171−173] yielding eq 6, where ϕ is defined as in eq 7 and ρ_∞ is the constant electron density in the subphase bulk. Thus, by measuring $R(q_z)$ it is possible, in principle, to determine $\rho(z)$, the variation of the electron density normal to the surface, and, in particular, the electron density of a monolayer floating on it. ϕ is a complex function, and only its modulus can be derived from the measured reflectivity but not its phase. Thus, one is faced with the usual phase problem of X-ray crystallography, and therefore, to date virtually all specular reflectivity data has been analyzed by fitting a parametrized model density $\rho(z)$ to the measured data via eqs 5−7.

$$R_F(q_z) = [\{q_z - (q^2{}_z - q^2{}_c)^{1/2}\}/\{q_z + (q^2{}_z - q^2{}_c)\}^{1/2}]^2 \quad (5)$$

$$R(q_z) = R_F(q_z)|\phi(q_z)|^2 \quad (6)$$

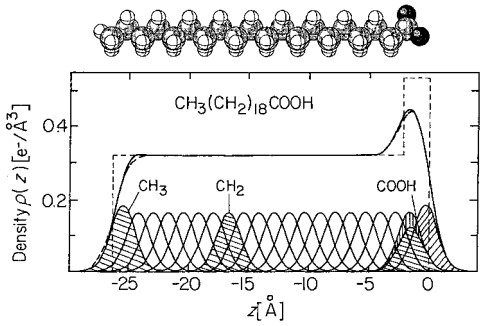

Figure 39. Top: Space-filling model of the molecule $C_{19}H_{39}COOH$ at the water surface. Bottom: Full lines: The total electron density at the interface is the sum of contributions from the subphase and the monolayer. The monolayer density is the sum of contributions from individual atoms of the amphiphile. Thermally excited capillary waves lead to an rms diffuseness σ, and all densities are smeared accordingly. The density may alternatively be described by a two-box model (dotted line) which, smeared by σ (dashed line), agrees well with the profile calculated from contributions from the individual atoms (full line).

where

$$\phi(q_z) = (1/\rho_\infty) \int [d\rho(z)/dz] \exp(iq_z z)dz \quad (7)$$

One strategy employed has been to generate $\rho(z)$ as the sum of densities $\rho_i(z)$ from individual atoms at height $z = z_i$ and refine this *atomic model* of the monolayer molecules under suitable constraints. [18] A typical constraint would be that the hydrophobic moiety must tilt as a rigid body, i.e., without distorting the a priori assumed internal bond lengths and angles. Adjustable parameters, then, would be the tilt angle of each molecular segment, the height of the molecule above the interface, and the area per molecule.

A computationally slightly simpler strategy is to represent the monolayer as a stack of slabs,[174] each with a constant density ρ_i and thickness l_i. Two such slabs would be needed for representing a simple fatty alcohol or acid monolayer.[175] When refining such a *slab model*, a possible choice of fit parameters, then, would be the densities ρ_i and thicknesses l_i of the slabs.

For either representation of the monolayer, the constant density of the semi-infinite subphase has to be added below the interface. Finally, either model density must be smeared out in the *z*-direction to account for the vertical roughness or diffuseness of the interface. The root-mean-square roughness, σ, is on the order of 3 Å and stems mainly from thermally excited capillary waves on the water surface.[2,172,173] It leads to a Debye−Waller factor $\exp(-q_z^2\sigma^2)$ in $|\phi(q_z)|^2$ (eq 5).

The rather large value of $\sigma \approx 3$ Å (equivalent in normal crystallographic parlance to $B = 8\pi^2\sigma^2 \approx 700$ Å^2) means that in the atomic model of $\rho(z)$ it is unnecessary to use accurate charge densities for the atoms; so long as each atom contributes its proper charge Z_i, the description will be adequate. Also, replacing groups of atoms by pseudoatoms is feasible. The large value of σ is also the reason that the monolayer may be adequately represented by the slab model. This is illustrated in Figure 39, which shows

that the density $\rho(z)$ of a fatty acid monolayer may be represented by either model.

XIV. References

(1) Larson, M. A.; Garside, J. *Chem. Eng. Sci.* **1986**, *41*, 1285.
(2) *Phase Transitions in Soft Condensed Matter*; Als-Nielsen, J., Kjaer, K., Eds.; Plenum Press: New York: Geilo, Norway, 1989; Vol. 211, Series B, p 113.
(3) Als-Nielsen, J.; Möhwald, H. In *Handbook on Synchrotron Radiation*; Ebashi, S., Rubinstein, E., Koch, M., Eds.; North-Holland: Amsterdam, 1991; Vol. IV.
(4) Jacquemain, D.; Grayer Wolf, S.; Leveiller, F.; Deutsch, M.; Kjaer, K.; Als-Nielsen, J.; Lahav, M.; Leiserowitz, L. *Angew. Chem., Int. Ed. Engl.* **1992**, *31*, 130.
(5) Als-Nielsen, J.; Jacquemain, D.; Kjaer, K.; Leveiller, F.; Lahav, M.; Leiserowitz, L. *Phys. Rep.* **1994**, *246*, 251.
(6) Dutta, P. *Curr. Opin. Solid State Mater. Sci.* **1997**, *2*, 557.
(7) Berge, B.; Lenne, P. F.; Renault, A. *Curr. Opin. Colloid Interface Sci.* **1998**, *3*, 321.
(8) Weissbuch, I.; Popovitz-Biro, R.; Lahav, M.; Leiserowitz, L.; Kjaer, K.; Als-Nielsen, J. In *Advances in Chemical Physics*; Prigogine, I., Rice, S. A., Eds.; J. Wiley: New York, 1997; Vol. 102; p 39.
(9) Rapaport, H.; Kuzmenko, I.; Berfeld, M.; Kjaer, K.; Als-Nielsen, J.; Popovitz-Biro, R.; Weissbuch, I.; Lahav, M.; Leiserowitz, L. *J. Phys. Chem. B* **2000**, *104*, 1399.
(10) McConnell, M. *Annu. Rev. Phys. Chem.* **1991**, *42*, 171.
(11) Knobler, C. M.; Desai, R. *Annu. Rev. Phys. Chem.* **1992**, *43*, 207.
(12) Seul, M.; Andelman, D. *Science* **1995**, *267*, 476.
(13) Kaganer, V. M.; Mohwald, H.; Dutta, P. *Rev. Mod. Phys.* **1999**, *71*, 779.
(14) Moore, B. G.; Knobler, C. M.; Akamatsu, S.; Rondelez, F. *J. Phys. Chem.* **1990**, *94*, 4588.
(15) Peterson, I. R.; Kenn, R. M. *Langmuir* **1994**, *10*, 4645.
(16) Kjaer, K.; Als-Nielsen, J.; Helm, C. A.; Laxhuber, L. A.; Möhwald, H. *Phys. Rev. Lett.* **1987**, *58*, 2224.
(17) Dutta, P.; Peng, J. B.; Lin, B.; Ketterson, J. B.; Prakash, M.; Georgopoulos, P.; Ehrlich, S. *Phys. Rev. Lett.* **1987**, *58*, 2228.
(18) Grayer Wolf, S.; Leiserowitz, L.; Lahav, M.; Deutsch, M.; Kjaer, K.; Als-Nielsen, J. *Nature* **1987**, *328*, 63.
(19) Kuzmenko, I.; Kaganer, V. M.; Leiserowitz, L. *Langmuir* **1998**, *14*, 3882.
(20) Leveiller, F.; Jacquemain, D.; Leiserowitz, L.; Kjaer, K.; Als-Nielsen, J. *J. Phys. Chem.* **1992**, *96*, 10380.
(21) Majewski, J.; Popovitz-Biro, R.; Bouwman, W. G.; Kjaer, K.; Als-Nielsen, J.; Lahav, M.; Leiserowitz, L. *Chem. Eur. J.* **1995**, *1*, 304.
(22) Weissbuch, I.; Berfeld, M.; Bouwman, W.; Kjaer, K.; Als-Nielsen, J.; Lahav, M.; Leiserowitz, L. *J. Am. Chem. Soc.* **1997**, *119*, 933.
(23) Jacquemain, D.; Leveiller, F.; Weinbach, S.; Lahav, M.; Leiserowitz, L.; Kjaer, K.; Als-Nielsen, J. *J. Am. Chem. Soc.* **1991**, *113*, 7684.
(24) Jacquemain, D.; Wolf, S. G.; Leveiller, F.; Frolow, F.; Eisenstein, M.; Lahav, M.; Leiserowitz, L. *J. Am. Chem. Soc.* **1992**, *114*, 9983.
(25) Eaton, D. F.; Smart, B. E. *J. Am. Chem. Soc.* **1990**, *112*, 2821.
(26) Shin, S.; Collazo, N.; Rice, S. A. *J. Chem. Phys.* **1992**, *96*, 1352.
(27) Leveiller, F.; Jacquemain, D.; Lahav, M.; Leiserowitz, L.; Deutsch, M.; Kjaer, K.; Als-Nielsen, J. *Science* **1991**, *252*, 1532.
(28) Leveiller, F.; Böhm, C.; Jacquemain, D.; Möhwald, H.; Leiserowitz, L.; Kjaer, K.; Als-Nielsen, J. *Langmuir* **1994**, *10*, 819.
(29) Böhm, C.; Leveiller, F.; Jacquemain, D.; Möhwald, H.; Kjaer, K.; Als-Nielsen, J.; Weissbuch, I.; Leiserowitz, L. *Langmuir* **1994**, *10*, 830.
(30) Wang, J. L.; Leveiller, F.; Jacquemain, D.; Kjaer, K.; Als-Nielsen, J.; Lahav, M.; Leiserowitz, L. *J. Am. Chem. Soc.* **1994**, *116*, 1192.
(31) *Crystal Growth*; Hartman, P., Ed.; North-Holland Publishing Co.: Amsterdam, 1973; Vol. 1, p 367.
(32) Fradin, C.; Braslau, A.; Luzet, D.; Alba, M.; Gourir, C.; Daillant, J.; Grubel, G.; Vignaud, G.; Legrand, J. F.; Lal, J.; Petit, J. M.; Rietord, F. *Physica B* **1998**, *248*, 310.
(33) Daillant, J. *Synchrotron Radiat. News* **1999**, *12*, 17.
(34) Quina, F. H.; Whitten, D. G. *J. Am. Chem. Soc.* **1977**, *99*, 877.
(35) Zhao, X.-M.; Perlstein, J.; Whitten, D. G. *J. Am. Chem. Soc.* **1994**, *116*, 10463.
(36) Tieke, B.; Enkelman, V.; Kapp, H.; Lieser, G.; Wegner, G. *J. Macromol. Sci. Chem.* **1981**, *A15*, 1045.
(37) Koch, H.; Laschewski, A.; Ringsdorf, H.; Teng, K. *Makromol. Chem.* **1986**, *187*, 1843.
(38) Tanaka, Y.; Nakayama, K.; Iijima, S.; Shimizu, T.; Maitani, Y. *Thin Solid Films* **1985**, *133*, 165.
(39) Schmidt, G. M. J. *Pure Appl. Chem.* **1971**, *51*, 647.
(40) Weissbuch, I.; Bouwman, W. G.; Kjaer, K.; Als-Nielsen, J.; Lahav, M.; Leiserowitz, L. *Chirality* **1998**, *10*, 60.
(41) Tollner, K.; Popovitz-Biro, R.; Lahav, M.; Millstein, D. *Science* **1997**, *278*, 2100.
(42) Eckardt, C. J.; Peachey, N. M.; Swanson, D. R.; Takacs, J. M.; Khan, M. A.; Gong, X.; Kim, J.-H.; Wang, J.; Uphaus, R. A. *Nature* **1993**, *362*, 614.
(43) Stevens, F.; Dyer, D. J.; Walba, D. M. *Angew. Chem., Int. Ed. Engl.* **1996**, *35*, 900.
(44) Nassoy, P.; Goldmann, M.; Bouloussa, O.; Rondelez, F. *Phys. Rev. Lett.* **1995**, *75*, 457.
(45) Andelman, D.; Gennes, P. G. d. *C. R. Acad. Sci.* **1988**, *307*, 323.
(46) Andelman, D.; Orland, H. *J. Am. Chem. Soc.* **1993**, *115*, 12322.
(47) Kuzmenko, I.; Kjaer, K.; Als-Nielsen, J.; Lahav, M.; Leiserowitz, L. *J. Am. Chem. Soc.* **1999**, *121*, 2657.
(48) Arbel-Hadad, M.; Lahav, M.; Leiserowitz, L. *J. Phys. Chem.* **1998**, *102*, 1543.
(49) Majewski, J.; Popovitz-Biro, R.; Edgar, R.; Arbel-Haddad, M.; Kjaer, K.; Bouwman, W.; Als-Nielsen, J.; Lahav, M.; Leiserowitz, L. *J. Phys. Chem. B* **1997**, *101*, 8874.
(50) Weinbach, S. P.; Weissbuch, I.; Kjaer, K.; Bouwman, W. G.; Als-Nielsen, J.; Lahav, M.; Leiserowitz, L. *Adv. Mater.* **1995**, *7*, 857.
(51) Du, Q.; Superfine, R.; Freysz, E.; Shen, Y. R. *Phys. Rev. Lett.* **1993**, *70*, 2313.
(52) Gavish, M.; Popovitz-Biro, R.; Lahav, M.; Leiserowitz, L. *Science* **1990**, *250*, 973.
(53) Popovitz-Biro, R.; Wang, J. L.; Majewski, J.; Shavit, E.; Leiserowitz, L.; Lahav, M. *J. Am. Chem. Soc.* **1994**, *116*, 1179.
(54) Weinbach, S. P.; Jacquemain, D.; Leveiller, F.; Kjaer, K.; Als-Nielsen, J.; Leiserowitz, L. *J. Am. Chem. Soc.* **1993**, *115*, 11110.
(55) Weinbach, S. P.; Kjaer, K.; Als-Nielsen, J.; Lahav, M.; Leiserowitz, L. *J. Phys. Chem.* **1993**, *97*, 5200.
(56) Jacquemain, D.; Grayer Wolf, S.; Leveiller, F.; Lahav, M.; Leiserowitz, L.; Deutsch, M.; Kjaer, K.; Als-Nielsen, J. *J. Am. Chem. Soc.* **1990**, *112*, 7724.
(57) Barton, S. W.; Thomas, B. N.; Novak, F.; Weber, P. M.; Harris, J.; Dolmer, P.; Bloch, J. M.; Rice, S. A. *Nature* **1986**, *321*, 685.
(58) Magnussen, O. J.; Ocko, B. M.; Regan, M. J.; Penanen, K.; Pershan, P. S.; Deutsch, M. *Phys. Rev. Lett.* **1995**, *74*, 4444.
(59) Barton, S. W.; Thomas, B. N.; Flom, E. B.; Novak, F.; Rice, S. A. *Langmuir* **1988**, *4*, 233.
(60) Magnussen, O. M.; Ocko, B. M.; Deutsch, M.; Regan, M. J.; Pershan, P. S.; Berman, L. E.; Abernathy, D.; Legrand, J. F.; Grubel, G. *Nature* **1996**, *384*, 250.
(61) Berfeld, M.; Kuzmenko, I.; Weissbuch, I.; Cohen, H.; Howes, P. B.; Kjaer, K.; Aals-Nielsen, J.; Leiserowitz, L.; Lahav. M. *J. Phys. Chem. B* **1999**, *103*, 6891.
(62) Gaarde, P. M.Sc. Thesis, Niels Bohr Institute, University of Copenhagen, 1999.
(63) Davey, R. J.; Maginn, S. J.; Steventon, R. B.; Ellery, J. M.; Murrell, A. V.; Booth, J.; Godwin, A. D.; Rout, J. E. *Langmuir* **1994**, *10*, 1673.
(64) Majewski, J.; Margulis, L.; Jacquemain, D.; Leveiller, F.; Bohm, C.; Arad, T.; Talmon, Y.; Lahav, M.; Leiserowitz, L. *Science* **1993**, *261*, 899.
(65) Berge, B.; Konovalov, O.; Lajzerowicz, J.; Renault, A.; Rieu, J. P.; Vallade, M.; Als-Nielsen, J.; Grubel, G.; Legrand, J. F. *Phys. Rev. Lett.* **1994**, *73*, 1652.
(66) Zakri, C.; Renault, A.; Berge, B. *Physica B* **1998**, *248*, 208.
(67) Edgar, R.; Huang, J. Y.; Popovitz-Biro, R.; Kjaer, K.; Bouwman, W. G.; Howes, P. B.; Als-Nielsen, J.; Shen, Y. R.; Lahav, M.; Leiserowitz, L. *J. Phys. Chem. B* **2000**, *104*, 6843.
(68) Douglas, T.; Mann, S. *Mater. Sci. Eng.* **1994**, *C1*, 193.
(69) Majewski, J.; Popovitz-Biro, R.; Kjaer, K.; Als-Nielsen, J.; Lahav, M.; Leiserowitz, L. *J. Phys. Chem.* **1994**, *98*, 4087.
(70) Torchet, G.; Schwartz, P.; Farges, J.; de Feraudy, M. F.; Raoult, B. *J. Chem. Phys.* **1983**, *79*, 6196.
(71) Zhang, Z.; Mitrinovic, D. M.; Williams, S. M.; Huang, Z.; Schlossman, M. L. *J. Phys. Chem.* **1999**, *110*, 7421.
(72) Brezesinski, G.; Thoma, M.; Struth, B.; Mohwald, H. *J. Phys. Chem.* **1996**, *100*, 3126.
(73) Landau, E. M.; Levanon, M.; Leiserowitz, L.; Lahav, M.; Sagiv, J. *Nature* **1985**, *318*, 353.
(74) Landau, E. M.; Wolf, S. G.; Levanon, M.; Leiserowitz, L.; Lahav, M.; Sagiv, J. *J. Am. Chem. Soc.* **1989**, *111*, 1436.
(75) Weissbuch, I.; Berkovic, G.; Leiserowitz, L.; Lahav, M. *J. Am. Chem. Soc.* **1990**, *112*, 5874.
(76) Weissbuch, I.; Berkovic, G.; Yam, R.; Als-Nielsen, J.; Lahav, M.; Leiserowitz, L. *J. Phys. Chem.* **1995**, *99*, 6036.
(77) Frostman, L. M.; Ward, M. D. *Langmuir* **1997**, *13*, 330.
(78) Weissbuch, I.; Majewski, J.; Kjaer, K.; Als-Nielsen, J.; Lahav, M.; Leiserowitz, L. *J. Phys. Chem.* **1993**, *97*, 12848.
(79) Landau, E. M.; Popovitz-Biro, R.; Levanon, M.; Leiserowitz, L.; Lahav, M. *Mol. Cryst. Liq. Cryst.* **1986**, *134*, 323.
(80) Addadi, L.; Moradian, J.; Shai, E.; Maroudas, N. G.; Weiner, S. *Proc. Natl. Acad. Sci. U.S.A.* **1987**, *84*, 2732.
(81) Mann, S.; Heywood, B. R.; Rajam, S.; Birchall, J. D. *Nature* **1988**, *334*, 692.
(82) Rajam, S.; Heywood, B. R.; Walker, J. B. A.; Mann, S.; Davey, R. J.; Birchall, J. D. *J. Chem. Soc., Faraday Trans.* **1991**, *87*, 727.
(83) Heywood, B. R.; Rajam, S.; Mann, S. *J. Chem. Soc., Faraday Trans.* **1991**, *87*, 735.

(84) Heywood, B. R.; Mann, S. *J. Am. Chem. Soc.* **1992**, *114*, 4681.
(85) Heywood, B. R.; Mann, S. *Chem. Mater.* **1994**, *6*, 311.
(86) Berman, A.; Ahn, D. J.; Lio, A.; Salmeron, M.; Reichert, A.; Charych, D. *Science* **1995**, *269*, 515.
(87) Ahn, D. J.; Berman, A.; Charych, D. *J. Phys. Chem.* **1996**, *100*, 12455.
(88) Zhao, X. K.; Yang, J.; McCormick, L. D.; Fendler, J. H. *J. Phys. Chem.* **1992**, *96*, 9933.
(89) Yang, J.; Fendler, J. H. *J. Phys. Chem.* **1995**, *99*, 5505.
(90) Yang, J.; Fendler, J. H.; Jao, T. C.; Laurion, T. *Microsc. Res. Techn.* **1993**, *27*, 402.
(91) Yang, J.; Meldrum, F. C.; Fendler, J. H. *J. Phys. Chem.* **1995**, *99*, 5500.
(92) Weissbuch, I.; Addadi, L.; Berkovitch-Yellin, Z.; Gati, E.; Lahav, M.; Leiserowitz, L. *Nature* **1984**, *310*, 161.
(93) Weissbuch, I.; Leiserowitz, L.; Lahav, M. *J. Am. Chem. Soc.* **1991**, *113*, 8941.
(94) Weissbuch, I.; Addadi, L.; Lahav, M.; Leiserowitz, L. *Science* **1991**, *253*, 637.
(95) Weinbach, S. P.; Bouwman, W. G.; Kjaer, K.; Als-Nielsen, J.; Lahav, M.; Leiserowitz, L. *J. Phys. Chem.* **1996**, *100*, 8356.
(96) Deutsch, M.; Magnussen, O. M.; Ocko, B. M.; Regan, M. J.; Pershan, P. S. In *Thin Films: Self-Assembled Monolayers of Thiols*; Ulman, A., Ed.; Academic Press: New York, 1999.
(97) Abrahamsson, S.; Dahlén, B.; Löfgren, H.; Pascher, I. In *Progress in the Chemistry of Fats other Lipids*; Pergamon Press: Elmsford, NY, 1978; Vol. 16, p 125.
(98) Majewski, J.; Edgar, R.; Popovitz-Biro, R.; Bouwman, W. G.; Als-Nielsen, J.; Lahav, M.; Leiserowitz, L. *Angew. Chem., Int. Ed. Engl.* **1995**, *34*, 649.
(99) Popovitz-Biro, R.; Majewski, J.; Margulis, L.; Cohen, S.; Leiserowitz, L.; Lahav, M. *J. Phys. Chem.* **1994**, *98*, 4970.
(100) Weissbuch, I.; Guo, S.; Cohen, S.; Edgar, R.; Howes, P.; Kjaer, K.; Als-Nielsen, J.; Lahav, M.; Leiserowitz, L. *Adv. Mater.* **1998**, *10*, 117.
(101) Isz, S.; Weissbuch, I.; Palacin, S.; Ruaudell-Texier, A.; Bouwman, W. G.; Kjaer, K.; Als-Nielsen, J.; Leiserowitz, L.; Lahav, M. *Chem. Eur. J.* **1997**, *3*, 930.
(102) Zhu, D. M.; Dash, J. G. *Phys. Rev. Lett.* **1986**, *57*, 2959.
(103) Elbaum, E.; Schick, M. *Phys. Rev. Lett.* **1991**, *66*, 1713.
(104) Earnshaw, J. C.; Hughes, C. J. *Phys. Rev.* **1992**, *A 46*, R4494.
(105) Wu, X. Z.; Sirota, E. B.; Ocko, B. M.; Deutsch, M. *Phys. Rev. Lett.* **1993**, *70*, 958.
(106) Ocko, B. M.; Wu, X. Z.; Sirota, E. B.; Sinha, S. K.; Gang, O.; Deutsch, M. *Phys. Rev. E* **1997**, *55*, 3164.
(107) Gang, O.; Ocko, B. M.; Wu, X. Z.; Sirota, E. B.; Deutsch, M. *Phys. Rev. Lett.* **1998**, *80*, 1264.
(108) Gang, O.; Ocko, B. M.; Wu, X. Z.; Sirota, E. B.; Deutsch, M. *Synchrotron Radiat. News* **1999**, *12*, 34.
(109) Als-Nielsen, J.; Christensen, F.; Pershan, P. S. *Phys. Rev. Lett.* **1982**, *48*, 1107.
(110) Pershan, P. S.; Als-Nielsen, J. *Phys. Rev. Lett.* **1984**, *52*, 759.
(111) Ocko, B. M.; et al. *Phys. Rev. Lett.* **1986**, *57*, 94.
(112) Deutsch, M.; et al. *Europhys. Lett.* **1995**, *30*, 283.
(113) Weissbuch, I.; Lahav, M.; Leiserowitz, L.; Lederer, K.; Godt, A.; Wegner, G.; Howes, P. B.; Kjaer, K.; Als-Nielsen, J. *J. Phys. Chem.* **1998**, *102*, 6313.
(114) Lederer, K.; Godt, A.; Howes, P. B.; Kjaer, K.; Als-Nielsen, J.; Lahav, M.; Wegner, G.; Leiserowitz, L.; Weissbuch, I. *Chem. Eur. J.* **2000**, *6*, 2173.
(115) Popovitz-Biro, R.; Edgar, R.; Weissbuch, I.; Lavie, R.; Cohen, S.; Kjaer, K.; Als-Nielsen, J.; Wasserman, E.; Leiserowitz, L.; Lahav, M. *Acta Polym.* **1998**, *49*, 622.
(116) Kitano, H.; Ringsdorf, H. *Bull. Chem. Soc. Jpn.* **1985**, *58*, 2826.
(117) Ariga, K.; Kunitaki, T. *Acc. Chem. Res.* **1997**, *31*, 3371.
(118) Kurihara, K.; Ohto, K.; Honda, Y.; Kunitake, T. *J. Am. Chem. Soc.* **1991**, *113*, 5077.
(119) Kawahara, T.; Kurihara, K.; Kunitake, T. *Chem. Lett.* **1992**, *1992*, 1839.
(120) Lehn, J. M.; Mascal, M.; DeClan, A.; Fischer, J. *J. Chem. Soc., Chem. Commun.* **1990**, 479.
(121) MacDonald, J. C.; Whitesides, G. M. *Chem. Rev.* **1994**, *94*, 2383.
(122) Bohanon, T. M.; Denziger, S.; Fink, R.; Paulus, W.; Ringsdorf, H.; Weck, M. *Angew. Chem., Int. Ed. Engl.* **1995**, *34*, 58.
(123) Ebara, Y.; Itakakura, K.; Okahata, Y. *Langmuir* **1996**, *12*, 5165.
(124) Matsuura, K.; Ebara, Y.; Okahata, Y. *Langmuir* **1997**, *13*, 814.
(125) Kuzmenko, I.; Buller, R.; Bouwman, W. G.; Kjaer, K.; Als-Nielsen, J.; Lahav, M.; Leiserowitz, L. *Science* **1996**, *274*, 2046.
(126) Brianso, M. C.; Leclercq, M.; Jacques, J. *Acta Crystallogr.* **1979**, *B35*, 2751.
(127) Larsen, S.; Diego, H. L. *Acta Crytstallogr.* **1993**, *B49*, 303.
(128) Kuzmenko, I.; Kindermann, M.; Kjaer, K.; Howes, P. B.; Als-Nielsen, J.; Kiedrowski, G. v.; Leiserowitz, L.; Lahav, M. *J. Am. Chem. Soc.* **2001**, *123*, 3771.
(129) Russell, V. A.; Ward, M. D. *J. Mater. Chem.* **1997**, *7*, 1123.
(130) Russell, V. A.; Evans, C. C.; Li, W.; Ward, M. D. *Science* **1997**, *276*, 575.
(131) Guo, S.; Popovitz, R.; Weissbuch, I.; Cohen, H.; Hodes, G.; Lahav, M. *Adv. Mater.* **1998**, *10*, 121.
(132) Weissbuch, I.; Baxter, P. N. W.; Cohen, S.; Cohen, H.; Howes, P.; Kjaer, K.; Hanna, G. S.; Schubert, U. S.; Als-Nielsen, J.; Lehn, J.-M.; Leiserowitz, L.; Lahav, M. *J. Am. Chem. Soc.* **1998**, *120*, 4850.
(133) Weissbuch, I.; Baxter, P. N. W.; Kuzmenko, I.; Cohen, H.; Cohen, S.; Kjaer, K.; Howes, P. W.; Als-Nielsen, J.; Lehn, J. M.; Leiserowitz, L.; Lahav, M. *Chem. Eur. J.* **2000**, *6*, 725.
(134) Bawendi, M. G.; Steigerwald, M. C.; Brus, L. E. *Annu. Rev. Phys. Chem.* **1990**, *41*, 477.
(135) Eychmuller, A.; Mews, A.; Weller, H. *Chem. Phys. Lett.* **1993**, *208*, 59.
(136) Micic, O. I.; Sprague, J. R.; Curtis, C. J.; Jones, K. M.; Machol, J. L.; Nozik, A. J.; Giessen, H.; Fluegel, B.; Mohs, G.; Peyghambarian, N. *J. Phys. Chem.* **1995**, *99*, 7754.
(137) Daboussi, B. O.; Murray, C. B.; Rubner, M. F.; Bawendi, M. G. *Chem. Mater.* **1994**, *6*, 216.
(138) Heath, J. M.; Knobler, C. M.; Leff, D. V. *J. Phys. Chem. B* **1997**, *101*, 189.
(139) Ghadiri, M. R.; Granja, J. R.; Milligan, R. A.; McRee, D. E.; Khazanovich, N. *Nature* **1993**, *366*, 324.
(140) Krejchi, M. T.; Atkins, E. D. T.; Waddon, A. J.; Fourier, M. J.; Mason, T. L.; Tirrell, D. A. *Science* **1994**, *265*, 1427.
(141) Yu, S.; Conticello, V. P.; Zhang, G.; Kayser, C.; Fournier, M. J.; Mason, T. L.; Tirrell, D. A. *Nature* **1997**, *389*, 167.
(142) Osterman, D.; Mora, R.; Kezdy, F. D.; Kaiser, E. T.; Meredith, S. C. *J. Am. Chem. Soc.* **1984**, *107*, 6845.
(143) DeGrado, W. F.; Lear, J. D. *J. Am. Chem. Soc.* **1985**, *107*, 7684.
(144) Rapaport, H.; Kjaer, K.; Jensen, T.; Leiserowitz, L.; Tirrell, D. A. *J. Am. Chem. Soc.* **2001**, *122*, 12523.
(145) Hunter, C. A.; Singh, J.; Thornton, J. M. *J. Mol. Biol.* **1991**, *218*, 837.
(146) Smith, C. K.; Regan, L. *Science* **1995**, *270*, 980.
(147) Lafont, S.; Rapaport, H.; Somjen, G. J.; Renault, A.; Howes, P. B.; Kjaer, K.; Als-Nielsen, J.; Leiserowitz, L.; Lahav, M. *J. Phys. Chem.* **1998**, *102*, 761.
(148) Rapaport, H.; Kuzmenko, I.; Lafont, S.; Kjaer, K.; Howes, P. B.; Als-Nielsen, J.; Lahav, M.; Leiserowitz, L., submitted for publication.
(149) Rapaport, H.; Kuzmenko, I.; Kjaer, K.; Howes, P.; Bowman, W.; Als-Nielsen, J.; Leiserowiz, L.; Lahav, M. *J. Am. Chem. Soc.* **1997**, *119*, 11211.
(150) Rapaport, H.; Kim H. S.; Kjaer, K.; Howes, P.; Als-Nielsen, J.; Ghadiri, M. R.; Leiserowitz, L.; Lahav, M. *J. Am. Chem. Soc.* **1999**, *121*, 1186.
(151) Fukuto, M.; Heilmann, R. K.; Pershan, P. S.; Yu, S. M.; Griffiths, J. A.; Tirrell, D. A. *J. Chem. Phys.* **1999**, *111*, 9761.
(152) Kornberg, R. D.; Ribi, H. O. In *Protein Structure, Folding, Design 2, Proceedings of a DuPont-UCLA Symposium*; Oxender, D. L., Ed.; Alan R. Liss, Inc.: New York, 1987; p 175.
(153) Uzgiris, E. E.; Kornberg, R. D. *Nature* **1983**, *301*, 125.
(154) Ribi, H. O.; Reichard, P.; Kornberg, R. D. *Biochemistry* **1987**, *26*, 7974.
(155) Ludwig, S. D.; Ribi, H. O.; G, K. S.; Kornberg, R. D. *Proc. Natl. Acad. Sci.* **1986**, *83*, 8585.
(156) Darst, S. A.; Ribi, H. O.; Pierce, W.; Kornberg, R. D. *J. Mol. Biol.* **1988**, *203*, 269.
(157) Ku, A. C.; Darst, S. A.; Robertson, C. R.; Gast, A. P.; Kornberg, R. D. *J. Phys. Chem.* **1993**, *97*, 3013.
(158) Darst, S. A.; Ahlers, M.; Meller, P. H.; Kubalek, E. W.; Blakenburg, R.; Ribi, H. O.; Ringsdorf, H.; Kornberg, R. D. *Biophys. J.* **1991**, *59*, 387.
(159) Vaknin, D.; Als-Nielsen, J.; Piepenstock, M.; Losche, M. *Biophys. J.* **1991**, *60*, 1545.
(160) Vaknin, D.; Kjaer, K.; Ringsdorf, H.; Blankenburg, R.; Piepenstock, M.; Dieterich, A.; Losche, M. *Langmuir* **1993**, *9*, 1171.
(161) Haas, H.; Brezezenski, G.; Mohwald, H. *Biophys. J.* **1995**, *68*, 312.
(162) Lenne, P. F.; Berge, B.; Renault, A.; Konovalov, O.; Legrand, J. F.; Balavoine, F.; Lal, J.; Grubel, G.; Bregsma-Schutter, W.; Brisson, A. Manuscript in preparation.
(163) Frenzen, A.; Wegand, M.; Verclas, S.; Denscher, N. A.; Buldt, G.; Howes, P. B.; Kjaer, K.; Losche, M. *Eur. Biophys J.* **1997**, *26*, 116.
(164) Weissbuch, I.; Popovitz-Biro, R.; Lahav, M.; Leiserowitz, L. *Acta Crystallogr.* **1994**, *B51*, 115.
(165) James, R. W. *The Optical Principles of the Diffraction of X-rays*; Ox Bow: Woodbridge, CT, 1982.
(166) Born, M.; Wolf, E. *Principles of Optics*; MacMillan: New York, 1959.
(167) Marra, W. C.; Eisenberger, P.; Cho, A. Y. *J. Appl. Phys.* **1979**, *50*, 6927.
(168) Eisenberger, P.; Marra, W. C. *Phys. Rev. Lett.* **1981**, *46*, 1081.
(169) Vineyard, G. *Phys. Rev. B* **1982**, *26*, 4146.
(170) Feidenhans'l, R. *Surf. Sci. Rep.* **1989**, *10* (3), 105.
(171) Braslau, A.; Deutsch, M.; Pershan, P. S.; Weiss, A. H.; Als-Nielsen, J.; Bohr, J. *Phys. Rev. Lett.* **1985**, *54*, 114.

(172) Braslau, A.; Pershan, P. S.; Swislow, G.; Ocko, B. M.; Als-Nielsen, J. *Phys. Rev. A* **1988**, *38*, 2457.
(173) Pershan, P. S. *Coll. Phys.* **1989**, *50*, C7.
(174) Parrat, L. G. *Phys. Rev.* **1954**, *95*, 359.
(175) Kjaer, K.; Als-Nielsen, J.; Helm, C. A.; Tippman-Krayer, P.; Mohwald, H. *J. Phys. Chem.* **1989**, *93*, 3200.

CR990038Y